UNIVERSITY OF OKLAHOMA
GRADUATE COLLEGE

CLUTTER DETECTION AND MITIGATION FOR DUAL-POLARIZATION WEATHER RADAR

A DISSERTATION
SUBMITTED TO THE GRADUATE FACULTY
in partial fulfillment of the requirements for the
Degree of
DOCTOR OF PHILOSOPHY

By

MOHAMMAD-HOSSEIN GOLBON-HAGHIGHI
Norman, Oklahoma
2019

CLUTTER DETECTION AND MITIGATION FOR DUAL-POLARIZATION WEATHER RADAR

A DISSERTATION APPROVED FOR THE
SCHOOL OF ELECTRICAL AND COMPUTER ENGINEERING

BY THE COMMITTEE CONSISTING OF

Dr. Guifu Zhang, Chair

Dr. Richard Doviak, co-Chair

Dr. Yan Zhang

Dr. Nathan Goodman

Dr. Yang Hong

Acknowledgments

First, I would like to express my deep gratitude to my supervisor, Professor Guifu Zhang, for providing guidance and inspiration throughout the course of my PhD studies. His kindness and support will never be forgotten. His stimulating suggestions, ideas, and encouragement help me persevere with my research. I have benefited tremendously from his experience and broad knowledge. I also appreciate the valuable discussions with my co-advisor, Professor Richard Doviak, who is always ready to help, patient with difficulties and encouraging of new ideas. His extraordinary high scientific standards and work ethic set an example for me.

I would also like to thank the members of my dissertation committee, Professor Yan Zhang, Professor Nathan Goodman, and Professor Yang Hong, for taking the time out of their busy schedules to carefully review my thesis, providing me with insightful questions and suggestions. I offer my regards and blessings to all members of the Advanced Radar Research Center (ARRC), who supported me in all respects during the completion of the project.

Finally, I would like to extend my gratitude to my parents for their unconditional support and love. I would like to give my most gracious gratitude to my family, especially my wife, and my three-year-old son, Taha. They are the ones who make my life meaningful and promising. Their unwavering support and encouragement make all of this possible.

Table of Contents

List of Tables

List of Figures

Abstract

Ground clutter in weather radar observations causes degradation of data quality and can lead to misinterpretation of radar echoes. It is important to detect clutter and mitigate its effects to obtain accurate weather measurements. The focus of this study is to improve the performance of clutter detection algorithms by presenting different discriminant functions. A Bayesian classifier is used to make an optimal decision based on discriminant functions to detect clutter mixed with weather echoes. The conditional probability density functions for clutter and weather signals may change and may need to be updated due to changing weather conditions, clutter, and radar parameters. Therefore, to make it more efficient, a multivariate Gaussian mixture model is presented to parametrize discriminant functions and reduce the complexity of detection algorithms. The model parameters are estimated based on the maximum likelihood, using the Expectation-Maximization (ML-EM) method.

A dual-polarization clutter filtering algorithm is also presented to mitigate ground clutter effects on weather radar measurements. A multivariate Gaussian model is introduced to parametrize clutter and weather power spectrums, and the Maximum A Posterior (MAP) method is used to estimate weather components. Instead of using a random phase, the phase of the retrieved weather spectrum is estimated based on the statistical properties of dual-polarization weather signals. The performance of the clutter detection and filtering algorithms are shown by applying them to the radar data collected by the national WSR-88D (KOUN) polarimetric radar and are compared to existing detection and filtering algorithms. It is shown that the proposed algorithms

can effectively mitigate clutter effects and substantially improve polarimetric weather radar data quality.

Chapter 1 :

Introduction

Ground clutter detection is one of the main challenges in the weather radar community because clutter mixed with echoes from precipitation can bias weather radar measurements. Ground clutter are echoes received from objects on the ground when parts of the main lobe or sidelobes of the radar antenna illuminate objects on the ground. Therefore, clutter contamination is more severe for the measurements of near ground precipitation, from which accurate rainfall rate estimation is required. Clutter is mostly located around zero Doppler velocity in the spectral domain and is supposed to be statistically stationary in the time domain. Therefore, a band-stop filter as a simple traditional method can be applied to the clutter contaminated radar signals to mitigate clutter effects [1, 2]. Although this filtering method is normally used to remove clutter from weather radar signals, some power components of weather signals may fall into the stop-band, which then suppresses the weather power components and biases the spectral moment estimates of weather spectra, especially for narrow-band zero-velocity weather signals [3-6]. Thus, the ground clutter locations need to be identified accurately to avoid biases from unnecessarily filtering weather signals.

Over the past few years, the researchers in the weather radar community focused on the design of more effective clutter detection algorithms that can detect weak clutter that contaminates weather echoes causing errors in polarimetric variables and spectrum-width which are particularly susceptible to bias due to even weak clutter [7]. It is essential to estimate accurately polarimetric parameters that can provide important information such as rainfall rate, tornado signatures, and types of precipitation. In [8], a static clutter map is determined in clear-air conditions and used for clutter detection in the weather condition. However, changing clutter maps under

different weather conditions are not considered in this algorithm. In [9, 10], the clutter mitigation decision (CMD) is introduced based on a fuzzy logic approach that combines the clutter phase alignment, the reflectivity texture, and the SPIN change (the number of reflectivity fluctuations) as three discriminant functions for ground clutter detection. The CMD algorithm, widely known and accepted in the weather radar community, is compared to our proposed algorithm in the simulation results.

More recently, the spectral properties have been considered for ground clutter detection. The analysis of clutter signals in the spectral domain is presented in [2, 5, 11] to take advantage of their unique spectrum properties to introduce new discriminant functions [7]. Spectrum clutter identification (SCI) algorithm is presented in [2, 11] and uses four discriminant functions for clutter detection: Spectrum Power Distribution, Spectrum Phase Fluctuation, Power Texture, and Spectrum Width Texture.

Most detection algorithms are based on the statistical properties for a single polarization, but better performance can often be achieved by using polarimetric weather data. Dual-polarization clutter detection algorithms are more attractive because they can take advantage of the polarization diversity. Ground clutter and weather signals have different polarimetric characteristics which can be utilized to distinguish clutter from weather signals The authors in [12] introduced CLEAN-AP (clutter environment analysis using adaptive processing) algorithm based on the autocorrelation spectral density (ASD) to suppress the effect of ground clutter to achieve better performance. This technique is extended in [13] to apply ASD to the staggered-PRT (pulse repetition time) sequences. In [14], the differential phase between the complex spectral

coefficients of the two spectra from the even and odd samples is proposed to identify ground clutter.

Though there are various clutter detection algorithms, dual-polarization algorithms are more attractive because they can take advantage of the different polarization scattering properties of precipitation and ground objects to discriminate clutter from weather signals [15-17]. The co-polar cross-correlation coefficient ρ_{hv} and differential reflectivity (Z_{DR}) are used in [18, 19], as the dual-polarization discriminant functions. The authors in [20] have introduced the scan-to-scan (dual-scan or DS) method based on the cross-correlation coefficient between consecutive scans as a new discriminant for clutter detection. This study shows that the correlation time of radar signals from hydrometers is typically much shorter than that of clutter. However, the dual-scan data are not available for the most operational weather radars [20].

In [5, 19], the dual-polarization radar data are used to define three discriminant functions, and a Bayesian classifier is used to make the decision for clutter detection. The co-polar cross-correlation coefficient, ρ_{hv}, is combined with the power ratio (PR) [5, 19] and Z_{DR} to form the dual-polarization (DP) clutter detection algorithm. The DP algorithm has been extended in [18] by adding a new discriminant function based on the cross-correlation of echoes received on DS separated by several seconds to form the dual-polarization dual-scan (DP-DS) algorithm. It is worth mentioning that using several discriminant functions to make a decision for classification can increase the computational complexity and processing time.

In [21, 22], the dual-polarization spectral decomposition technique is proposed to identify the non-meteorological echoes present in radar observations such as sea

clutter, chaff, birds, and insects. In [23, 24], a Bayesian radar-signal classifier algorithm is employed to identify ground clutter in terms of its spatial statistical features, and the spatial analysis is used to estimate the relative clutter calibration and its uncertainty for both reflectivity and differential reflectivity.

In chapter 4, we introduce a new discriminant function to improve the performance of the clutter detection algorithms. The algorithm is based on the phase fluctuations index (PFI), and it is found that this discriminant function has the best separation between clutter and weather signals even for the low values of the clutter to weather signal ratio (CSR). Numerical simulations and theory show the phase of weather signal is typically a rapidly varying function for echoes from each resolution volume [4, 5], whereas the phase of the ground clutter is typically slowly varying. Thus, the fluctuations of the signal phase for each resolution can be considered as a robust discriminant function to detect clutter. We show that the probability density functions (PDF) of the PFI for weather and clutter signals are entirely separated using PFI and thus can effectively detect clutter mixed with weather echoes with the highest probability of detection compared to other detection algorithms.

A 3D discriminant function is introduced in chapter 5 to improve the performance of clutter detection algorithms. The algorithm is based on the phase structure function (PSF) for H and V polarizations and the dual-scan cross-correlation coefficient [4, 5]. The wave scattering from fixed scatterers on the ground (or ground clutter) and randomly distributed hydrometers yield a relatively slow and fast fluctuation in phase, respectively. The phase structure function can be used as a proper discriminant function to improve the performance of the clutter detection algorithms. Additionally, the

correlation time of radar signals from the randomly distributed hydrometers is typically much shorter than that of fixed scatterers or ground clutter. Therefore, the 3D discriminant function based on the phase structure function of H and V polarizations and dual-scan cross-correlation can achieve a good probability of detection for ground clutter detection algorithms. It is shown that the 3D discriminant function has a good separation in 3D visualization and can achieve the highest probability of detection compared to other detection algorithms. Therefore, the phase fluctuations for each resolution volume can be considered as a robust discriminant function to distinguish clutter from weather signals.

The PDFs of discriminant functions may change based on the weather, types of clutter, antenna rotation and the radar characteristics, and may need to be updated. Thus, the complete knowledge about the probabilistic structure of the conditional PDFs may not be available for real-time implementations. Therefore, a multivariate Gaussian mixture model is developed to parametrize the class-conditional densities for the 3D discriminant function, and the complexity of the problem is reduced significantly. [25-27] The model parameters are then estimated based on the maximum likelihood, using the Expectation-Maximization (ML-EM) algorithm.

The Doppler spectrum of ground clutter is mostly located around zero Doppler velocity because ground targets are stationary or only have slow motions. Clutter filtering in the frequency domain has become more popular. The authors in [28] proposed the Gaussian model adaptive processing (GMAP) method. GMAP could recover the weather spectrum after notching the spectrum around zero velocity. However, the filtering still biases the weather signal, and its performance needs to be

improved. [4, 5] Hence, after detecting ground clutter, a high-performance clutter filtering system needs to be applied to retrieved weather signals with the least bias effect on weather signals. A dual polarization clutter filtering algorithm is introduced in chapter 6 to mitigate ground clutter effects on weather radar measurements. The statistical properties of the dual polarization radar data are utilized in time and spectral domains to reconstruct the weather signals/data from clutter contaminated resolution volumes. A multivariate Gaussian mixture model is introduced to parametrize clutter and weather power spectrums, and the Maximum A Posterior (MAP) method is used to estimate model parameters. Instead of using the random phase, the phase of the retrieved weather spectrum is estimated based on the weather properties to be more accurate.

The remainder of this dissertation is organized as follows: In chapter 2, existing discriminant functions for several clutter detection algorithms are discussed; In chapter 3, the dual-pol dual-scan (DPDS) clutter detection algorithm is presented; In chapter 4, the ground clutter detection for weather radar using phase fluctuation index is introduced, and the performance of the proposed algorithm is evaluated using controlled data set collected by KOUN polarimetric radar. In chapter 5, the 3D-PSF algorithm is presented, and a multivariate Gaussian mixture model is introduced to parameterize the PDFs of discriminant functions. Dual-polarization clutter filtering algorithm is introduced in chapter 6. Conclusions and future works are drawn in chapter 7.

Chapter 2

Discriminant Functions for Ground Clutter Detection

2.1 Discriminant functions

In this chapter, existing discriminant functions are presented for clutter detection algorithms. Special datasets were collected by KOUN (WSR-88D) radar on different days during times and locations when and where nearly pure weather and ground clutter were available to be combined to synthesize a weather plus clutter PPI dataset of known clutter-to-weather echo signal ratio or CSR. The synthesized PPI dataset is used to compare clutter detection performance for detection algorithms with ground truth. These specially collected and edited clutter and weather data were also used to find the PDFs of the discriminant function for pure weather and clutter.

Other clutter and weather datasets are used as the testing datasets and were collected by the KOUN radar at 00:47 UTC on 4 February and at 14:02 UTC on 9 February 2011, respectively. It should be noted that the controlled I/Q dataset is created by matching and combining the almost pure clutter data and pure weather data to find ground truth, as discussed in [18, 19]. The nearly pure clutter data was collected at the low elevation angles (0.5°) under cold, clear air conditions, while the nearly pure weather data was obtained at 1.5° within the farther ranges (over 50km for this study) from the radar location, where ground clutter can be neglected. The testing weather data collected at ranges beyond ground clutter is collapsed to near ranges. If needed, weather data collected at high elevation angles (above 2° for the WSR-88D [4,

Section7.9]) typically have negligible clutter so that pure weather data can be combined with the specially collected and edited clutter PPI without range collapsing. [5, 29]

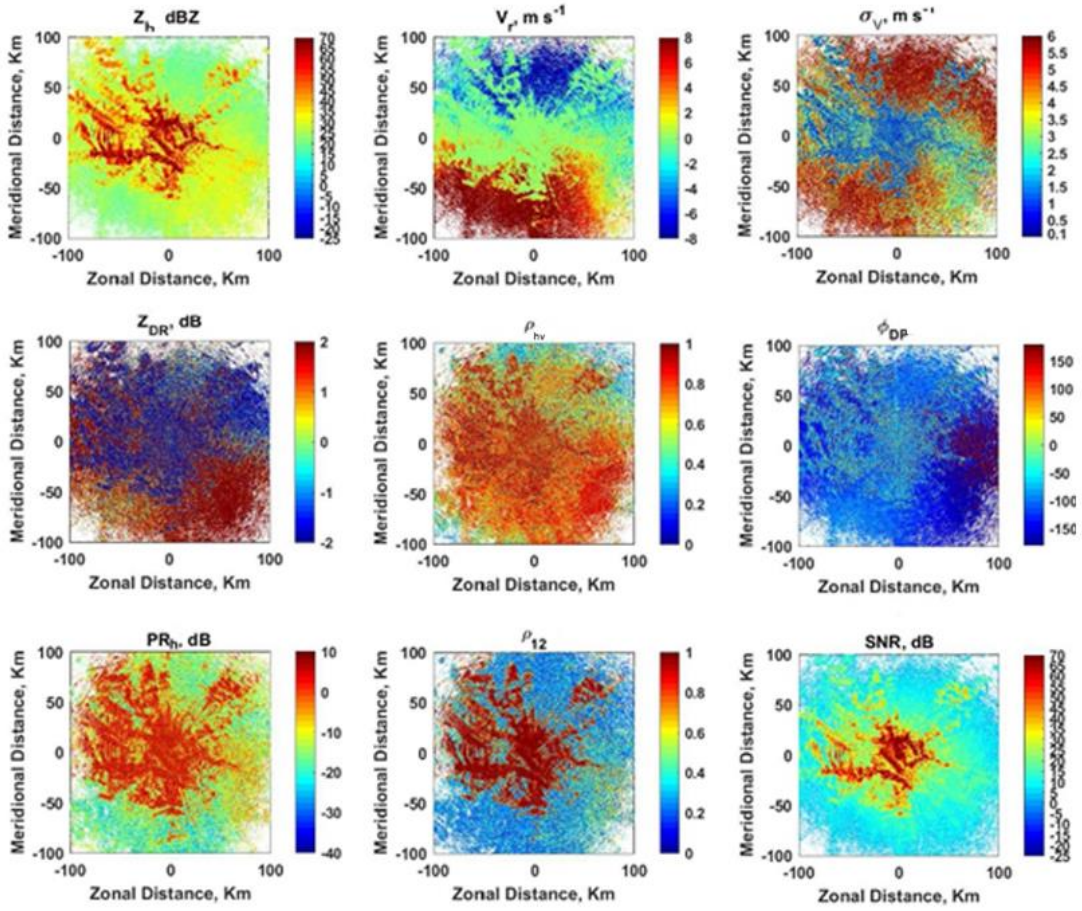

Figure 2-1 : Radar clutter data collected at 07:09 UTC on 27 May 2010; a) Reflectivity, b) Doppler Velocity, m/s; c) Spectrum width; d) Differential reflectivity (Z_{DR}); e) Dual-polarization cross-correlation coefficient; f) Differential phase; g) Power Ratio (PR), dB; h) Dual-Scan cross-correlation coefficient; i) SNR, dB.

Special data sets were collected by KOUN (WSR-88D) radar on two different days during times and locations when and where nearly pure weather and ground clutter were available to be combined to synthesize a weather plus clutter PPI data set of known clutter-to-weather echo signal ratio (CSR). The synthesized PPI data set is

used to compare clutter detection performance for the PFI and other detection algorithms with ground truth. These specially collected and edited clutter and weather data were also used to find the PDFs of the discriminant function (PFI) for pure weather and clutter. The nearly pure clutter data set was collected in clear air conditions by the KOUN (WSR-88D) radar, at 00:46 UTC on February 4, 2011, and 07:09 UTC on 27 May 2010, and nearly pure weather data were collected at 13:08 UTC on February 9, 2011. To evaluate the performance of the clutter detection algorithm, we use other clutter and weather data sets, as the testing data sets, collected by the KOUN radar at 00:47 UTC on February 4, 2011, and at 14:02 UTC on February 9, 2011, respectively. It should be noted that we created a controlled I/Q data set by matching and combining the almost pure clutter data and pure weather data to find ground truth, as discussed in [18] and [19]. The nearly pure clutter data was obtained at the low elevation angles (0.50°) under cold clear air conditions, while the pure weather data was obtained at 1.50° within the farther ranges (over 50 km) from the radar location, where ground clutter can be neglected. The testing weather data collected at ranges beyond ground clutter is collapsed to near ranges, if needed, (weather data collected at high elevation angles [above 2° for the WSR-88D [3, Sec. 7.9] typically have negligible clutter so that pure weather data can be combined with the specially collected and edited clutter PPI without range collapsing]. [18] The SNR, reflectivity, Doppler velocity, differential phase, dual-pol cross-correlation coefficient, differential reflectivity differential phase, dual-scan cross-correlation coefficient, and power ratio of the clutter data collected at 07:09 UTC on 27 May 2010 and weather data collected at 13:08 on 9 February 2011 are shown in Figure 2-1and Figure 2-2.

To mitigate/avoid noise effects, data for resolution volumes with weather and clutter signal-to-noise ratio (SNR) less than 20 dB have been deleted. To provide pure clutter fields, the data in resolution volumes contaminated by moving point objects (e.g., birds, aircraft, and moving vehicles on the ground) are deleted. Furthermore, ground clutter I/Q data were edited by deleting the resolution volumes showing mean Doppler velocities.

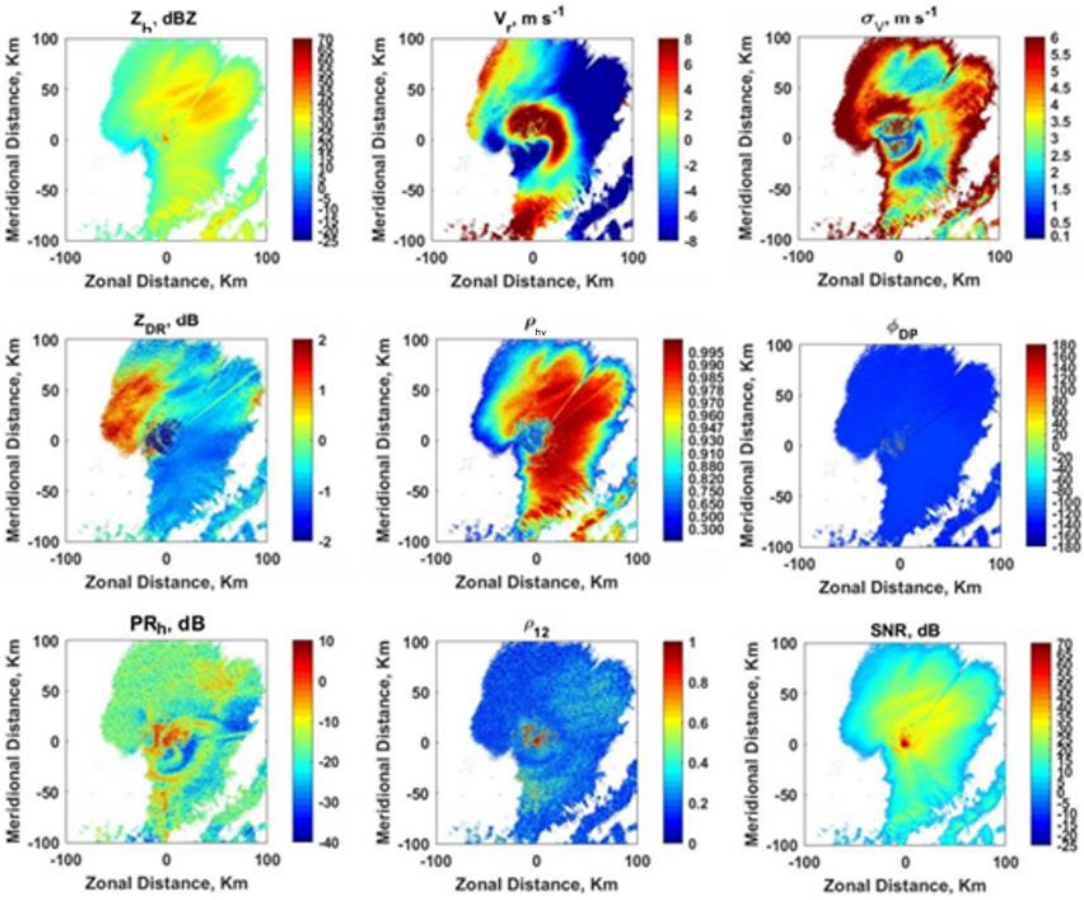

Figure 2-2: Radar weather data collected at 13:08 on 9 February 2011; a) Reflectivity, b) Doppler Velocity, m/s; c) Spectrum width; d) Differential reflectivity (Z_{DR}); e) Dual-polarization cross-correlation coefficient; f) Differential phase; g) Power Ratio (PR), dB; h) Dual-Scan cross-correlation coefficient; i) SNR, dB.

2.2 Discriminant functions for ground clutter detection algorithms:

In this section, different discriminant functions are introduced for clutter detection algorithms. These discriminants are used to make decisions to identify clutter contaminated weather signals. The clutter detection algorithms are using discriminant functions to make optimal decision based on the Bayesian or a fuzzy logic approach for classification. These discriminant functions are listed as:

- Dual-polarization cross-correlation coefficient (H and V-polarization) (ρ_{hv})
- Dual-scan cross-correlation coefficient (ρ_{12})
- Differential reflectivity (Z_{DR})
- Power ratio (PR)
- Phase of Dual-Scan Cross-Correlation
- Differential phase.

2.2.1 Co-Polar Cross-Correlation Coefficient (ρ_{hv})

The co-polar correlation coefficient between H and V, commonly known as dual-polarization correlation coefficient for H and V co-polar echoes, is a polarimetric parameter frequently used in the weather radar community. It is defined as [5, 30]:

$$\rho_{hv} = \frac{\left|\frac{1}{M}\sum_{m=1}^{M} V_h(m)V_v^*(m)\right|}{\sqrt{\left|\frac{1}{M}\sum_{m=1}^{M} V_h(m)V_h^*(m)\right|\left|\frac{1}{M}\sum_{m=1}^{M} V_v(m)V_v^*(m)\right|}} \quad 0 \le m \le M-1 \tag{2.1}$$

where V represents the complex echo signal sample received from h (v) as the horizontally (vertically) polarized echo samples; index m signifies the echo sample number; and M is the number of samples in a dwell time (i.e., the time used to make

estimates of polarimetric variables and spectral moments). Reliable ground truth is an important issue to evaluate the performance of clutter detectors [9, 10]. To obtain the class label of each resolution volume for obtaining the training data and discriminant PDFs, DPDS has been used as suggested by [18].

The PDF of ρ_{hv} is shown in Figure 2-3 and Figure 2-4. Narrow-band zero-velocity weather signals (W_0) are considered as a separate weather class because their properties are mostly similar to clutter signals and thus are the most challenging to distinguish. W_0 are echoes from resolution volumes where the mean wind radial velocity is weak, with a mean Doppler velocity ($|v_r|$) and the spectrum width (σ_v) close to zero (i.e., $|v_r| \leq 2\ \mathrm{m \cdot s^{-1}}$ and $\sigma_v \leq 2\ \mathrm{m \cdot s^{-1}}$); These weather echoes commonly have a longer correlation time τ_c compared with the other weather signals (*i.e.*, W). It can be seen from this figure that ρ_{hv} values for both clutter and weather signals are mostly close to one. However, the ρ_{hv} for ground clutter has much larger spread values compared with weather signals. It should be noted that the clutter PDF of ρ_{hv} depends on the characteristics of scatterers and radar parameters [31-39] and can be easily updated based on the weather condition, radar, and antenna rotation.

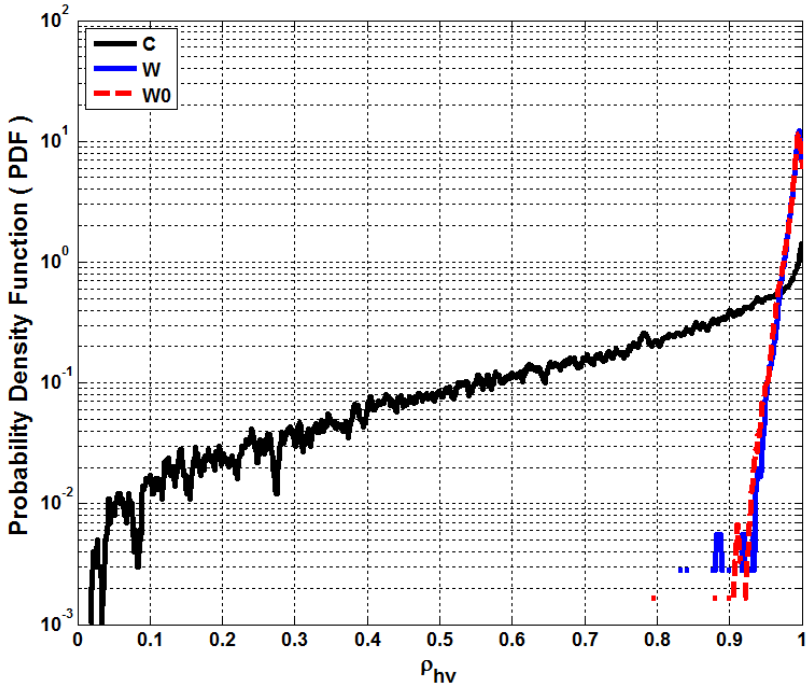

Figure 2-3: The PDF of the co-polar cross-correlation coefficient (ρ_{hv}).

It should be noted that some of the clutter detection algorithms are using the ρ_{hv} as discriminant functions. However, as can be seen from Figure 2-3 and Figure 2-4, there are some overlapped areas between clutter and weather PDFs that can increase the error rate. Moreover, as can be seen from these figures, the peak values for both clutter and weather PDFs for ρ_{hv} are in the same interval and near 1. Furthermore, the PDF of ρ_{hv} for weather is much larger than that of the clutter in their peak regions (near 1 for ρ_{hv}); therefore, it is clear that clutter with near one ρ_{hv} values would most likely be detected as weather instead of clutter. These peak regions have the lower CSR values (less than 0dB) [40, 41] with more weather power than clutter, and this is the reason that these algorithms cannot have a good performance for the low CSR values, especially lower than 0dB.

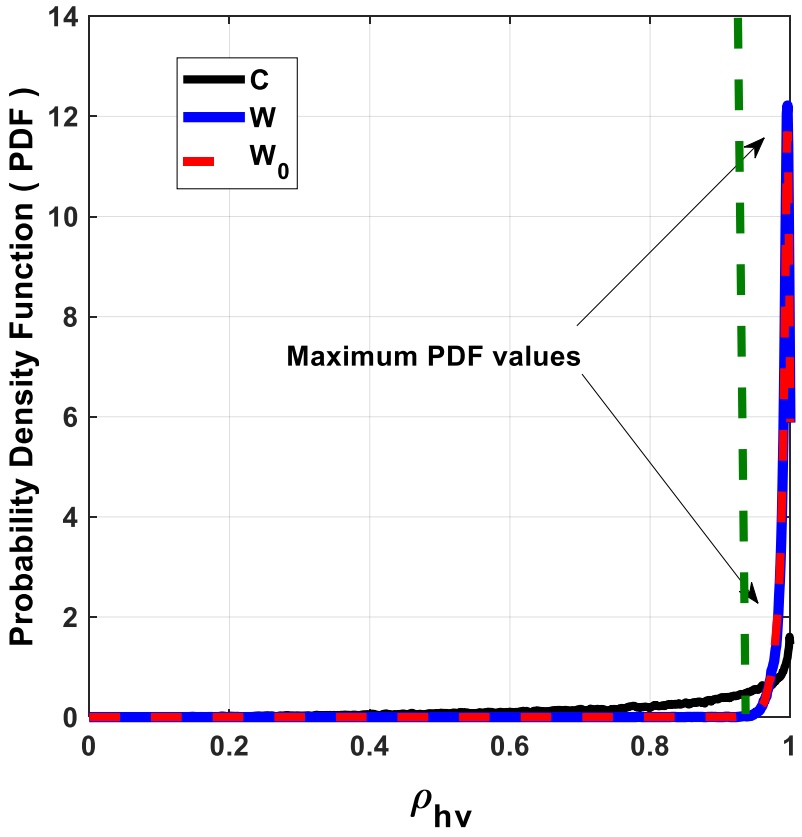

Figure 2-4: The PDF of co-polar cross-correlation coefficient (ρ_{hv})

2.2.2 Dual-Scan Cross-Correlation Coefficient (ρ_{12})

The cross-correlation coefficient between two consecutive scans from the same location is given by [5, 42, 43]:

$$\rho_{12} = \frac{\left|\frac{1}{M}\sum_{m=1}^{M} V_1(m)V_2^*(m)\right|}{\sqrt{\left|\frac{1}{M}\sum_{m=1}^{M} V_1(m)V_1^*(m)\right|\left|\frac{1}{M}\sum_{m=1}^{M} V_2(m)V_2^*(m)\right|}} \qquad 0 \le m \le M-1 \tag{2.2}$$

Ground clutter has a longer correlation time than weather signals; thus, ρ_{12} should be larger for ground clutter than weather signals [4, 5, 20], as shown in Figure 3. This cross-correlation can be calculated for both h and v polarizations.

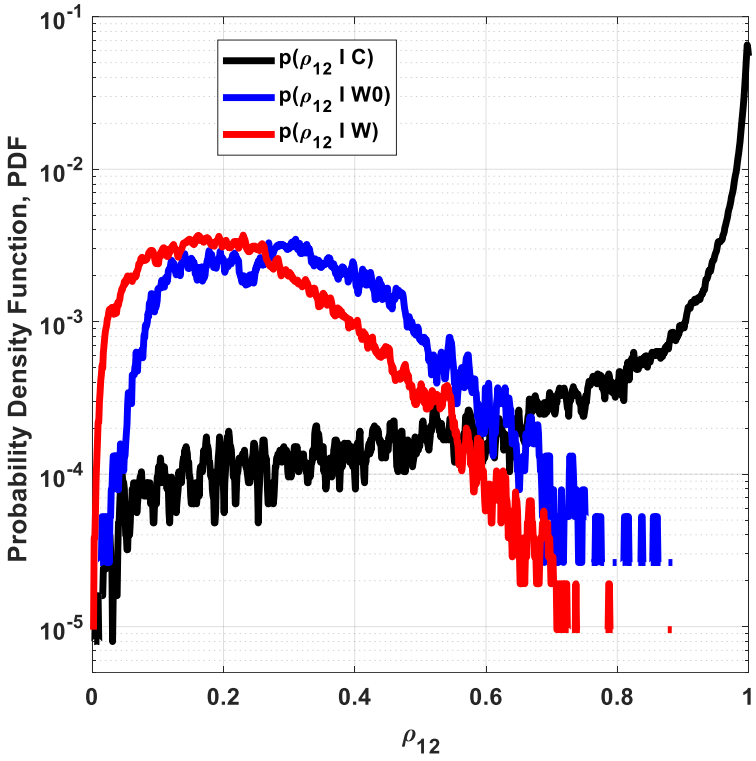

Figure 2-5: The PDF of the dual-scan cross-correlation coefficient (ρ_{12}).

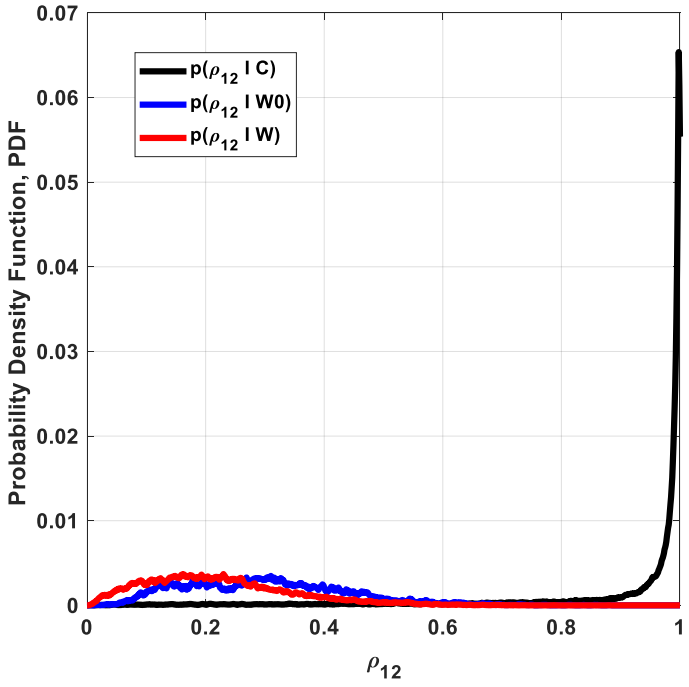

Figure 2-6: The PDF of dual-scan cross-correlation coefficient (ρ_{12})

It is expected that ρ_{12} should be larger for ground clutter than weather signals [4, 5], because ground clutter has a longer correlation time than weather signals, as shown in Figure 2-5 and Figure 2-6. Figure 2-7 illustrates the joint PDF between dual-scan cross-correlation and dual-polarization cross-co-polar correlation for two different SNR threshold values. As expected, the weather signals have larger ρ_{hv} with smaller ρ_{12}. Additionally, the clutter has larger ρ_{12} values with a wide range of ρ_{hv}. Thus, it can be clearly concluded that the joint PDF has a better separation compared to other discriminant functions. Therefore, this discriminant function can reduce the error rate of the detection algorithm and improve the probability of detection compared to previous common algorithms. As can be seen from this figure, the SNR threshold value may change the joint PDFs, but the performance of the DPDS algorithm is not

sensitive to SNR, because the overlapped areas between clutter and weather do not change with SNR. Other discriminants can be considered for future works by using cross-correlation between multiple antennas and exploiting spatial diversity [44-46].

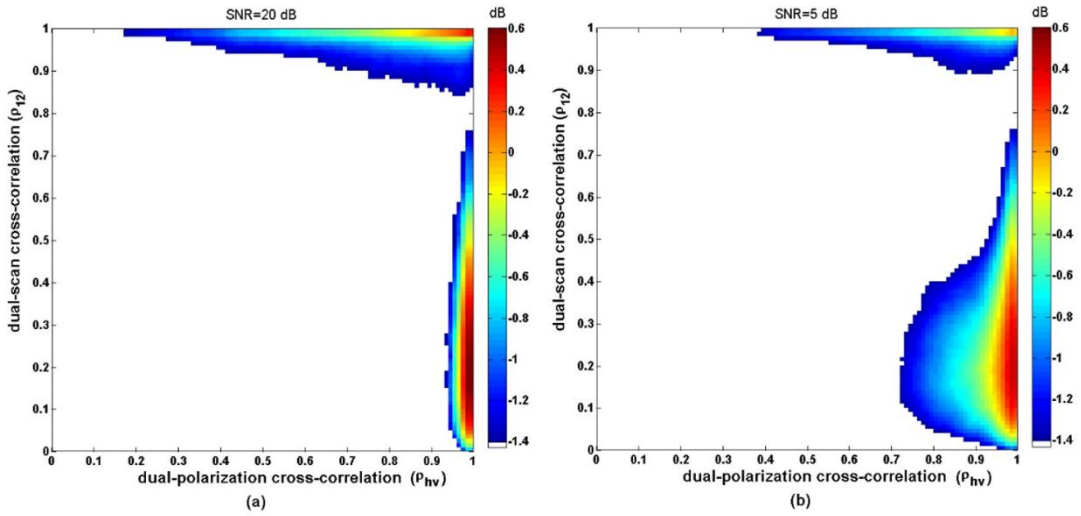

Figure 2-7: The PDF of dual-scan cross-correlation vs. dual-polarization co-polar cross-correlation, obtained from training data (a) SNR threshold value 20 dB and (b) SNR threshold value 5 dB.

The joint PDF between ρ_{12} and ρ_{hv} is shown in Figure 2-7. It is typically expected that the weather signals have larger ρ_{hv} with smaller ρ_{12}. Moreover, the ground clutter has larger ρ_{12} values with a wide range of ρ_{hv}. Thus, ground clutter and weather signals are almost separated in terms of this discriminant function. Therefore, this discriminant function can reduce the detection error rate and improve the probability of detection compared to previous common algorithms [44-46].

2.2.3 Differential Reflectivity (Z_{DR})

Differential reflectivity is the power ratio of horizontal and vertical polarization signals [47] and is defined as:

$$Z_{DR} = 10\log_{10}\left(\frac{\left|\frac{1}{M}\sum_{m=1}^{M} V_h(m)V_h^*(m)\right|}{\left|\frac{1}{M}\sum_{m=1}^{M} V_v(m)V_v^*(m)\right|}\right) \qquad 0 \le m \le M-1 \qquad (2.3)$$

The PDFs of differential reflectivity based on the training data are shown in Figure 2-8. As is normally expected, the Z_{DR} values for clutter have a wider range in comparison to weather signals [4, 5, 18]. Because we conducted two consecutive scans, there are two differential reflectivities (i.e., Z_{DR1} and Z_{DR2}); and both of them most likely have the same PDFs; thus, we used the averaged value for ZDR. It can be seen from Figure 2-8 that both PDFs center near zero, but that clutter has a wide distribution, whereas the PDF for weather signals is narrow. Because the PDF of Z_{DR} for weather is much larger than that of the clutter in the region near zero, it is clear that clutter with the near-zero Z_{DR} values would most likely be detected as weather instead of clutter. Therefore, in order to decrease the detection error rate, Z_{DR} in the interval within the pair of vertical lines is not considered for the clutter detection. However, from our experience, there is a negligible performance improvement for the probability of detection when we use Z_{DR} as a discriminant.

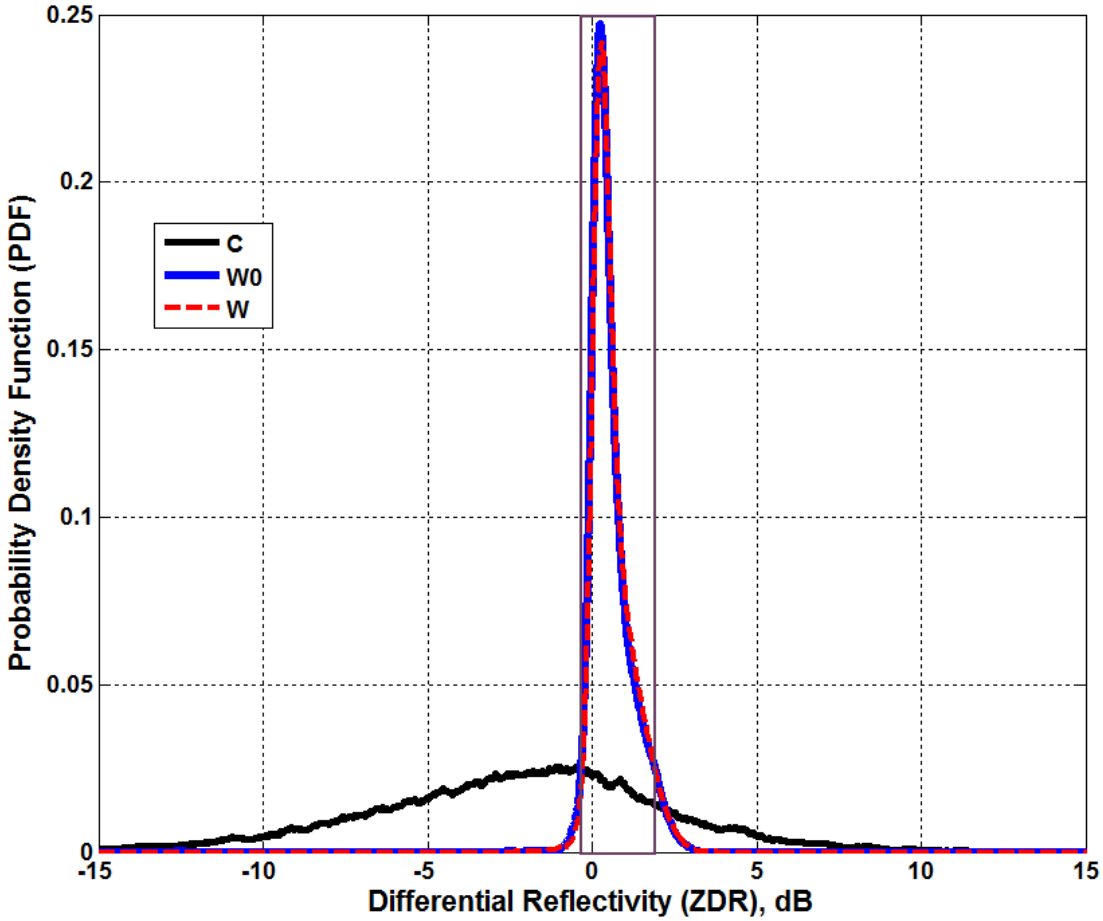

Figure 2-8: The PDF of differential reflectivity (Z_{DR}) for C, W, W0, (*i.e.*, $P(Z_{DR} \mid \omega_i)$ given ω_i = C, W_0, and W), obtained from the training data.

Figure 2-9 shows the 3D joint PDF of Z_{DR}, ρ_{12} and ρ_{hv}. As can be seen from this figure, the joint 3D PDF has better separation and can improve the probability of detection for clutter detection algorithms.

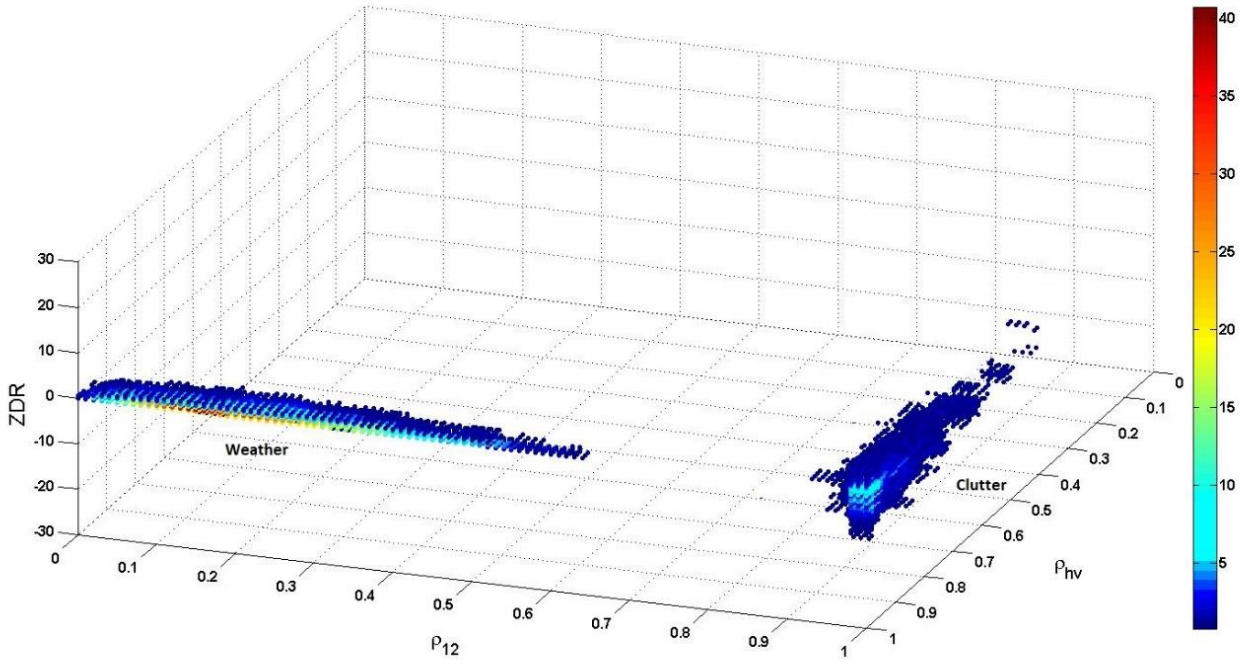

Figure 2-9: The PDF of ZDR vs. ρ_{12} and ρ_{hv} obtained from the training data

2.2.4 Power Ratio (PR)

The power ratio is the ratio between coherent power and incoherent power of the wave scatters from hydrometers or clutters and is defined as [18, 19]:

$$\mathrm{PR}_h = 10\log_{10}\left(\frac{\left|\frac{1}{\mathrm{M}}\sum_{\mathrm{m}=1}^{\mathrm{M}}\mathrm{V}_h(\mathrm{m})\right|^2}{\frac{1}{\mathrm{M}}\sum_{\mathrm{m}=1}^{\mathrm{M}}\left|\mathrm{V}_h(\mathrm{m})\right|^2-\left|\frac{1}{\mathrm{M}}\sum_{\mathrm{m}=1}^{\mathrm{M}}\mathrm{V}_h(\mathrm{m})\right|^2}\right),$$
$$\mathrm{PR}_v = 10\log_{10}\left(\frac{\left|\frac{1}{\mathrm{M}}\sum_{\mathrm{m}=1}^{\mathrm{M}}\mathrm{V}_v(\mathrm{m})\right|^2}{\frac{1}{\mathrm{M}}\sum_{\mathrm{m}=1}^{\mathrm{M}}\left|\mathrm{V}_v(\mathrm{m})\right|^2-\left|\frac{1}{\mathrm{M}}\sum_{\mathrm{m}=1}^{\mathrm{M}}\mathrm{V}_v(\mathrm{m})\right|^2}\right), \quad (2.4)$$

The estimated value of coherent power at the numerator of this equation is defined as the power component at zero frequency and is divided by M^2 according to the definition of Discrete Fourier Transform (DFT). The estimated value of incoherent power at the denominator is the sum of all other power components in the frequency domain divided by M according to Parseval's Theorem i.e. $\frac{1}{\mathrm{M}}\sum_{\mathrm{m}=1}^{\mathrm{M}}\left|\mathrm{V}_h\left(\mathrm{m}\right)\right|^2-\left|\frac{1}{\mathrm{M}}\sum_{\mathrm{m}=1}^{\mathrm{M}}\mathrm{V}_h\left(\mathrm{m}\right)\right|^2$. Thus, PR is the ratio between coherent power and the power in all the other spectral lines; therefore, PR should be larger for ground clutter than weather signals.

Figure 2-10 shows the joint 2D PDF of PR_h and PR_v. Although, the wave scatters from randomly distributed hydrometers do not yield any coherent wave field in the forward direction, the deterministic scatterers such as ground clutter cause coherent wave field [19]. Therefore, this characteristic can be used as a discriminant function to distinguish clutters from weather signals.

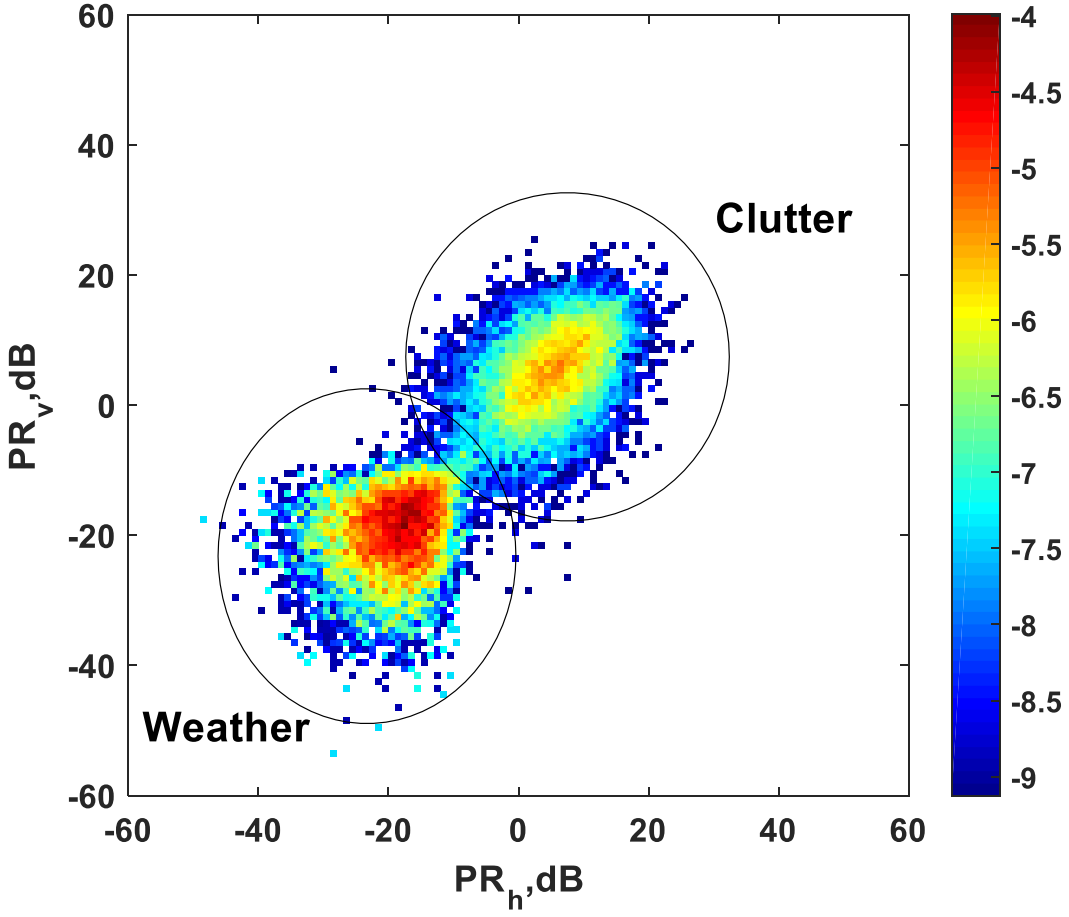

Figure 2-10: The PDF of power ratio, dB

The joint PDF of power ratio and Lag-1 or Lag-6 correlations for weather and clutter signals are shown in Figure 2-11. As normally expected, Lag-1 or Lag-6 correlations for the deterministic scatterers such as ground clutters, are almost the same. Because for the deterministic medium, the relative random motion is much less than half a wavelength. Therefore, the correlation between different Lags still remains near one. However, for the randomly distributed hydrometers, the correlations are reducing for higher Lag correlations.

The joint PDF of power ratio and Lag-1 or Lag-6 correlations for weather and clutter signals are shown in Figure 2-11. As normally expected, Lag-1 or Lag-6 correlations for the deterministic scatterers such as ground clutters, are almost the same. Because for the deterministic medium, the relative random motion is much less than half a wavelength. Therefore, the correlation between different Lags still remains near one. However, for the randomly distributed hydrometers, the correlations are reducing for higher Lag correlations.

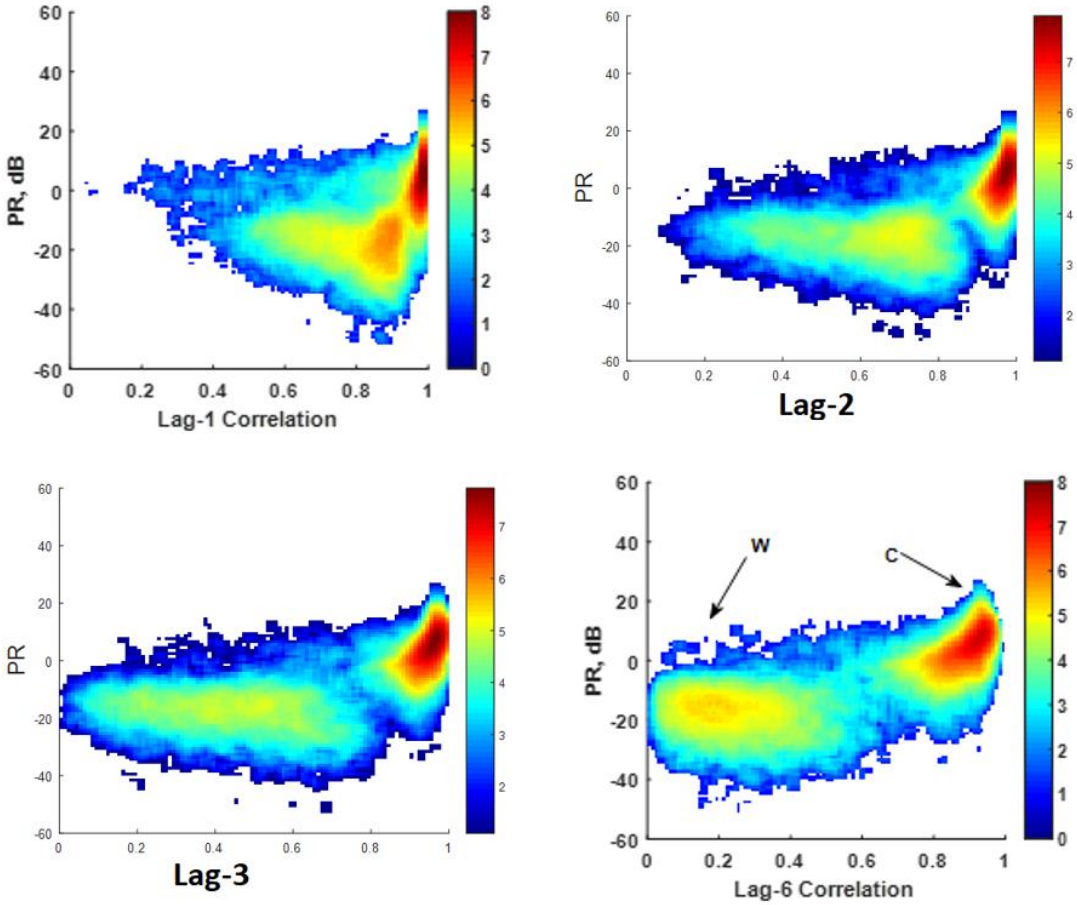

Figure 2-11: The PDF of power ratio versus Lag-1, Lag-2, Lag-3 and Lag-6 correlations versus power ratio

2.2.5 The phase of Dual-Scan Cross-Correlation Coefficient

Figure 2-12 shows the phase of the correlation coefficient between the two scans. It can be seen that ground clutter signals have near-zero values for the phase of the dual scan cross-correlation coefficient. It is clear that the signals from two consecutive scans are almost correlated for clutters and are noncorrelated for weather signals, either for phase or amplitude, because the first and second scans have mostly the same features for fixed scatterers such as ground clutter. However, the second scan is not correlated to the first scan for randomly distributed hydrometers. Thus, this PDF can be used as another discriminant function to detect clutters from weather signals.

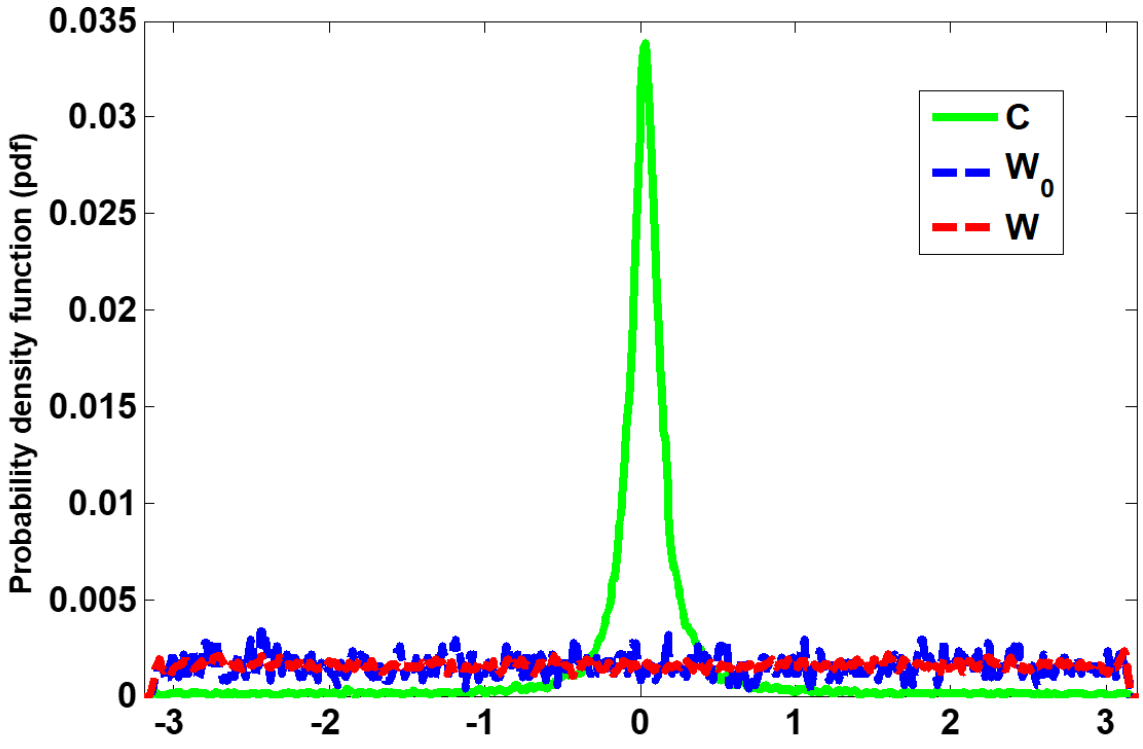

Figure 2-12: The PDF of the phase of Dual-Scan Cross-Correlation

2.2.6 Differential Phase

The differential phase between H-polarization and V-polarization is defined as:

$$\Delta\phi = \frac{1}{M}\sum_{m=1}^{M}\left(\phi_h(m) - \phi_v(m)\right) \tag{2.5}$$

Figure 2-13 shows the PDFs of the differential phase based on the training data. It is expected that the differential phase for clutter has a wider range in comparison to weather signals. The wave scattering from randomly distributed hydrometers yields a random dependent phase for H-pol and V-pol, based on the hydrometer shape. However, wave scattering from deterministic scatterers such as ground clutters yields an independent phase for H-pol and V-pol, with a non-constant differential phase, as shown in Figure 2-13. This constant differential phase for weather signals may change based on the weather conditions and radar parameters, and can be easily updated.

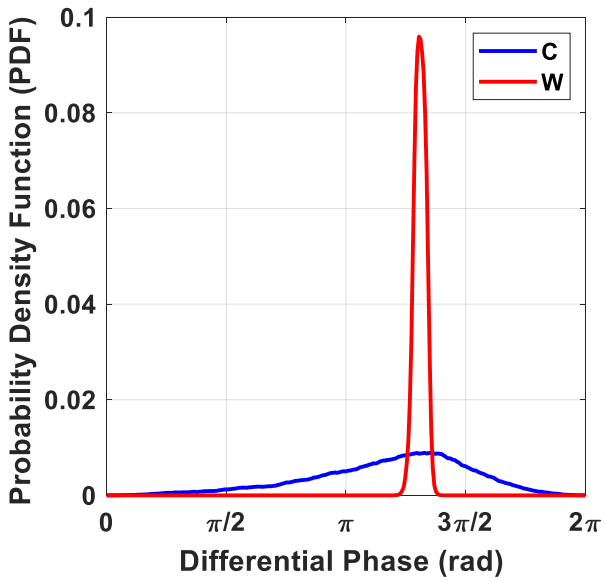

Figure 2-13: The PDF of the differential phase between H-polarization and V-polarization

Chapter 3

Dual-pol Dual Scan (DPDS) Clutter Detection Algorithm

3.1 Dual-Polarization and Dual-Scan (DPDS) Detection Algorithm

A dual-polarization and dual-scan (DPDS) classification algorithm is presented in this chapter for clutter detection. Two consecutive scans of dual-polarization radar signs are jointly processed to estimate auto- and cross-correlation functions. Radar discriminants are then defined and estimated in order to separate clutter from weather based on their physical and statistical properties. An optimal Bayesian classifier is used to make a decision on clutter presence from the estimated discriminant functions. The DPDS algorithm is applied to the data collected with the KOUN polarimetric radar, and compared with the existing detection methods. It is shown that the DPDS algorithm yields a higher probability of detection and false alarm rate in clutter detection.

In this chapter, three discriminant functions for DPDS clutter detection are considered. The discriminant functions for the DPDS algorithm are the differential reflectivity (Z_{DR}), dual scan cross-correlation coefficient (ρ_{12}), dual-pol cross-correlation coefficient (between H and V-polarization) (ρ_{hv}) signals. The Bayesian classifier is used to combine discriminant functions to detect clutter from weather signals, which includes estimation and aggregation of discriminants for decision making.

Our training data were collected by the national KOUN (WSR-88D) radar on two different days—this data was used to find the probability density functions (PDFs) for the discriminant functions. The training weather data were collected at 13:08 UTC on 9 February 2011. The training clutter dataset was collected by the KOUN radar in clear weather conditions, at 00:46 UTC on 4 February 2011. It should be noted that we created a controlled training data set by matching and combining to create almost

pure clutter data at 00:46 UTC on 4 February 2011, and pure weather data at 13:08 UTC on 9 February 2011.

Two sequential azimuthal scans with different pulse repetition times (PRTs) are used in the volume coverage patterns (VCPs) of the WSR-88D to mitigate range–velocity ambiguities [48]. The first azimuthal scan collects voltage samples data using long PRT (Ts1 = 3.10 ms); and the second scan at the same elevation angles uses a short PRT (Ts2 = 0.973 ms), as shown in Figure 3-1. To implement the scan-to-scan method, we down-sampled the short PRT data to be matched with its corresponding long PRT data. Because the WSR-88D records the azimuth of each voltage sample, we were able to select those short PRT samples that are nearest in azimuth to the corresponding, long PRT samples.

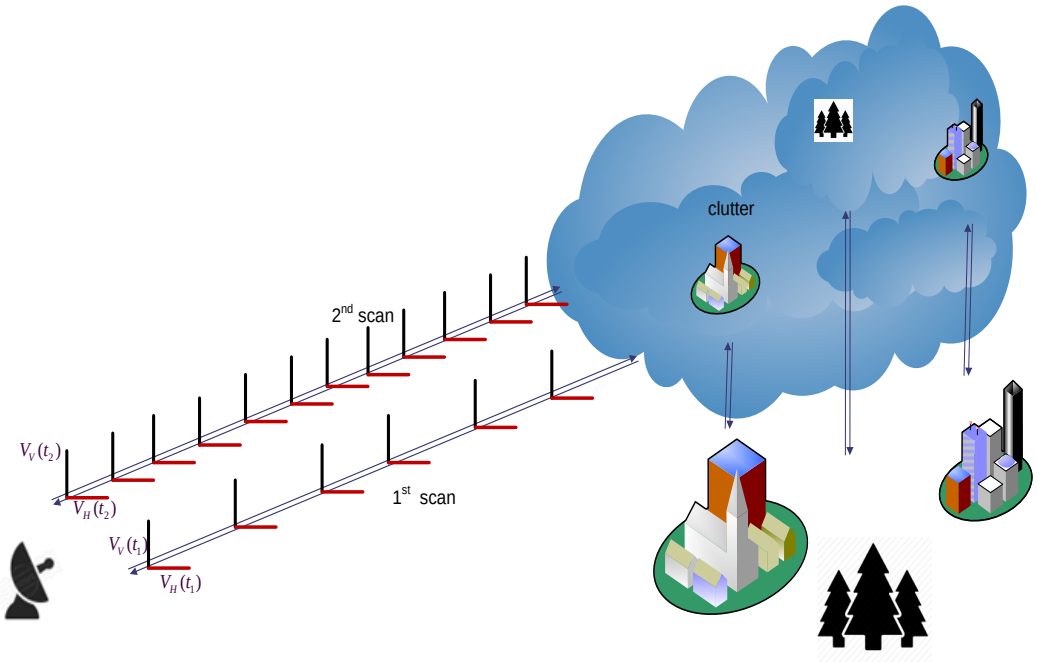

Figure 3-1: Dual-polarization and dual-scan (DPDS) weather radar.

Weather I/Q data were edited by excluding the resolution volumes showing SNR < 20 dB. The 20 dB SNR threshold is applied to produce data to mitigate and avoid noise effects. The weather data consist of two scans at the same elevation angle (i.e.,

1.49°) separated by about 36 s. The clutter data were collected at 00:46 UTC on 4 February 2011 with two scans at the same elevation angle (0.5°) separated by about 76s under clear air conditions. Ground clutter I/Q data were edited by deleting the resolution volumes showing mean Doppler velocities $|v_r| \geq 1$ m·s−1 and CNR (Clutter to Noise Ratio) < 3 dB. This deletion provided a cluttered field not contaminated from moving objects on the ground or airborne (e.g., birds and aircraft).

Reliable ground truth is an important issue to evaluate the performance of clutter detectors [9, 10]. To obtain the class label of each resolution volume for obtaining the training data and discriminant PDFs, CMD has been used as suggested by [49]. Although the performance of the CMD algorithm is entirely acceptable for our controlled training data, all PDFs were updated and modified by the DPDS algorithm.

3.2 Optimal Bayesian Classifier

Simple Bayesian Classifiers assume that the effect of an attribute value on a given class is independent of the values of the other attributes, and it is called class-conditional independence. The Bayesian Classifiers works as follows [50]:

1. Suppose *D* is a training set of tuples and their associated class labels. Each tuple consists of an *n*-dimensional attribute vector $\boldsymbol{X} = (x_1, x_2, ..., x_n)$, and an *n*-dimensional observation vector made on *n* attributes $\boldsymbol{X}^{\mathrm{O}} = (x_1^{\mathrm{O}}, x_2^{\mathrm{O}}, ..., x_n^{\mathrm{O}})$ where the superscript ‘O’ signifies observation. The attribute is equivalent to discriminant in this dissertation. For example, the differential reflectivity can be an attribute for polarimetric radar ground clutter detection.

2. Suppose that there are m classes, C_1, C_2, … C_m. For example, ground clutter is a class that differs itself from weather signal, which is another class. Given an observation of the attributes, the classifier will predict that $\boldsymbol{X} = \boldsymbol{X}^{\mathrm{O}}$ belongs to the class having the highest posterior probability, conditioned on $\boldsymbol{X} = \boldsymbol{X}^{\mathrm{O}}$. That is, the SBC predicts that $\boldsymbol{X} = \boldsymbol{X}^{\mathrm{O}}$ belongs to the class C_i if and only if $p(C_i | \boldsymbol{X} = \boldsymbol{X}^{\mathrm{O}}) > p(C_j | \boldsymbol{X} = \boldsymbol{X}^{\mathrm{O}})$ for $1 \le j \le m$ and $j \ne i$. According to Bayes' theorem [51]:

$$p(C_i \mid \boldsymbol{X} = \boldsymbol{X}^{\mathrm{O}}) = \frac{p(\boldsymbol{X} = \boldsymbol{X}^{\mathrm{O}} \mid C_i)\, p(C_i)}{p(\boldsymbol{X} = \boldsymbol{X}^{\mathrm{O}})} \tag{3.1}$$

3. As $p(\boldsymbol{X} = \boldsymbol{X}^{\mathrm{O}})$ is constant for all classes [50], from (3.1) we have:

$$p(C_i \mid \boldsymbol{X} = \boldsymbol{X}^{\mathrm{O}}) \propto p(\boldsymbol{X} = \boldsymbol{X}^{\mathrm{O}} \mid C_i)\, p(C_i) \tag{3.2}$$

4. Given datasets with many attributes, it would be computationally expensive to calculate $p(\boldsymbol{X} = \boldsymbol{X}^{\mathrm{O}} \mid C_i)$. The simple assumption of class-conditional independence is made to reduce computations involved, which presumes that the attributes' values are conditionally independent of one another, given the class label. Thus,

$$p(\boldsymbol{X} = \boldsymbol{X}^{\mathrm{O}} \mid C_i) = p(x_1 = x_1^{\mathrm{O}} \mid C_i) \times p(x_2 = x_2^{\mathrm{O}} \mid C_i) \times \cdots \times p(x_n = x_n^{\mathrm{O}} \mid C_i) \tag{3.3}$$

   The probabilities $p(x_1 = x_1^{\mathrm{O}} \mid C_i)$, $p(x_2 = x_2^{\mathrm{O}} \mid C_i)$,…, $p(x_n = x_n^{\mathrm{O}} \mid C_i)$ can be obtained from the training tuples.

5. To predict the class label of $\boldsymbol{X} = \boldsymbol{X}^{\mathrm{O}}$, $p(\boldsymbol{X} = \boldsymbol{X}^{\mathrm{O}} \mid C_i)$ is evaluated for each class. The classifier predicts that the class label of $\boldsymbol{X} = \boldsymbol{X}^{\mathrm{O}}$ is the class C_i if and only if

$$p(\boldsymbol{X} = \boldsymbol{X}^{\mathrm{O}} \mid C_i)\, p(C_i) > p(\boldsymbol{X} = \boldsymbol{X}^{\mathrm{O}} \mid C_j)\, p(C_j),\ 1 \le j \le m \text{ and } j \ne i \tag{3.4}$$

Thus, the predicted class is the class C_i for which $p(\boldsymbol{X} = \boldsymbol{X}^{\mathrm{O}} \mid C_i)\, p(C_i)$ is the maximum.

3.3 Performance Evaluations of DPDS

In this section, the performance of the DPDS algorithm is evaluated using the testing control data sets collected by the KOUN (WSR-88D) radar at 13:07, 13:08 and 14:02 UTC on 9 February 2011, and 00:46 UTC on 4 February 2011 with two scans at the same elevation angle. The same procedure has been used to obtain the ground truth, from the combination of pure clutter and pure weather data for the controlled testing data sets. Therefore, the ground truth will be used as a reference for clutter detection algorithms. The ground truth can also be used to find the CSR. By changing the CSR, we can compare the performances of detection algorithms as a function of CSR.

We will compare the DPDS algorithm to previous clutter detection algorithms, such as DP, DS, CMD, presented in [10, 20, 30, 52]. Figure 3-3 shows the statistical characteristics of the DPDS algorithm. To evaluate the performance of DPDS, the numbers of true positives (TP), false negatives (FN), false positives (FP), and true negatives (TN), as well as the probability of detection P_D, and the probability of false alarm P_{FA} are calculated.

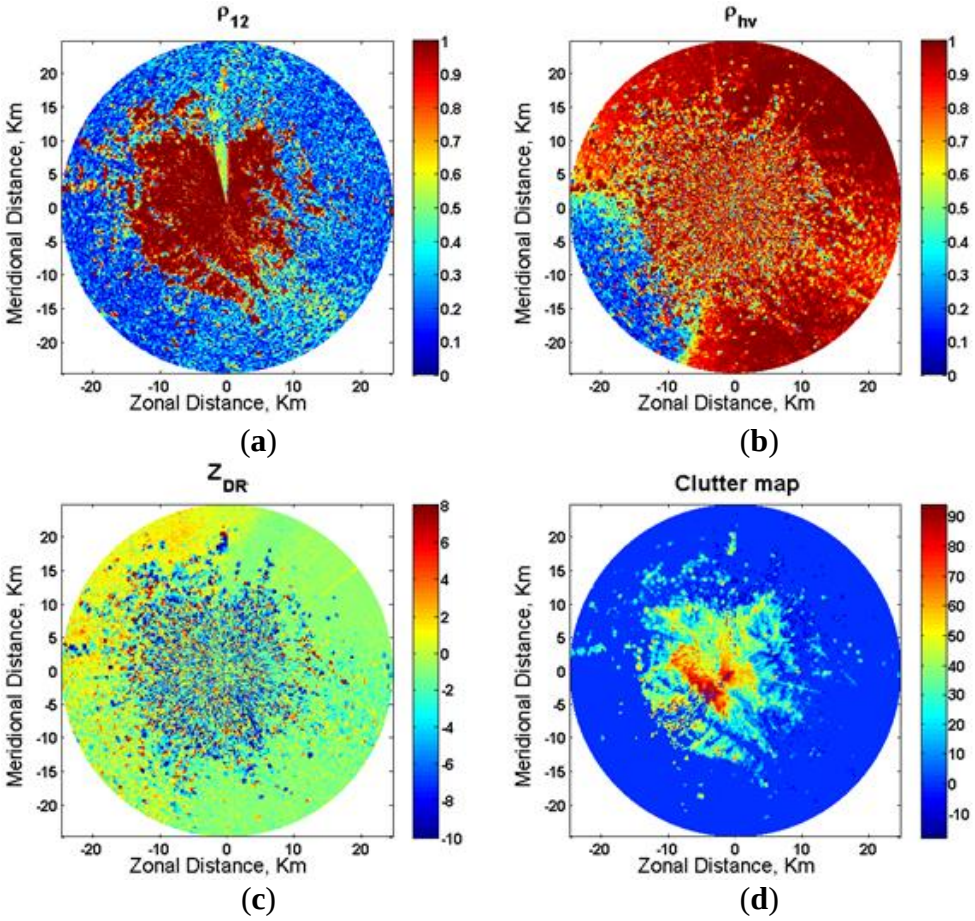

Figure 3-2: Pure weather signals from KOUN (13:08 UTC on 9 February 2011) mixed with pure ground clutter (00:46 UTC on 4 February 2011). (a) Dual-scan cross-correlation coefficient; (b) dual-polarization co-polar cross-correlation coefficient; (c) differential reflectivity; (d) ground truth clutter map.

"True" or "False" stand for truly or falsely detected by the algorithm, and "Positive" or "Negative" stand for the clutter decision made by the algorithm. The probability of detection and false alarm (i.e., P_D and P_{FA}) are generally calculated as:

$$P_D = \frac{TP}{TP + FN} \quad , \quad P_{FA} = \frac{FP}{FP + TN} \tag{3.5}$$

Figure 7 illustrates the probability of detection (P_D) versus clutter to signal ratio for DPDS, DP, DS, and CMD algorithms. It is clear P_D rate should increase with increasing clutter power or CSR. All radars do not have the ability to collect dual scan data. However, the same procedure can be implemented to detect clutter using other discriminants such as power ratio (PR—defined as the ratio between coherent and incoherent power). Figure 3-4, illustrates the clutter map of the ground truth along with CSR, and clutter maps of DPDS, DP, DS, and CMD algorithms. As can be seen from this figure, the DPDS is most similar to ground truth in comparison to other algorithms. Additionally, it was shown in Figure 3-3 that the difference between P_D of DPDS and other detection algorithms increased with decreasing CSR. Therefore, the DPDS improvement gain is clearly observable in the resolution of the clutter map, in Figure 3-2, especially for the low values of CSR. It also can be seen from Figure 3-2 that for high CSR values, the DPDS algorithm has better performance in comparison to DP, DS, and CMD algorithms, respectively.

In Table 3.1, we list the probability of false alarm (PFA) for the three controlled testing data sets, collected by KOUN at 13:07, 13:08 and 14:02 UTC on 9 February 2011. From Table 3.1, we can see that all four algorithms produce low P_{FA}; the reason is that there are many more pure weather signal pixels. This table shows that the DPDS algorithm produces the lowest P_{FA} with the highest P_d compared to DP, DS, and CMD algorithms.

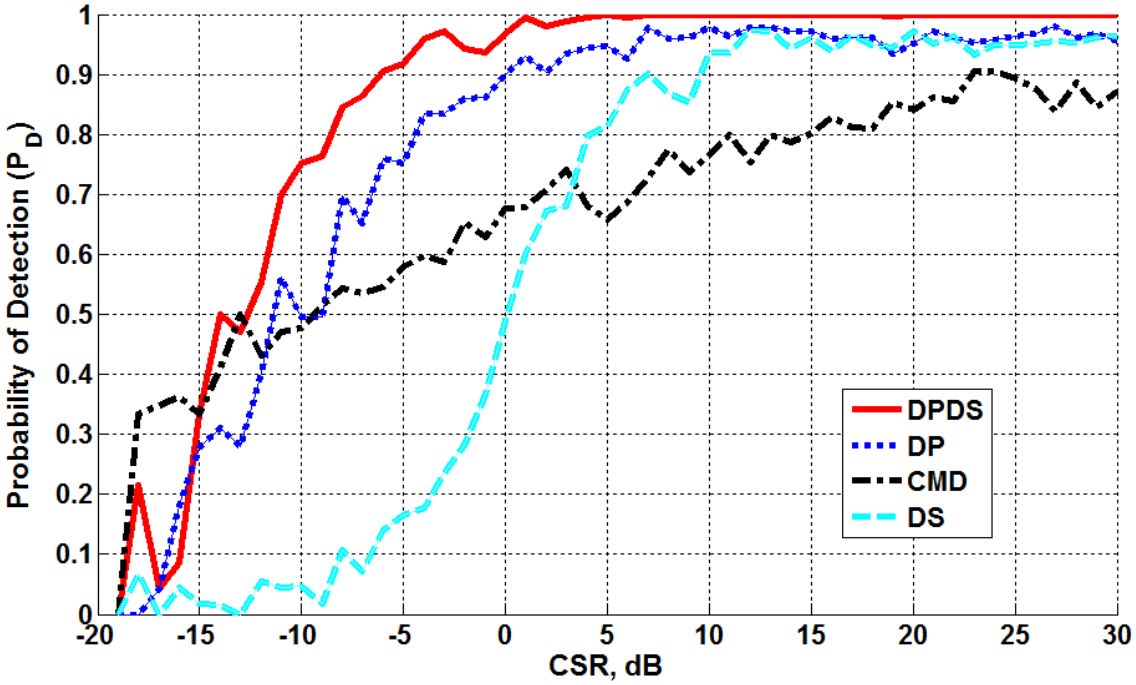

Figure 3-3: The probability of Detection (P_D) *vs.* CSR.

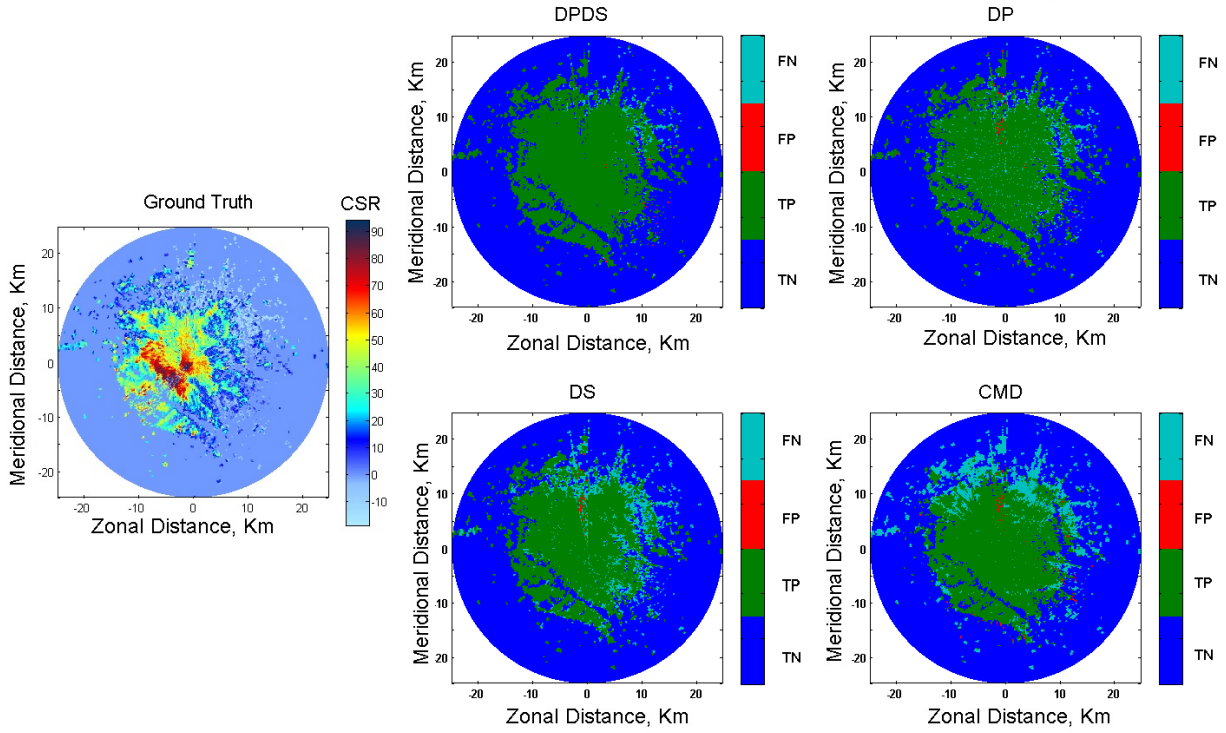

Figure 3-4: Clutter Maps using: DPDS, DP, DS, and CMD algorithms, and Ground truth.

Table 3.1: P_{FA} for three testing data by using the DPDS, DP, DS, and CMD algorithms.

Data-Time, UTC	CMD	DS	DP	DPDS
13:08	0.7770%	0.3387%	0.4782%	0.00%
13:07	0.5525%	0.2130%	0.3195%	0.00%
14:02	0.6346%	0.2363%	0.3443%	0.00%

There are various dual-polarization clutter detection algorithms, and they can take advantage of the polarization diversity of the scattering properties to discriminate clutter from weather signals [15-17]. The Z_{DR} and ρ_{hv} as discriminant functions have an overlapped range between clutter and weather PDFs, as shown in Figure 2-8 and Figure 2-4. Also, the peak values of the weather and clutter PDFs are in the same regions (i.e., near-zero for Z_{DR} and near one for ρ_{hv}). Furthermore, it is shown that weather PDFs have larger peak values than clutter. Consequently, it is clear that the clutter with the near-zero Z_{DR} values and/or near one ρ_{hv} values most likely would be detected as weather instead of clutter and it can undoubtedly increase the detection error rates and reduce the probability of detection for DP algorithm. In [20], the scan-to-scan or dual-scan (DS) algorithm is introduced for clutter detection and considered the cross-correlation coefficient between consecutive scans as a discriminant function. This study shows that the correlation time of radar signals from hydrometers is typically much shorter than that of clutter [20].

Chapter 4

Ground Clutter Detection Using Phase Fluctuation Index

Our aim in this chapter is to develop a ground clutter detection algorithm to provide more representative weather radar observations. The discriminant function based on the phase fluctuation index (PFI) is introduced to achieve better performance for clutter detection algorithms. Statistical properties of the phase fluctuation index for pure weather and ground clutter are presented. A Bayesian classifier is used to make an optimal decision to detect clutter mixed with weather echoes. The performance improvements are demonstrated by applying the PFI detection algorithm to radar data collected by the WSR-88D polarimetric weather radar. Our proposed clutter detection algorithm is compared to several other detection algorithms and reveals the PFI algorithm yields a higher probability of detection.

4.1 Introduction

It is worth mentioning that using several discriminant functions to make the decision for the classification problem can increase the computational complexity and processing time. Therefore, the PFI algorithm is used to improve the detection performance and reduce the error rate and the computational complexity. The PFI algorithm is based on the phase fluctuations index, and it is found that this discriminant function has good separation between clutter and weather signals even for the low values of the CSR. Numerical simulations and theory show the phase of weather signal is typically a rapidly varying function for echoes from each resolution volume [4, 5], whereas the phase of the ground clutter is typically slowly varying. Thus, the fluctuations of the signal phase for each resolution can be considered as a robust discriminant function to detect clutter. We show that the probability density

functions (PDF) of the PFI for weather and clutter signals are entirely separated using PFI and thus can effectively detect clutter mixed with weather echoes with the highest probability of detection compared to other detection algorithms.

4.2 Phase Fluctuation Index (PFI)

The synthesized PPI dataset (see chapter 2) is used to compare clutter detection performance for the PFI and other detection algorithms with ground truth. These specially collected and edited clutter and weather data were also used to find the PFI PDFs as the clutter detection discriminant functions, from pure weather and clutter data. The nearly pure clutter data set was collected in clear air conditions by the KOUN (WSR-88D) radar, at 00:46 UTC on 4 February 2011, and nearly pure weather data were collected on at 13:08 UTC on 9 February 2011.

The I/Q data for each resolution volume is represented as the received complex voltage sample, and the phase (φ , radian) can be calculated as: $\phi = \measuredangle V, where\ V = X - jY = Ae^{-j\phi}$. Figure 4-1 shows the statistical properties of the real part, imaginary part, amplitude and phase of the received complex voltage. In [4, 5], it is demonstrated that the real (*X*) and imaginary (*Y*) parts follow the Gaussian distribution and the amplitude (*A*) follows the Rayleigh distribution. However, the statistical distribution for the phase is uniform on [-π , π]. Also, it is proved in [4, 5] that based on the central limit theorem, the I and Q (Real and Imaginary parts of the received complex voltage) have a Gaussian distribution with zero mean for echoes from hydrometers.

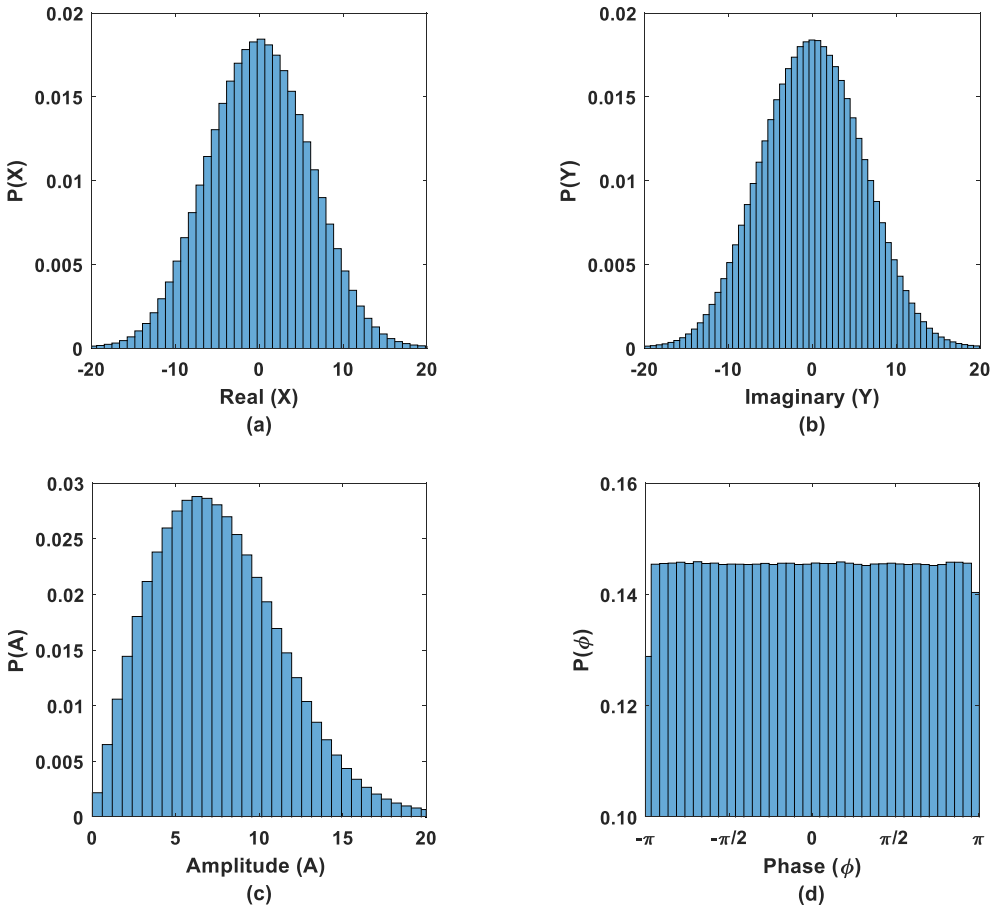

Figure 4-1: Histogram of statistics for the wave scattering from KOUN data a) Real part (*X*), b) Imaginary part (*Y*), c) Amplitude (*A*) and d) Phase of the complex voltage (V) for the I/Q data

Also, it is shown that although the I and Q are independent random variables, the random process controlling the changes of I and Q are not independent and the random processes controlling the changes in I and Q are correlated if sample spacing Ts is sufficiently short so that each sample is correlated with previous one. Therefore, the phase (based on the correlated changes on the I and Q) is a random process and there is a correlation on the changes of the phase of echoes from hydrometers and clutter (but Ts must be short compared to the correlation time). It should be noted that

the ranges of signal's Doppler velocity used in the testing control data are between [-8,8], and the spectrum width range are between [0,5], as shown in Figure 4-2.

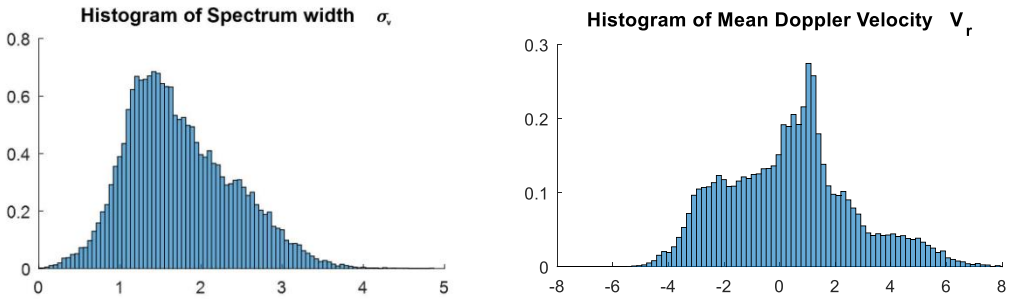

Figure 4-2: Histogram of the Doppler velocity and the spectrum width for the testing data collected by KOUN radar

Wave scattering from the randomly distributed hydrometers yields a rapidly fluctuating phase due to turbulence and mean radial velocity. The phase fluctuations have both a random component due to turbulence and a quasi-deterministic component due to the mean radial velocity as shown in Figure 4-3. Most if not all of the rapid fluctuations seen in Figure 4-3 are caused by phase folding of the quasi-deterministically varying phase (i.e., the continuous decrease on the downward slopes) associated with the mean Doppler velocity, and the phase fluctuations superimposed on the quasi-deterministically varying phase is due to the width of the weather signal spectrum. However, the wave scattering from fixed scatterers on the ground produces a relatively slow fluctuation in phase due to the scanning beam, as shown in Figure 4-3a. The radar antenna is rotating azimuthally with a constant elevation angle; thus, azimuth is equivalent to sample time, as shown in Figure 4-3. The blue lines in Figure 4-3 represent the phase of I/Q data for pure clutter and weather data.

As can be seen from Figure 4-3, the phase fluctuations for weather signals are more pronounced than that for clutter. Figure1b and Figure1c show the fluctuating

phase for the non-zero mean Doppler and zero mean Doppler of hydrometeors. As can be seen from Figure 4-3c, the phase fluctuations for W_0 are still stronger than that for clutter echoes.

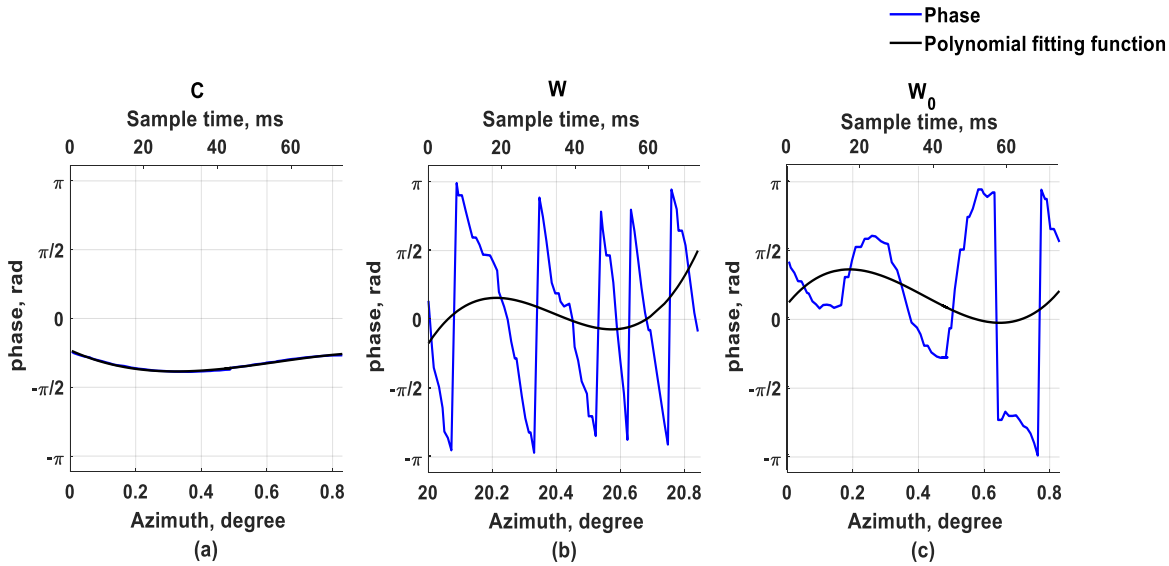

Figure 4-3: Phase of the I/Q data and the 3-order polynomial fitting functions for a) pure clutter (C), b) pure non-zero mean Doppler velocity weather (W), and c) pure narrow-band zero mean Doppler velocity weather (W_0)

4.3 Polynomial Fitting Function

Therefore, an index for phase fluctuation needs to be defined to discriminate clutter from weather signals (W, W_0). In this chapter, the PFI is calculated by defining the 3-order polynomial fitting function and calculating the distance of the phase to its corresponding fitting function, for echoes from each resolution volume. In Figure 4-3, black lines represent the 3-order polynomial fitting function for clutter and weather echoes. The 3-order polynomial function is defined as:

$$V_p(n) = p_3 n^3 + p_2 n^2 + p_1 n + p_0 \tag{4.1}$$

where *n* signifies the echo sample number. The best-fitting coefficients (i.e., p_0, p_1, p_2, p_3) can be obtained based on the least-squares (LS) approach. It is found that the 3-order polynomial fitting function can achieve the highest performance with the lowest complexity compared to other orders of polynomial functions, as shown in Figure 4-4.

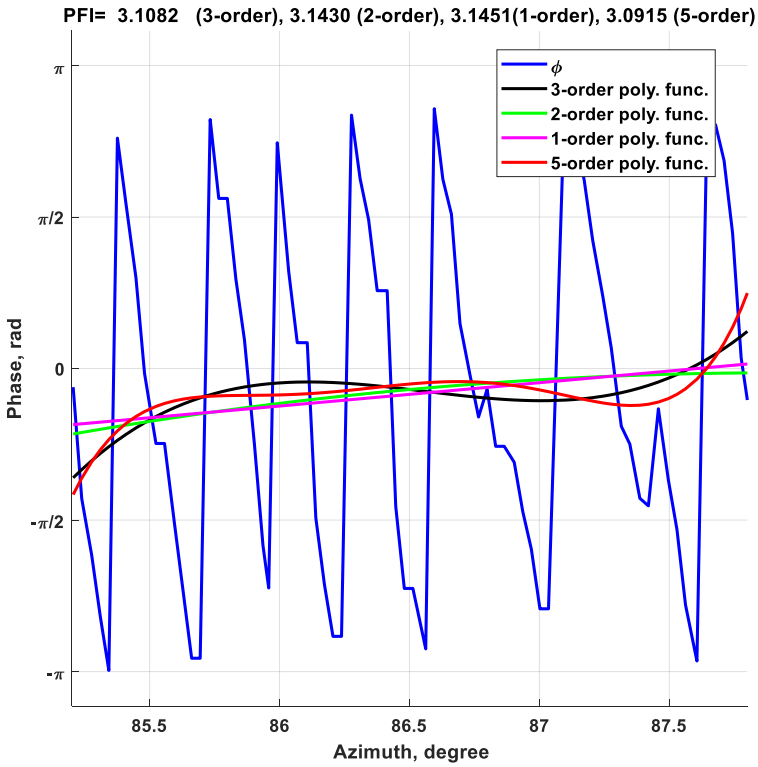

Figure 4-4: Phase of the pure weather I/Q data and the 3-order polynomial fitting function compared to 2-order, 1-order, and 5-order polynomial fitting functions

The 3-order polynomial function can easily capture the transitions of the clutter phase compared to 2-order or 1-order polynomial function (or mean value) and can keep the PFI values under one for clutter. Furthermore, there is not that much improvement for the discriminant functions by using higher orders (4-order or 5-order polynomial functions), however, using higher orders can increase the computational

complexity of the algorithm. Therefore, we considered 3-order polynomial as the best polynomial fitting function for the PFI. Figure 4-4 shows the PFI values based on the 1-, 2-, 3-, 5-order polynomial functions. As can be seen from this figure, the PFI value for weather is almost 3.1 for all different orders of the polynomial fitting function. As can be seen from Figure 4-5, the PFI value for clutter based on 3-order polynomial fitting function is around 0.28, whereas the PFI is around 0.51 for 1-order (around twice).

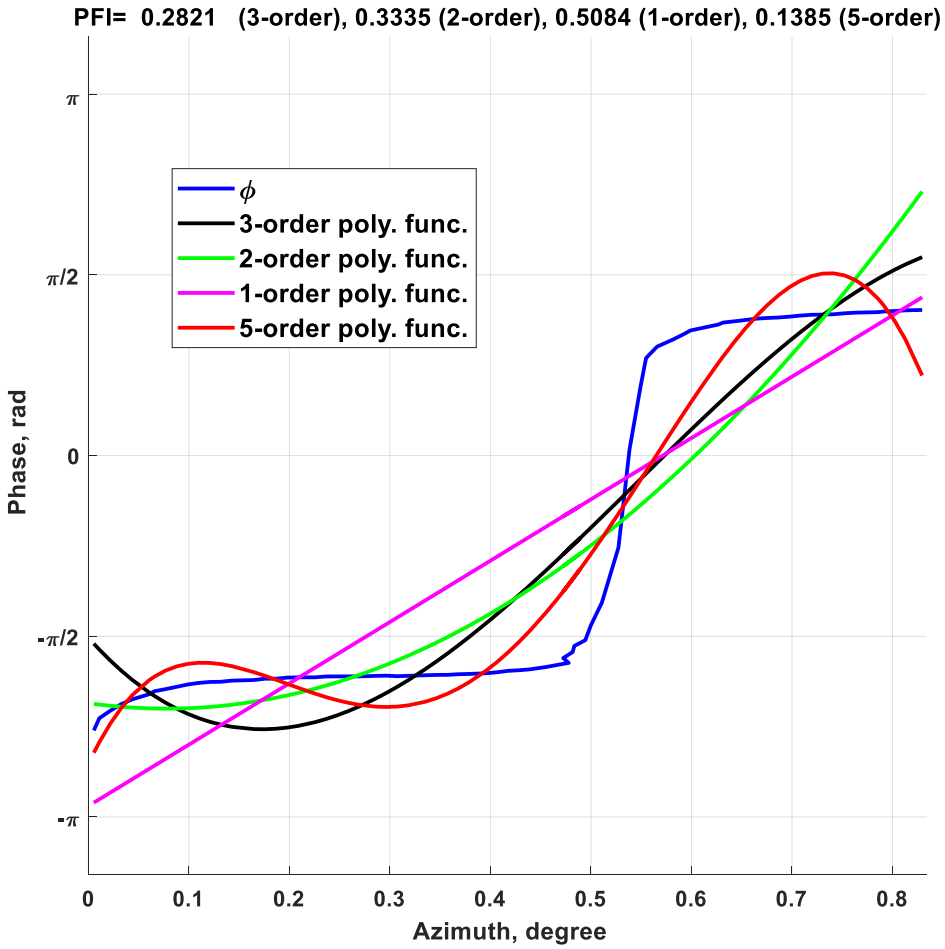

Figure 4-5: Phase of the pure clutter I/Q data and the 3-order polynomial fitting function compared to 2-order, 1-order, and 5-order polynomial fitting functions

It can be seen that the distance to the fitting function for the weather signals is much larger than that for clutter. Therefore, we define the phase fluctuation index for each polarization as:

$$PFI_h = \frac{1}{M}\sum_{n=1}^{M}\left|\measuredangle V_h(n) - \measuredangle V_p(n)\right|^2$$
$$PFI_v = \frac{1}{M}\sum_{n=1}^{M}\left|\measuredangle V_v(n) - \measuredangle V_p(n)\right|^2 \quad (4.2)$$

The joint 2D PDF of the PFI_h and PFI_v is shown in Figure 4-6a. The PDF is obtained from the specially collected and edited data sets for nearly pure weather and clutter, and the CSR range is between -45dB and 20dB for this figure. As can be seen from this figure, ground clutter and weather PDFs are separated by using the phase fluctuation index as a discriminant. Therefore, this discriminant function can reduce the detection error rate and improve the probability of detection compared to existing algorithms. Also, there is no overlapped area between clutter and weather signals for the CSR values over 0dB. Hence, this characteristic can make the PFI method the best to detect ground clutter compared to other detection methods. The next section shows the performance improvements for clutter detection based solely on the PFI discriminate.

Furthermore, it can be seen from this figure that weather (W) PDF data is tightly clustered about the 1:1 line suggesting H and V for W echoes have a relatively high correlation coefficient ρ_{hv} (i.e., ρ_{hv} for W is more than 0.85 with the peak located at 0.995[18, 19]). However, it is likely the precipitation in February is frozen and the

co-polar correlation is less than it is for rain, and the PFIs for H and V fall farther from the 1:1 line (if H and V echoes were perfectly correlated all W points would fall on the 1:1 line). Ground clutter has a much weaker co-polar correlation (i.e., ρ_{hv} has large spread values between 0.5-0.99 for clutter [18, 19]), and the PFIs for H and V are not as tightly clustered about the 1:1 line. Thus, the separation space between the 2D PDFs of clutter and weather is larger than that for 1D space. Therefore, the 2D-PFI detection algorithm can effectively improve the performance of clutter detection to achieve the highest probability of detection compared to 1D-PFI and other existing detection algorithms.

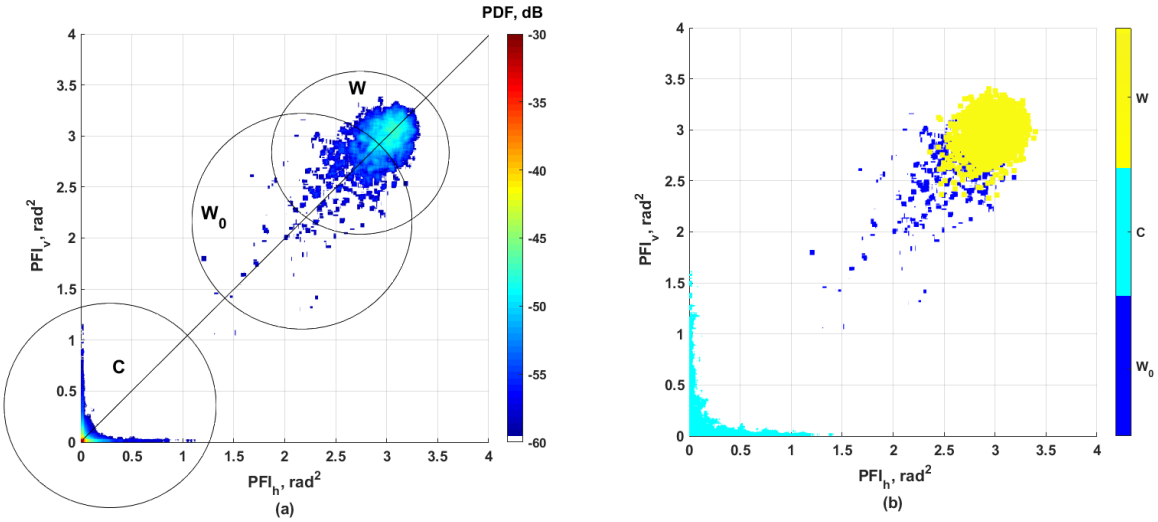

Figure 4-6: Joint probability density function of the *PFI* for H-pol and V-pol for clutter and weather classes

To examine the effect of the clutter power on the PFI, a pure clutter and pure weather data sets are combined with different CSR values, and the corresponding PFI values are obtained. Figure 3 shows the CSR to the phase fluctuation index. As expected, the PFI is increasing with decreasing the clutter power or CSR.

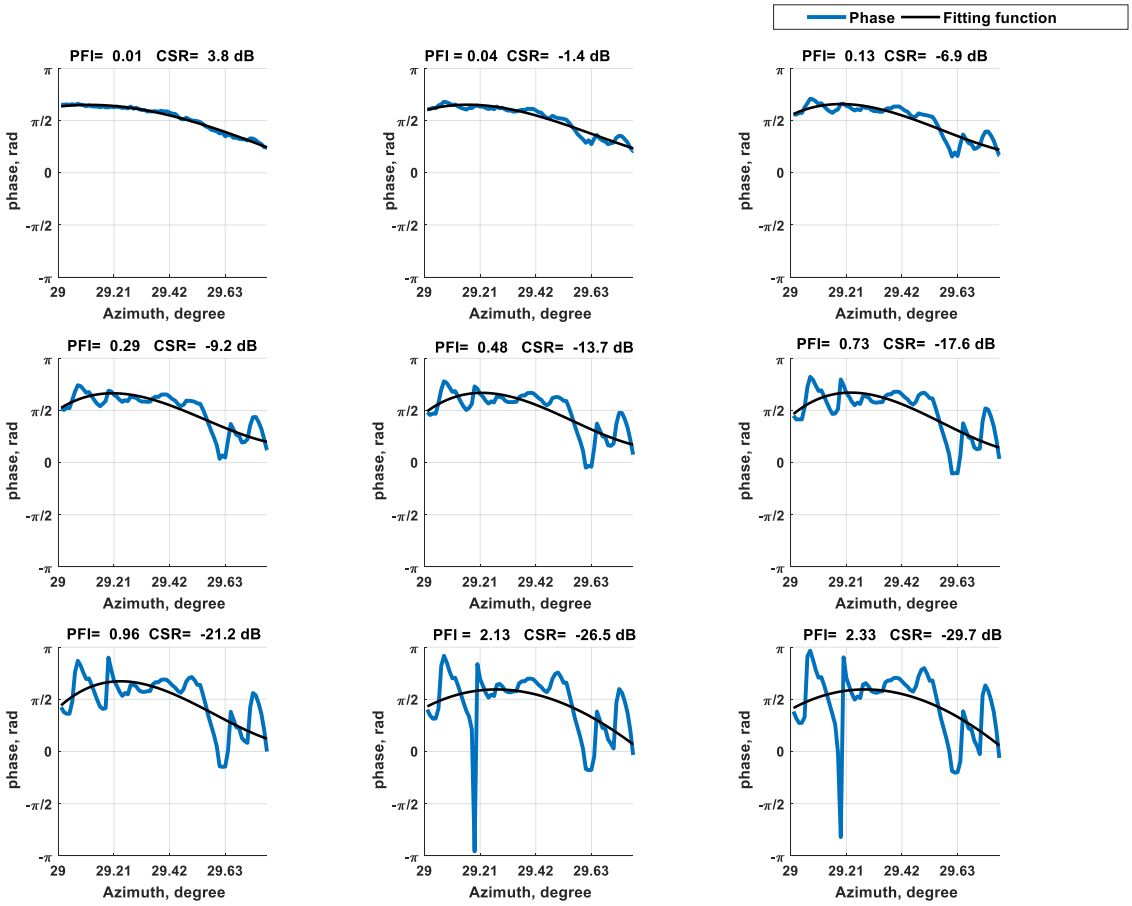

Figure 4-7: Effect of CSR on the PFI_h of W_0 weather signal

4.4 Bayesian PFI Clutter Detection Algorithm

The PDF of the joint (PFI_h, PFI_v) is used as a reference for the optimal Bayesian classifier. It is proved in chapter 2 of [53] that the Bayesian classifier can provide the optimal decision boundary and gives the lowest probability of error. Also, in chapter 2 of [54], it is shown and proved that the Bayesian classifier is optimal with respect to minimizing the classification error probability.

The likelihood function can be obtained from the training dataset for all classes by using the PDF shown in Figure 4-6. Thus, the class conditional densities for each class ($p(\boldsymbol{X} = \boldsymbol{X}^{O} \mid \omega_i)$) can be calculated as:

$$p(\boldsymbol{X} = \boldsymbol{X}^{\mathrm{O}} \mid \omega_{\mathrm{i}}) = p\left(PFI_h^{\mathrm{O}}, PFI_v^{\mathrm{O}} \mid \omega_{\mathrm{i}}\right) \tag{4.3}$$

The class that corresponds to the maximum probability value will be selected as the classification decision. Thus, we can infer that Bayesian classifier assigns $\boldsymbol{X} = \boldsymbol{X}°$ to "C" only if:

$$p(\boldsymbol{X} = \boldsymbol{X}°|\mathrm{C}) > p(\boldsymbol{X} = \boldsymbol{X}°|\mathrm{W}) \text{ and } p(\boldsymbol{X} = \boldsymbol{X}°|\mathrm{C}) > p(\boldsymbol{X} = \boldsymbol{X}°|\mathrm{W}_0) \tag{3.4}$$

Therefore, the detection algorithm is summarized in the following steps:

1) Calculate the signal to noise ratio (SNR) for the current resolution volume. If the SNR is less than 20dB, the current gate is considered not to have a significant signal compared to the noise power, and we compute SNR for the next range resolution volume. Otherwise, go to step 2.
2) Calculate the observed PFI (discriminant function) for the current gate, using the joint PDF:

$$p(\boldsymbol{X} = \boldsymbol{X}^{\mathrm{O}} \mid C) = p\left(PFI_h{}^{\mathrm{O}}, PFI_v{}^{\mathrm{O}} \mid C\right),$$

$$p(\boldsymbol{X} = \boldsymbol{X}^{\mathrm{O}} \mid W_0) = p\left(PFI_h{}^{\mathrm{O}}, PFI_v{}^{\mathrm{O}} \mid W_0\right),$$

$$p(\boldsymbol{X} = \boldsymbol{X}^{\mathrm{O}} \mid W) = p\left(PFI_h{}^{\mathrm{O}}, PFI_v{}^{\mathrm{O}} \mid W\right).$$

3) The data for the current gate is clutter-contaminated if

$$p(\boldsymbol{X} = \boldsymbol{X}^{\mathrm{O}} \mid C) > p(\boldsymbol{X} = \boldsymbol{X}^{\mathrm{O}} \mid W)$$

$$p(\boldsymbol{X} = \boldsymbol{X}^{\mathrm{O}} \mid C) > p(\boldsymbol{X} = \boldsymbol{X}^{\mathrm{O}} \mid W_0).$$

Otherwise, the data is not contaminated and return to step 1 for the next gate.

To compare the performance with other existing detection algorithms, the CSR can be computed from the combination of the pure clutter and pure weather datasets [18]. Figure 4-8 illustrates clutter map, and the ground truth is obtained from the training dataset to be used as a reference for clutter detection algorithms. We will compare the performance of the PFI algorithm with other clutter detection algorithms, such as DPDS, DP, DS, CMD; presented in [10, 18-20], for different values of CSR.

To evaluate the detection performance, the probability of detection (P_D) is calculated for the PFI algorithm. Figure 4-9 illustrates the probability of detection *versus* clutter to signal ratio for DP-DS, DP, DS, and CMD algorithms. It can be seen from this figure that P_D for the PFI algorithm is better than 0.9, for CSR as low as -20 dB whereas the P_D for the other algorithms fall below 0.5. The results of the proposed PFI algorithm are also compared to the PFI algorithm with a 1D discriminant function for the single polarization Doppler radar, and it is clear that the joint 2D discriminant function has a better performance compared to 1D discriminant function, as shown in Figure 4-9.

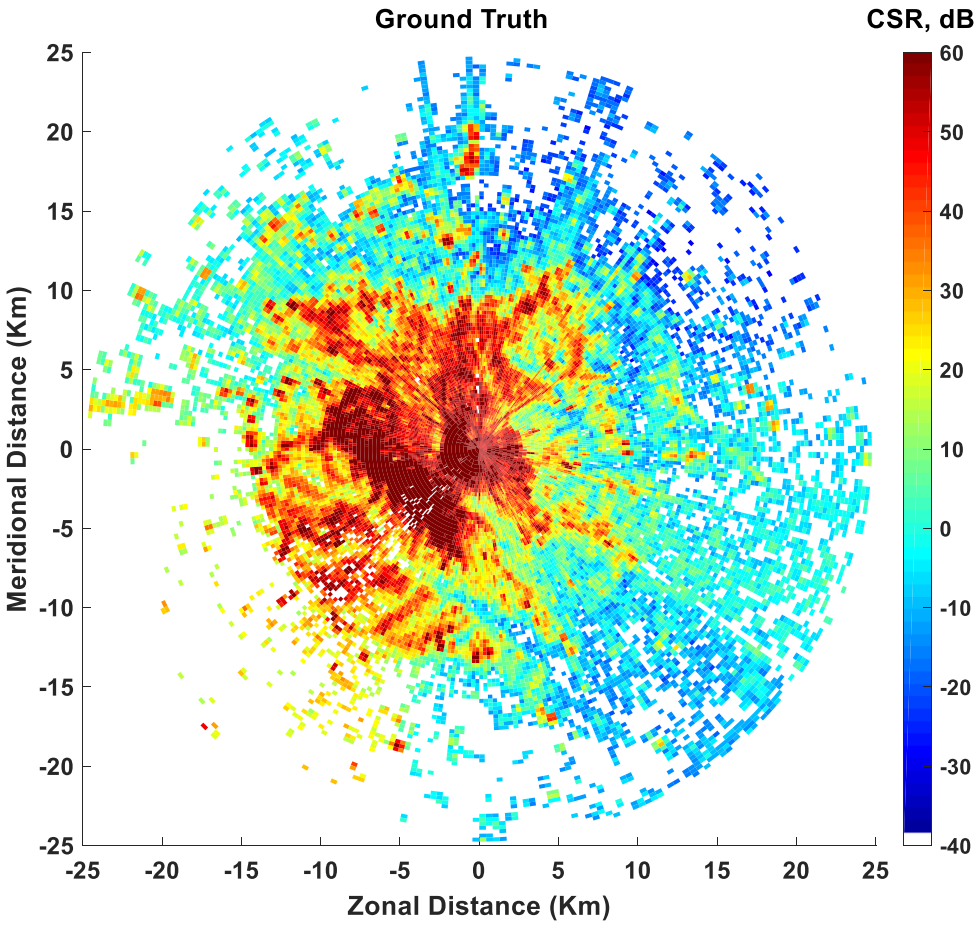

Figure 4-8: Ground Truth; Clutter map

Figure 4-10 illustrates the clutter map of the ground truth and the results of clutter maps for the PFI algorithm compared to the DP-DS [18], DP [19], DS [20], and CMD [9, 10] algorithms. The results of the PFI algorithm are most similar to the ground truth in comparison to other algorithms. In this figure, green points are the "True Positive" samples and represent the number of clutter samples (as shown in the ground truth), which are correctly detected by the corresponding algorithm. Red points ("False Negative") are the samples that are falsely detected as weather instead of clutter, and blue points ("False Positive") are the sample,s that are falsely detected as clutter instead of weather, by each algorithm. It can be seen that the blue points are

not that much because the testing data is the combination of pure weather and pure clutter and the samples are mostly contaminated by clutter. Furthermore, the performance improvement of the PFI algorithm is clearly observable in the resolution of the clutter map in Figure 4-10.

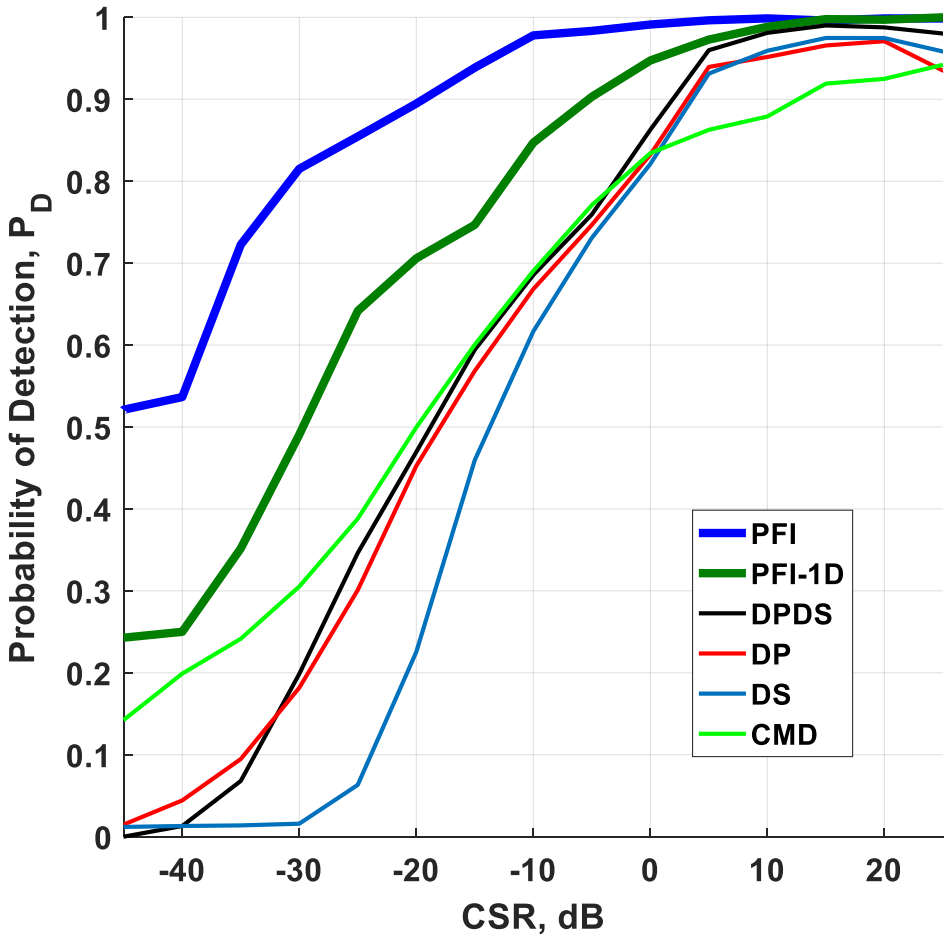

Figure 4-9: Probability of Detection (P_D) *vs.* CSR for *PFI* compared to other clutter detection algorithms.

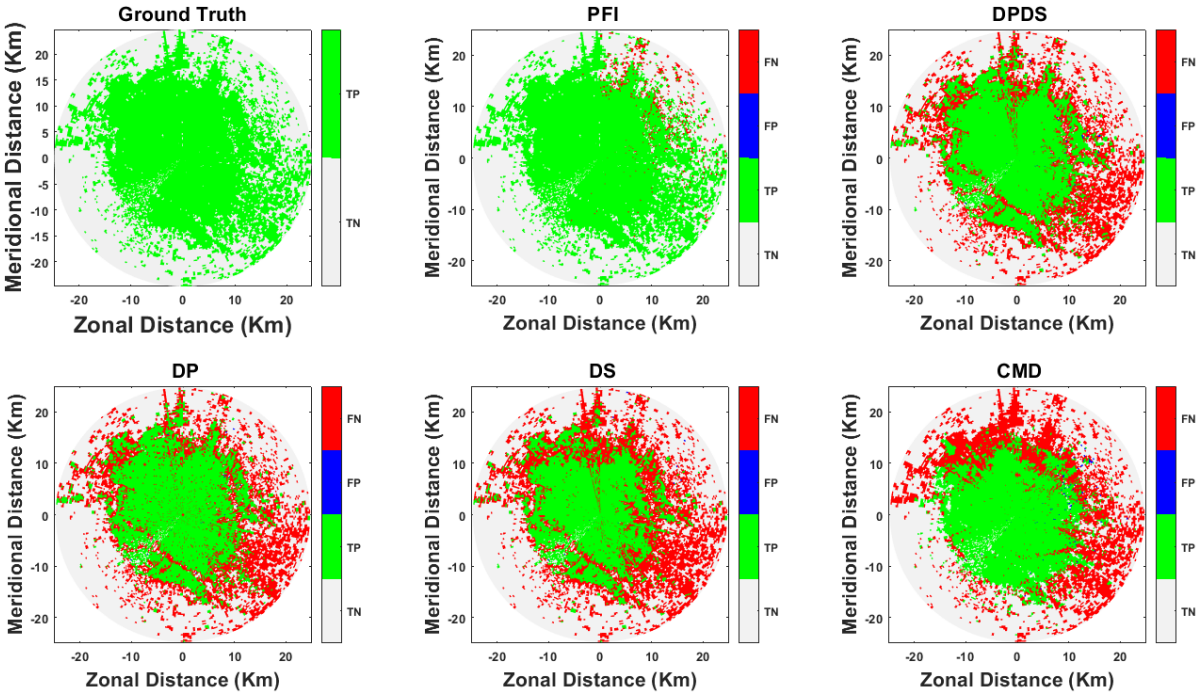

Figure 4-10: Ground truth clutter and clutter detection performance maps using PFI, DPDS, DP, DS, and CMD algorithms

4.5 Conclusions

We have proposed a discriminant function to improve clutter detection algorithms for weather radars. It is demonstrated that the probability density functions of the PFI as a discriminant function for weather and clutter has a very good separation between clutter and weather signals. The PFI property has been analyzed for the proposed detection algorithm, and it is shown that the PFI detects clutter mixed with weather echoes with a P_D better than 90% even for CSR as low as -20 dB. Furthermore, the proposed clutter detection based on PFI can achieve a good performance gain even if dual-polarization data is not available. A simple Bayesian classifier is defined to make an optimal decision for clutter detection. It has been shown via the control dataset that the clutter detection based on the phase fluctuation index can

achieve the best performance as compared to existing detection algorithms such as DP-DS, DP, DS, and CMD. The statistical characteristics obtained from the proposed phase fluctuation index can be extended to design an adaptive target detection algorithm.

The preliminary results for the PFI algorithm are promising. However, the algorithm should be evaluated using other types of weather conditions. The PDFs of discriminant functions may change and thus, may need to be updated based on the weather and clutter conditions, noise effects, and radar parameters, and also, the complete knowledge about the probabilistic structure of the class conditional densities may not be available for the real-time implementations. Therefore, we introduce a method to parameterize the PDF of discriminant functions in the next chapter.

Chapter 5

Detection of Ground Clutter Using a 3D Discriminant Function

In this chapter, a new 3D discriminant function is introduced to improve the performance of the clutter detection algorithms. Phase structure-function (PSF), for H- and V-polarizations is presented as an exceptional discriminant function based on the received radar phase. PSF is using another method to estimate the phase fluctuations without using the polynomial fitting function, which can make it more efficient, in terms of the computational complexity. The PSF is jointly combined with ρ_{12} to form a unique 3D discriminant function with outstanding performance improvements for the probability density function. It is shown that the 3D discriminant function has a good separation in 3D visualization, and the highest probability of detection is achieved compared to other detection algorithms. The class conditional densities need to be parametrized because the clutter and weather PDFs may change and may need to be updated based on the weather, clutter, radar parameters, and antenna rotation. Also, the complete knowledge about the probabilistic structure of the class conditional densities may not be available for the real-time implementations. It is more efficient to update the PDF using a limited number of variables (i.e. mean, variance), instead of recalculating the PDF from the data. Therefore, a multivariate Gaussian mixture model is introduced to parameterize the PDFs of discriminant functions. The parameters are obtained and updated based on the maximum likelihood method using the Expectation-Maximization (ML-EM) algorithm. The performance of the proposed algorithm is compared to several existing detection algorithms. The comparison results revealed that our proposed algorithm could effectively improve the performance of clutter detection algorithms to achieve the highest probability of detection.

5.1 Phase Structure-Function

In this section, the phase structure function is presented as a novel discriminant function to improve detection algorithms. The wave scattering from the randomly distributed hydrometers produces the fast phase fluctuations due to the random size

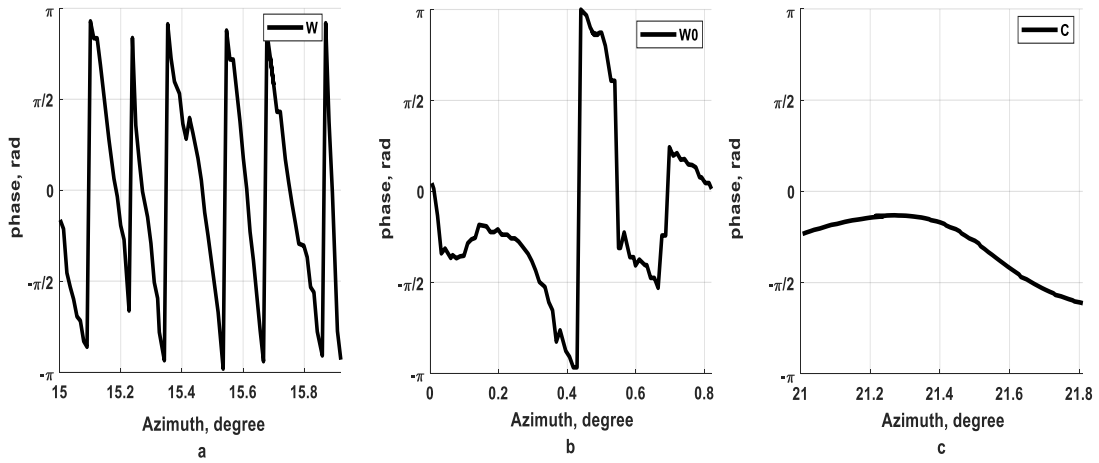

Figure 5-1: Phase of the I/Q data for a) Non-zero velocity weather, b) Zero velocity weather, c) Clutter

and location of scatterers and turbulence with radial velocity (see Figure 5-1a, b). However, the wave scattering from fixed scatterers on the ground (or ground clutter) produces a slow fluctuation in the phase of received signals (see Figure 5-1c). Therefore, the phase structure function is introduced to distinguish clutter from weather signals. The PSF is using a direct method to estimate the phase fluctuations without calculating the polynomial fitting function, which make it operationally efficient, in terms of the computational complexity. The PSF for H- and V- polarizations is defined as:

$$PSF_{\mathrm{h}} = \frac{1}{M}\sum_{n=1}^{M-1}\left|\phi_{\mathrm{h}}(n+1)-\phi_{\mathrm{h}}(n)\right|^2$$
$$PSF_{\mathrm{v}} = \frac{1}{M}\sum_{n=1}^{M-1}\left|\phi_{\mathrm{v}}(n+1)-\phi_{\mathrm{v}}(n)\right|^2 \tag{5.1}$$

The phase structure-function is obtained from the average of angular separations between consecutive phases, for each resolution volume.

Figure 5-2–Figure 5-4 shows the joint 2D PDF of the PSF algorithm for clutter and weather classes. Parzen windows have been applied to estimate the joint class-conditional densities for each class from the training datasets (i.e., p(PSF_{h}, PSF_{v} |C), p(PSF_{h}, PSF_{v} |W), p(PSF_{h}, PSF_{v} |W_0)) [53]. It can be seen that the clutter PDF has near-zero values, and weather PDFs have large values with the PSF peaks around 7 rad^2. Moreover, there is a good separation between clutter and weather PDFs, and thus, this discriminant function can improve the probability of detection for clutter detection algorithms. In the next section, we show that the PSF as a discriminant function can improve the probability of detection compared to other existing algorithms.

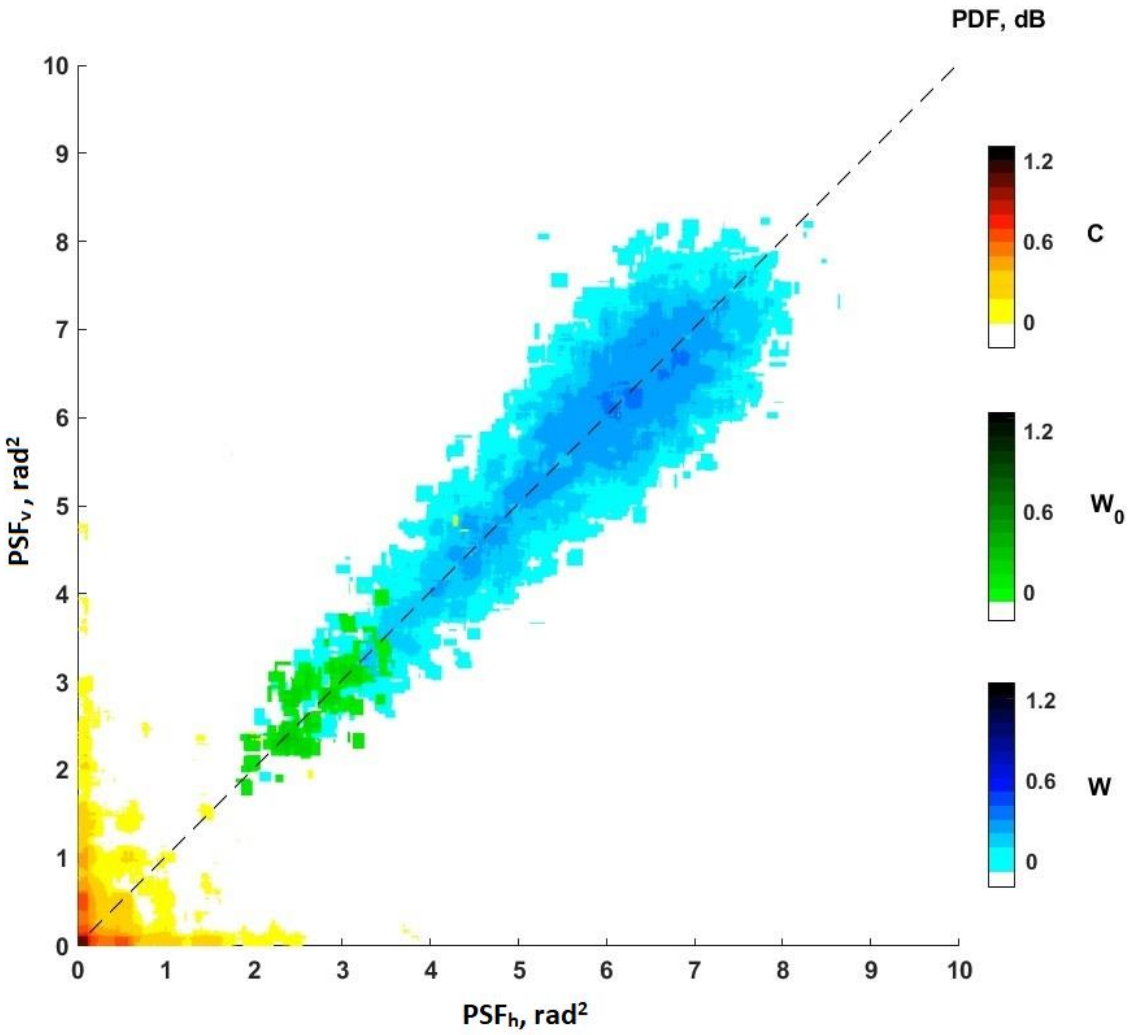

Figure 5-2: Joint 2D PDF of [PSFh, PSFv], rad²

Figure 5-3 and Figure 5-4 show the joint 2D class conditional densities based on [ρ_{12} , min(PSFh, PSFv)] and [ρ_{12} , PSFh]. There is a tendency for PSFh and PSFv, to take on values very close to zero. Therefore, it is more efficient to use min(PSFh, PSFv) with ρ_{12} , for the joint 2D discriminant function, instead of using PSF_h with ρ_{12} . As can be seen from Figure 5-3, the joint 2D PDF based on min(PSFh, PSFv) can concentrate the C class data nearer the origin while preserving the separation with W_0 and W classes. In the next section, the probability of detection for our proposed

PSF clutter detection algorithm is presented and compared to other detection algorithms.

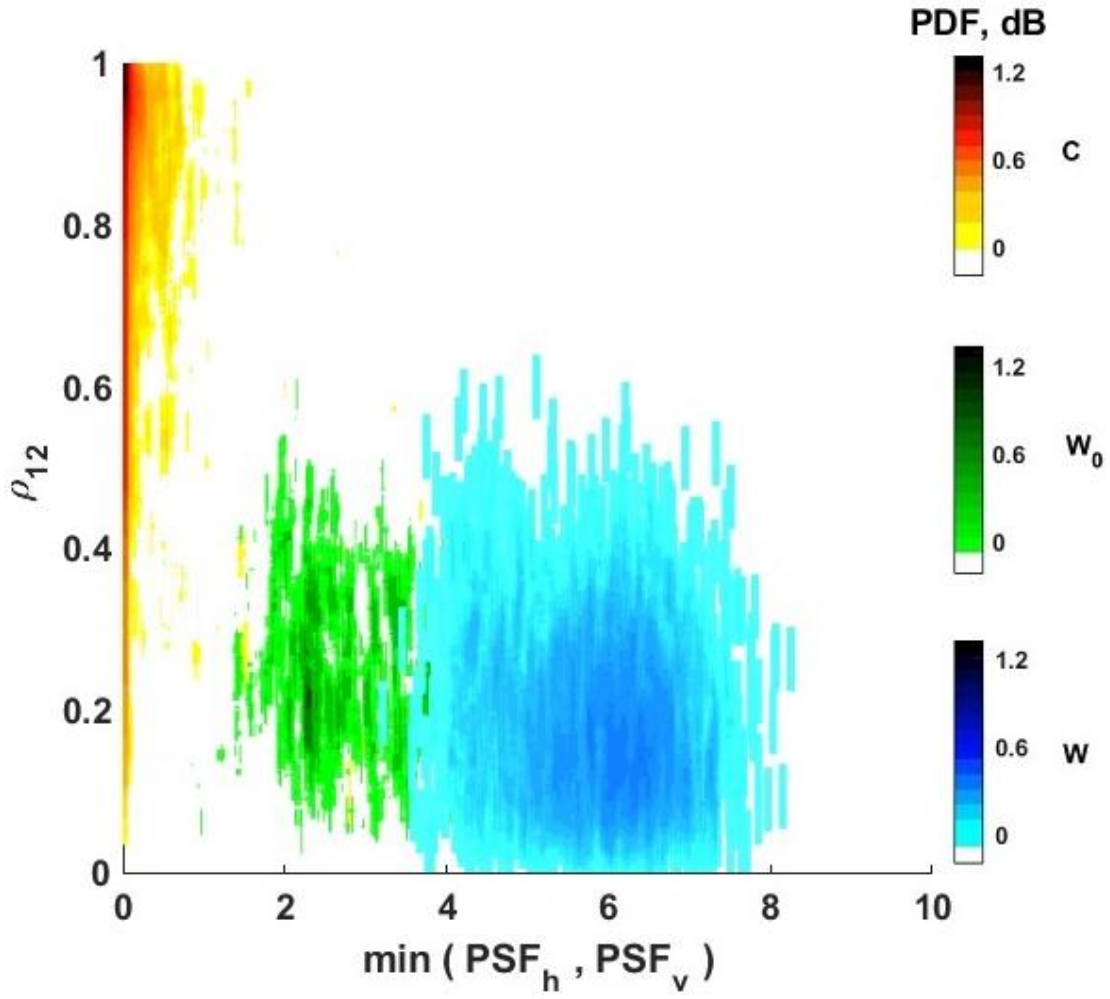

Figure 5-3: Joint 2D class-conditional densities for $p\left(\rho_{12}, \min(PSF_h, PSF_v) \mid \omega_i\right)$

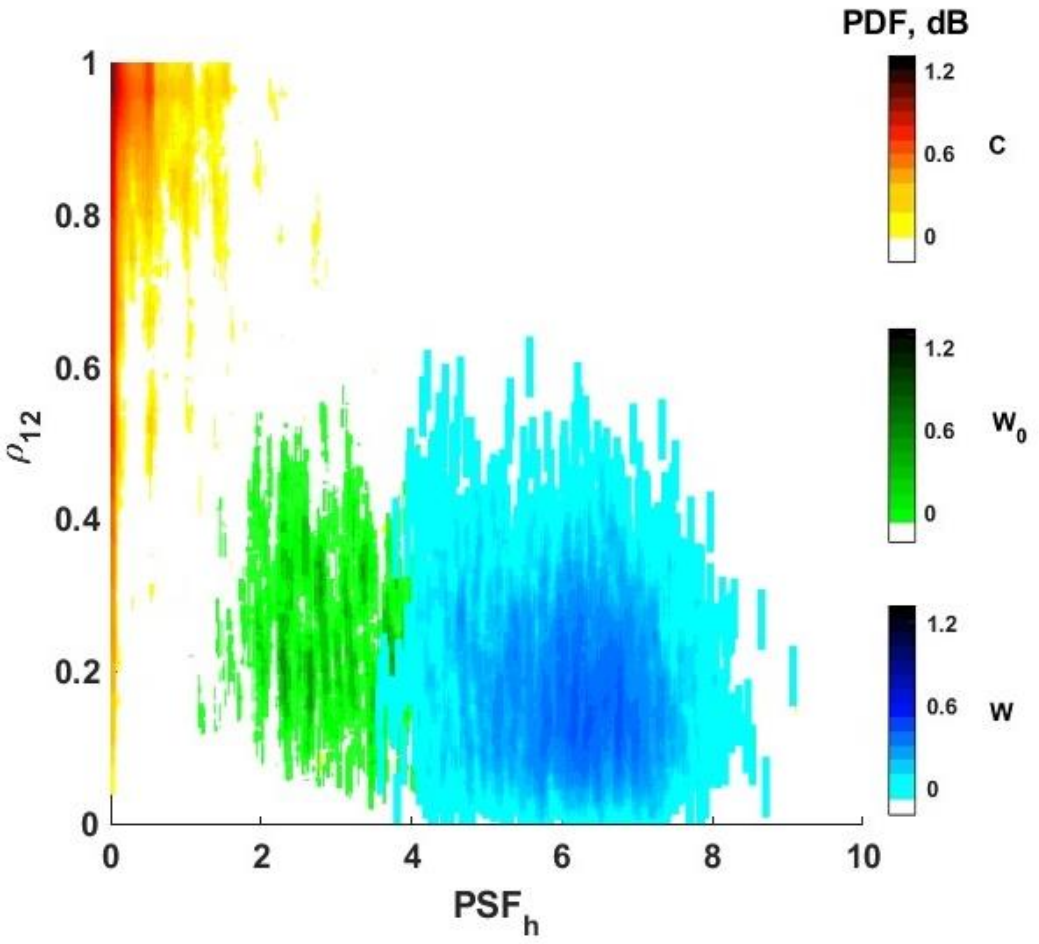

Figure 5-4: Joint 2D class-conditional densities for $p\left(\rho_{12}, PSF_h \mid \omega_i\right)$

5.2 Gaussian Mixture Model (GMM) parametrization

The PDFs of discriminant functions may change based on types of weather and clutter, and the radar parameters, and thus, the class conditional densities may need to be updated [54, 55]. A multivariate Gaussian mixture model (GMM) is designed for clutter detection discriminant functions to parametrize the PDFs. The PDF parameters are estimated based on the maximum likelihood, using the Expectation-Maximization (ML-EM) algorithm [53, 54].

5.2.1 Joint 2D GMM model

Figure 5-5 shows the GMM model for the 2D joint class-conditional densities (i.e. [PSF_H, PSF_V] for all classes. The PDF of the clutter has the peak values near zero for PSF and near one for ρ_{12}. Therefore, the GMM model for clutter PDFs has been modified by using a mirror function before applying the Gaussian fitting function to the clutter PDF. In Figure 5-5, the GMM model is estimated for the 2D lognormal distribution function (shown in Figure 5-2), and the GMM statistical parameters are estimated based on the ML-EM method and presented in Table 5.1. The joint 2-dimensional (2D) PDF of a vector [X Y] for the Bi-variate Gaussian distribution is calculated as [53, 54] [40]:

$$p(X,Y) = \frac{1}{2\pi\sigma_X\sigma_Y\sqrt{1-\rho_{XY}^2}} \times \exp\left\{-\frac{1}{2\left(1-\rho_{XY}^2\right)}\left[\frac{(X-\mu_X)^2}{{\sigma_X}^2} + \frac{(Y-\mu_Y)^2}{{\sigma_Y}^2} - \frac{2\rho_{XY}(X-\mu_X)(Y-\mu_Y)}{\sigma_X\sigma_Y}\right]\right\}$$

$$\mu \triangleq \begin{pmatrix}\mu_X \\ \mu_Y\end{pmatrix}, \text{ and } \sum \triangleq \begin{pmatrix}{\sigma_X}^2 & \sigma_X\sigma_Y\rho_{XY} \\ \sigma_X\sigma_Y\rho_{XY} & {\sigma_Y}^2\end{pmatrix} \tag{5.2}$$

where μ, *and* $\sum$ represent the mean and covariance matrixes and ρ_{XY} is the cross-correlation between X and Y. In Figure 5-5, [X Y] vector is considered as [PSF_h, PSF_v].

Table 5.1: Fitted conditional probability function parameters for 2D GMM

Variables	**Classes**	PSF_h	PSF_v
μ	C	0.1151	0.1151
	W	6.4778	6.4286
	W_0	2.6999	2.6242
Σ	C	0.4973	0.0003
		0.0003	0.8807
	W	0.5744	0.3126
		0.3126	0.5816
	W_0	0.3615	0.2940
		0.2940	0.3359

The mean and standard deviation of the joint 2D GMM model are presented in Table 5.1. The standard deviation generally indicates how largely data points tend to be spread around the mean value. As can be seen from Table 5.1, the mean value for the "C" class is 0.1151 for both PSF_h and PSF_V, and the mean value for W is around 6.4 rad^2 and for W_0 is around 2.6 rad^2. The results in this table clearly indicated that the clutter has a good separation from weather classes in terms of the joint PDF of PSF as a discriminant function. There are several advantages to this GMM model: [40]:

1) it can be efficiently updated for different conditions;

2) the parameters can be estimated by a small amount of training data;

3) If the *priori* distributions are not equal for all classes, the Maximum-*a-Posteriori* (MAP) parameter estimator can be used instead of *ML*;

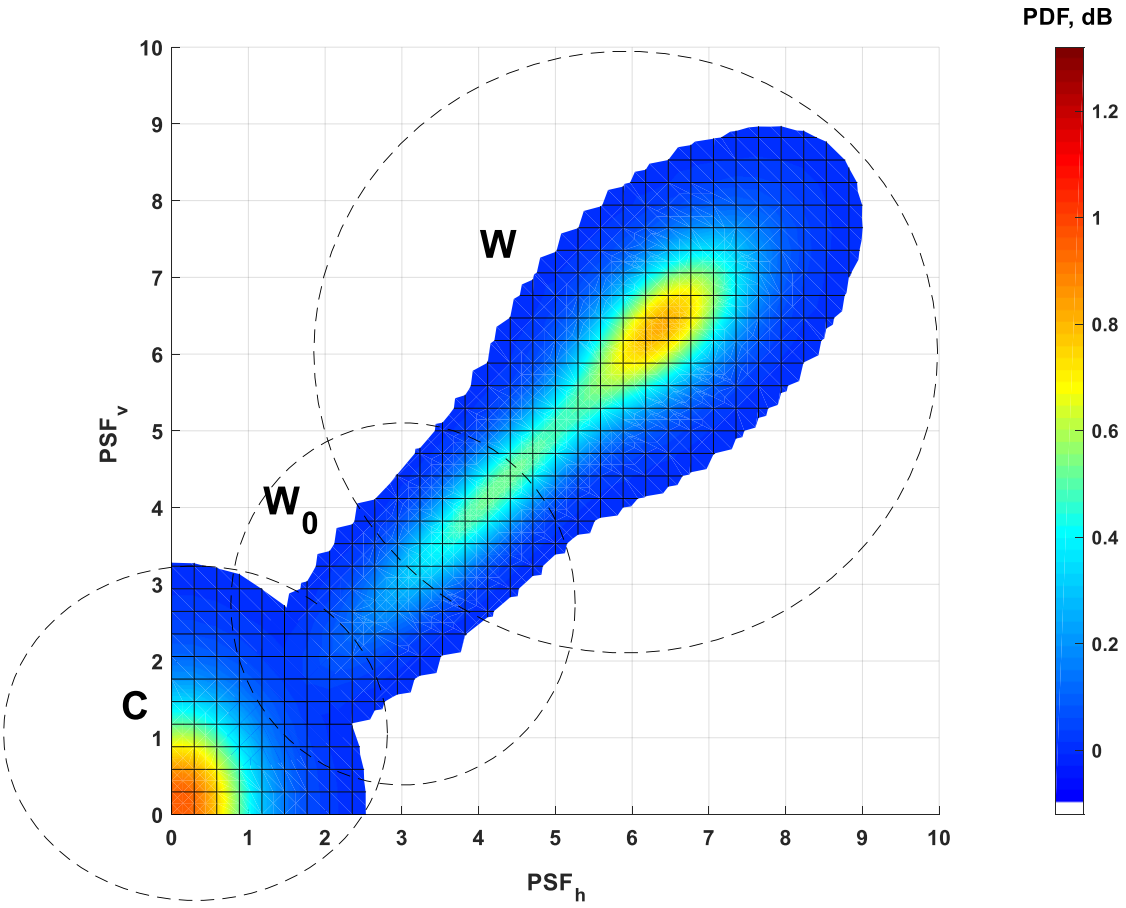

Figure 5-5: 2D joint class-conditional densities for each class of GMM (i.e. p (*PSF*$_h$, *PSF*$_v$ |C), p(*PSF*$_h$, *PSF*$_v$ |W), p (*PSF*$_h$, *PSF*$_v$ |W$_0$))

5.2.2 Joint 3D GMM Model

The ML-EM method is used to estimate the GMM model parameters for the joint 3D PDF of [PSFh, PSFv, ρ_{12}].

The PDF of the joint 3D Gaussian distribution can be calculated as [53, 54] [40]:

$$p(Z)=\frac{1}{\sqrt{(2\pi)^3|\Sigma|}}\exp\left\{-\frac{1}{2}(Z-\mu_Z)'\,\Sigma^{-1}(Z-\mu_Z)\right\} \qquad (5.3)$$

$$\mu \triangleq \begin{pmatrix} \mu_{Z_1} \\ \mu_{Z_2} \\ \mu_{Z_3} \end{pmatrix}, \text{ and } \sum \triangleq \begin{pmatrix} \sigma_{Z_1}{}^2 & \sigma_{Z_1}\sigma_{Z_2}\rho_{Z_1Z_2} & \sigma_{Z_1}\sigma_{Z_3}\rho_{Z_1Z_3} \\ \sigma_{Z_1}\sigma_{Z_2}\rho_{Z_1Z_2} & \sigma_{Z_2}{}^2 & \sigma_{Z_2}\sigma_{Z_3}\rho_{Z_2Z_3} \\ \sigma_{Z_1}\sigma_{Z_3}\rho_{Z_1Z_3} & \sigma_{Z_2}\sigma_{Z_3}\rho_{Z_2Z_3} & \sigma_{Z_3}{}^2 \end{pmatrix}$$

where $Z = [Z_1, Z_2, Z_3]^T = [PSF_h, PSF_v, \rho_{12}]^T$. The GMM model of the joint 3D PDF is shown in Figure 5-6. The weather signals have larger *PSF* for H and V polarizations with smaller ρ_{12}. As we discussed in chapter 2, ρ_{12} has a better separation between clutter and weather pdfs compared to other discriminant functions, thus. we used it here as the third discriminant function for the joint 3D PDF. Moreover, the clutter has smaller values of *PSF* with a wider range and larger values of ρ_{12}. Consequently, it is shown that the joint 3D PDF of clutter and weather signals are separated in terms of the 3D discriminant function.

Table 5.2: Fitted conditional probability function parameters for 3D GMM

Variables	**Classes**	ρ_{12}	PSF_h	PSF_v
μ	C	0.9815	0.1500	0.1500
	W	0.1867	6.4744	6.4420
	W_0	0.2981	2.6460	2.5763
Σ	C	0.1872	0.0001	0.0010
		0.0001	1.1592	0.0003
		0.0010	0.0003	1.5172
	W	0.0080	-0.0008	0.0009
		-0.0008	0.4414	0.2917
		0.0009	0.2917	0.4579
	W_0	0.0139	0.0017	-0.0010
		0.0017	0.2062	0.1592
		-0.0010	0.1592	0.1730

Other visualizations of the class conditional densities are shown in Figure 5-8 - Figure 5-10. Therefore, the PSF detection algorithm based on the 3D-PDF can efficiently reduce the error rate and improve the probability of detection compared to other detection algorithms.[40, 41] Also, it can be seen from Figure 5-5 and Figure 5-8, that the joint 2D-PDFs have an overlapped areas between clutter and weather PDFs and thus, it is normally expected that the error rate for the PSF algorithm based on the joint 2D-PDF is more than that for the 3D-PDF.

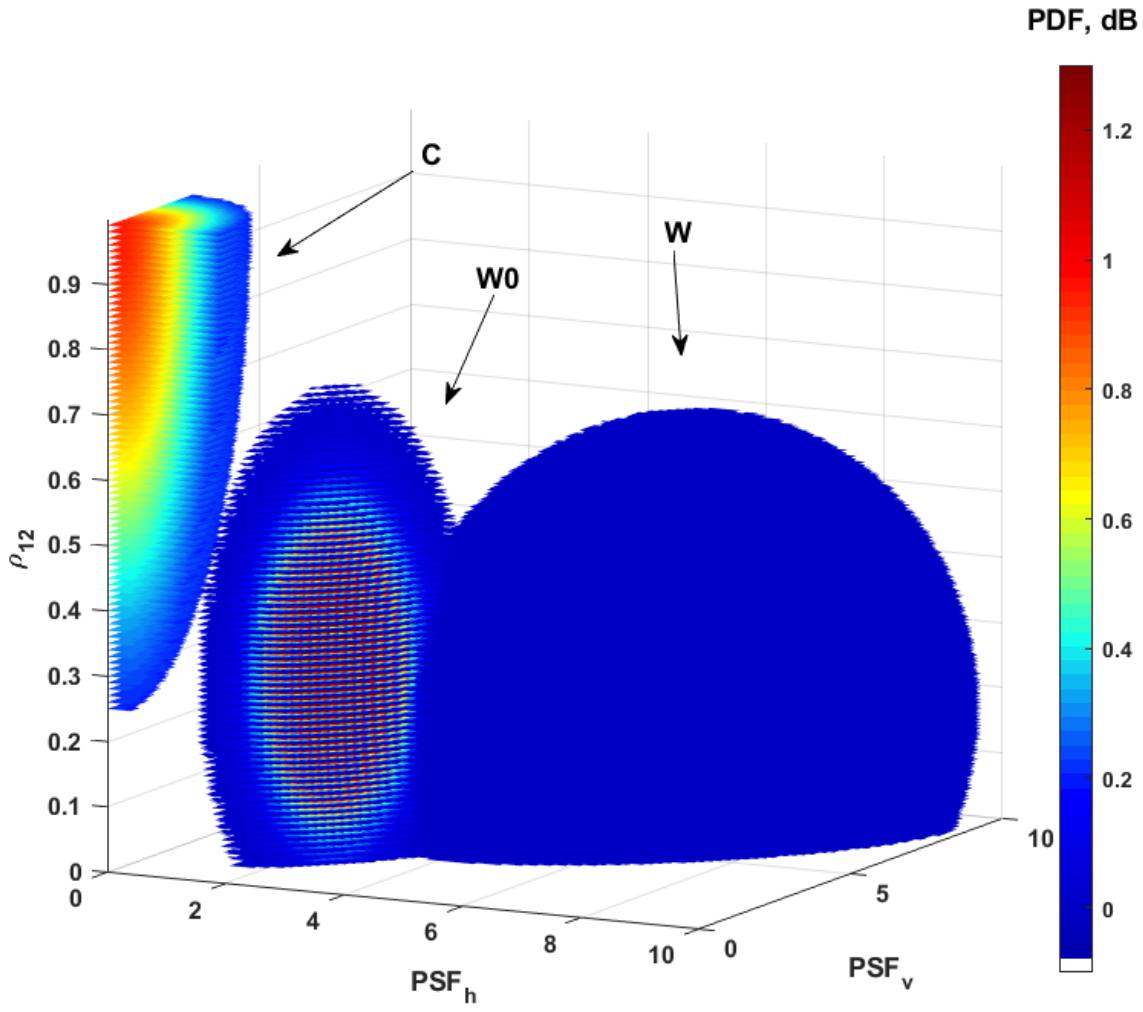

Figure 5-6: 3D PDF of [PSFh, PSFv, ρ_{12}] for the GMM (i.e. p(PSFh, PSFv, ρ_{12} |C), p(PSFh, PSFv, ρ_{12} |W), p(PSFh, PSFv, ρ_{12} |W0))

As can be seen from Figure 5-5 and Figure 5-8, the joint 2D PDFs have the overlapped areas between the clutter and weather PDFs, and thus, it is normally expected that the error rate for the 2D-PSF clutter detection algorithm is more than that for 3D-PDF. The probability of detection for our proposed PSF-3D clutter detection algorithm is presented in the next section and compared to other existing detection algorithms.

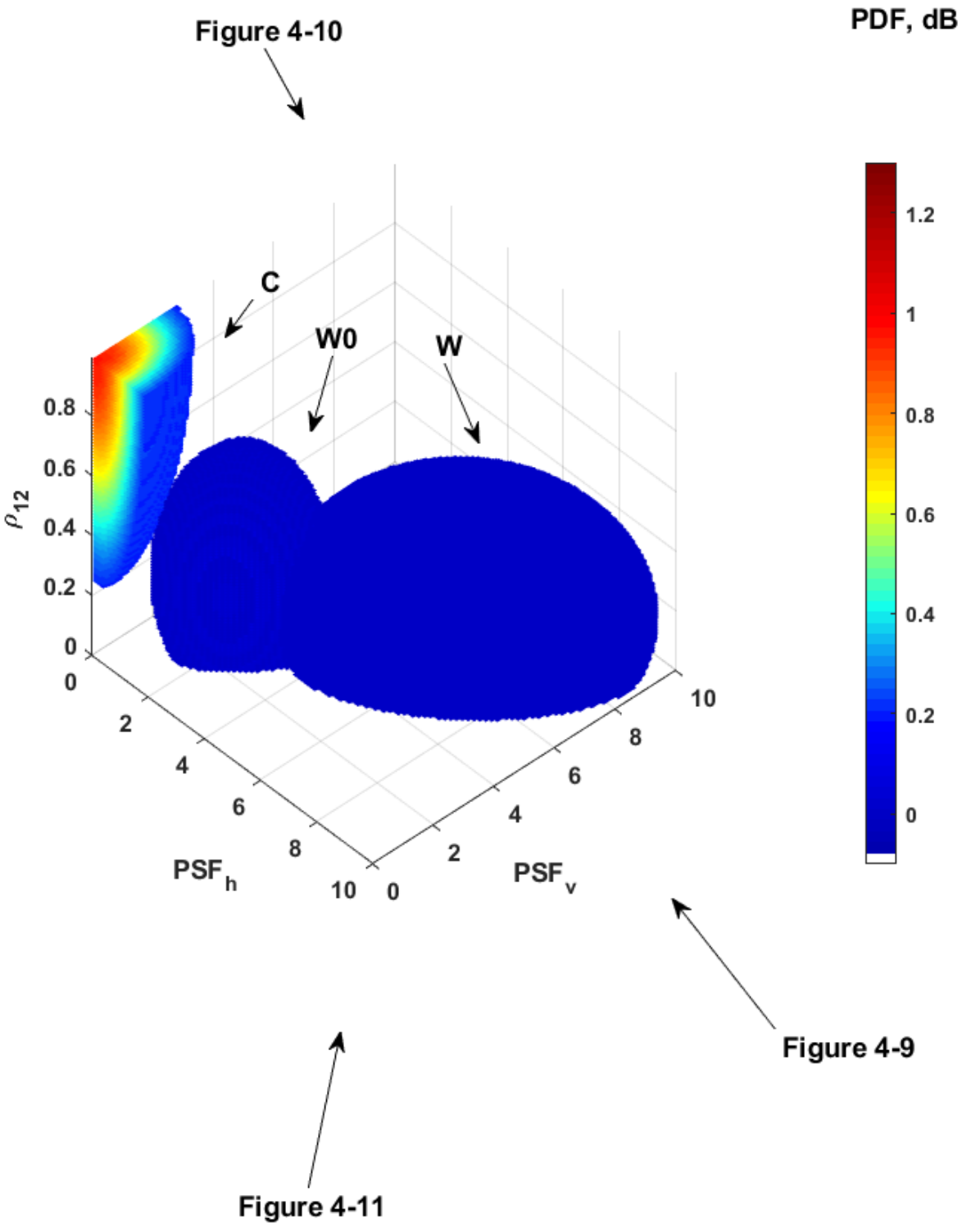

Figure 5-7: Other visualizations of joint 3D PDF for GMM

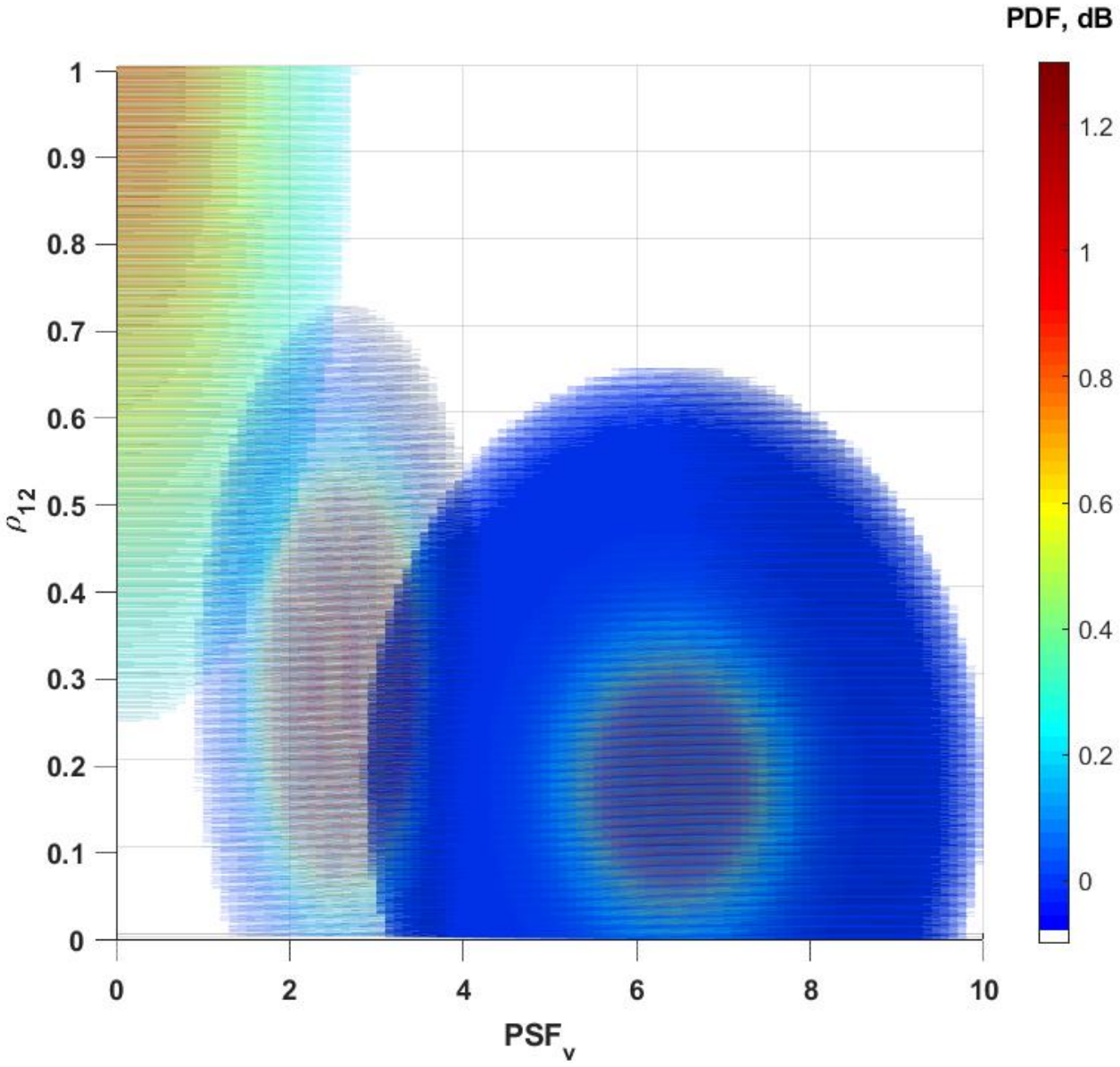

Figure 5-8: 2D-visualization of the joint 3D PDF on [PSF_h, ρ_{12}] for the GMM

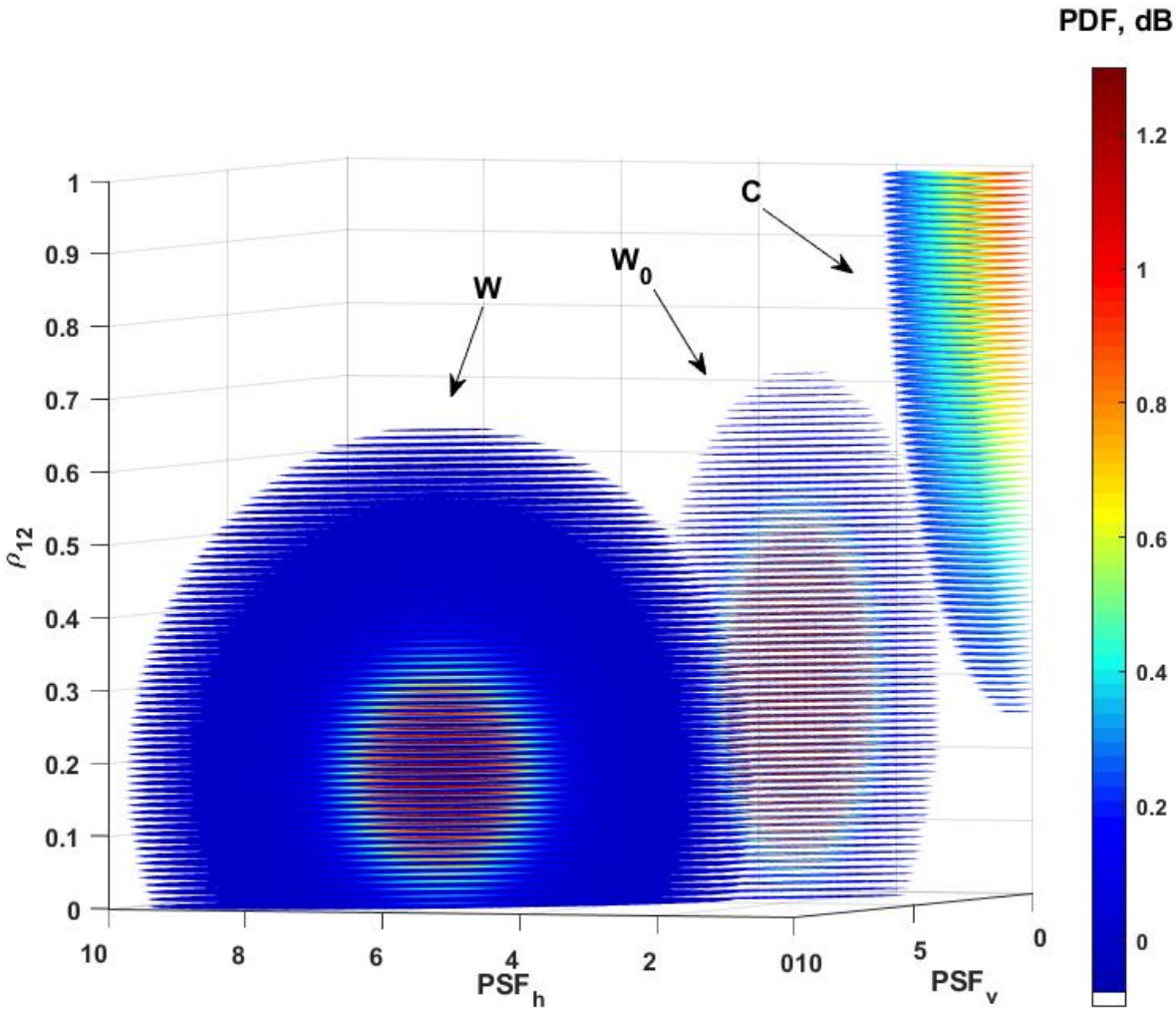

Figure 5-9: Other visualizations of joint 3D PDF for GMM

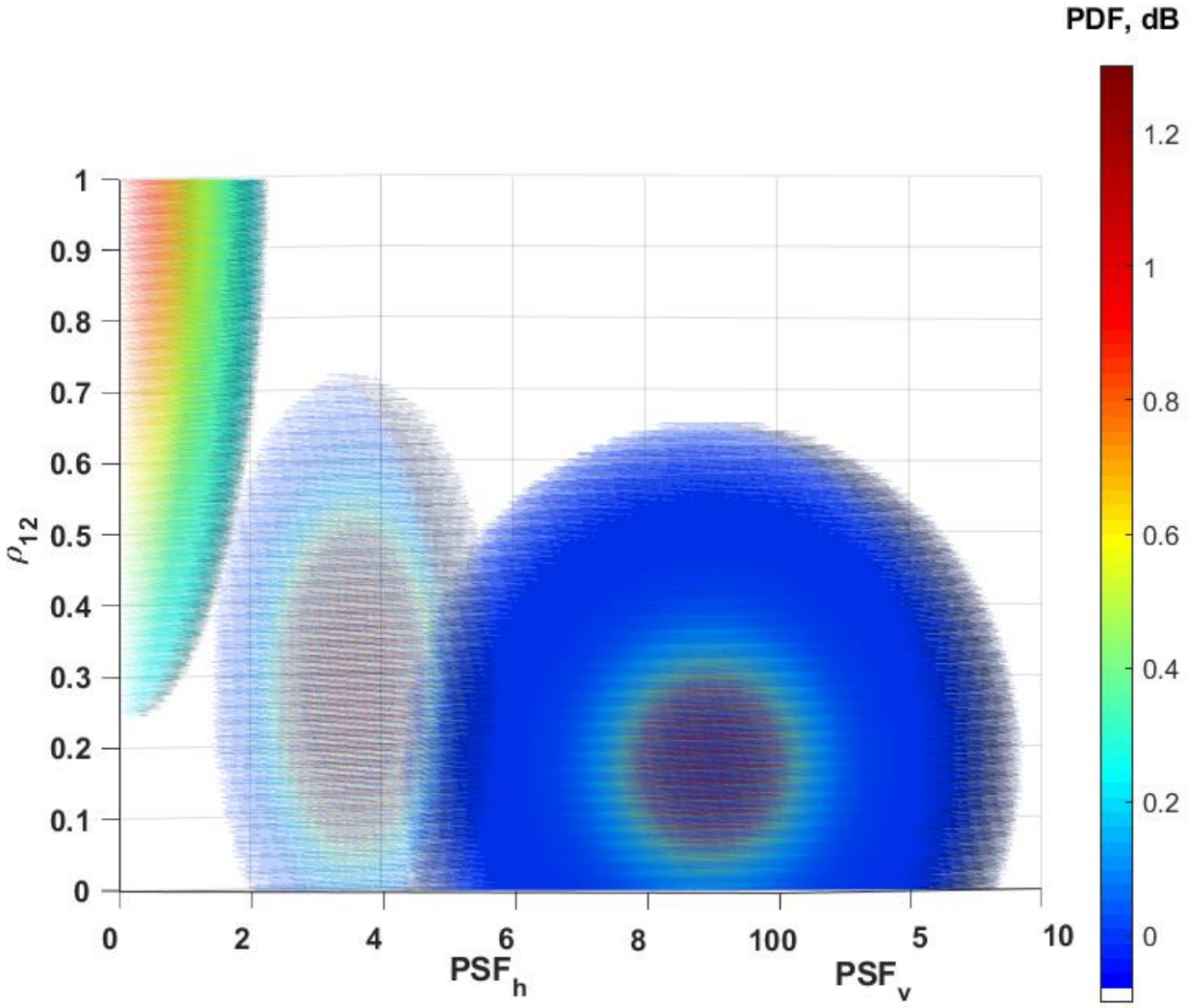

Figure 5-10: Other visualizations of joint 3D PDF for GMM

5.3 Optimal Decision for the GMM model

In the previous section, the joint 3D PDF has been calculated from training data and can be used as a reference for the optimal Bayesian classifier. For each resolution volume, the observational discriminant vector $\boldsymbol{X}° = (PSF_h°, PSF_v°, \rho_{12}°)$ needs to be calculated. The optimal classifier detects $\boldsymbol{X} = \boldsymbol{X}°$ belongs to the class ω_i, if and only

if its joint 3D PDF for ω_i is more than that for other classes, i.e., $p(\omega_i|\boldsymbol{X}^\circ) > p(\omega_j|\boldsymbol{X}^\circ)$ and $p(\omega_i|\boldsymbol{X}^\circ) > p(\omega_k|\boldsymbol{X}^\circ)$ for $i, j, k \in [\mathrm{C}, \mathrm{W}, \mathrm{W0}]$, $i \neq j, k$.

The likelihood function is obtained from training data for each class from the joint 3D PDF (shown in Figure 5-6). Thus, we have:

$$p(\boldsymbol{X} = \boldsymbol{X}^{\mathrm{O}} \mid \omega_i) = p\left(PSF_h^{\mathrm{O}}, PSF_v^{\mathrm{O}}, \rho_{12}^{\mathrm{O}} \mid \omega_i\right) \tag{5.4}$$

Therefore, the likelihood function ($p(\boldsymbol{X} = \boldsymbol{X}^{\mathrm{O}} \mid \omega_i)$) is calculated for each class, and the class corresponding to the maximum probability value will be selected as the classification decision. Thus, we can infer that the Bayesian classifier assigns $\boldsymbol{X} = \boldsymbol{X}^\circ$ to "C" only if

$$p\left(PSF_h^{\mathrm{O}}, PSF_v^{\mathrm{O}}, \rho_{12}^{\mathrm{O}} \mid \mathrm{C}\right) > p\left(PSF_h^{\mathrm{O}}, PSF_v^{\mathrm{O}}, \rho_{12}^{\mathrm{O}} \mid \mathrm{W}\right)$$

, and (5.5)

$$p\left(PSF_h^{\mathrm{O}}, PSF_v^{\mathrm{O}}, \rho_{12}^{\mathrm{O}} \mid \mathrm{C}\right) > p\left(PSF_h^{\mathrm{O}}, PSF_v^{\mathrm{O}}, \rho_{12}^{\mathrm{O}} \mid \mathrm{W}_0\right)$$

The clutter detection algorithm is summarized as:

1. Estimate the GMM parameters and update the GMM model based on the estimated parameters, and calibrate the PDFs shown in Figure 5-6.
2. Calculate SNR for the current resolution volume.

   If the SNR is more than 20dB, go to step 3. Otherwise, the current gate is considered not to have a significant signal compared to the noise power, and we calculate SNR for the next resolution volume.

3. Calculate the 3D observed discriminant function for the current gate, using the joint 3D PDF obtained in step 2:

$$p(\boldsymbol{X} = \boldsymbol{X}^{\mathrm{O}} \mid C) = p\left(PSF_h^{\mathrm{O}}, PSF_{\mathrm{v}}^{\mathrm{O}}, \rho_{12}^{\mathrm{O}} \mid C\right),$$

$$p(\boldsymbol{X} = \boldsymbol{X}^{\mathrm{O}} \mid W_0) = p\left(PSF_h^{\mathrm{O}}, PSF_{\mathrm{v}}^{\mathrm{O}}, \rho_{12}^{\mathrm{O}} \mid W_0\right),$$

$$p(\boldsymbol{X} = \boldsymbol{X}^{\mathrm{O}} \mid W) = p\left(PSF_h^{\mathrm{O}}, PSF_{\mathrm{v}}^{\mathrm{O}}, \rho_{12}^{\mathrm{O}} \mid W\right).$$

4. The data for the current gate is clutter-contaminated if

$$p(\boldsymbol{X} = \boldsymbol{X}^{\mathrm{O}} \mid C) > p(\boldsymbol{X} = \boldsymbol{X}^{\mathrm{O}} \mid W)$$

$$p(\boldsymbol{X} = \boldsymbol{X}^{\mathrm{O}} \mid C) > p(\boldsymbol{X} = \boldsymbol{X}^{\mathrm{O}} \mid W0).$$

Thus, a ground clutter filter [40, 56] needs to be applied to mitigate clutter effects and restore weather estimates. Otherwise, the data is not contaminated and return to step 1 for the next gate.

The performance of the clutter detection algorithm is evaluated using the testing datasets collected by the KOUN (WSR-88D) radar at 14:02 UTC on 9 February 2011, and 00:47 UTC on 4 February 2011. Ground truth has been obtained from the combination of pure clutter and pure weather data and will be used as a reference to obtain the CSR. The proposed 3d-PSF clutter detection algorithm is compared to other clutter detection algorithms, such as DPDS, DP, DS, CMD, presented in [10, 18-20].

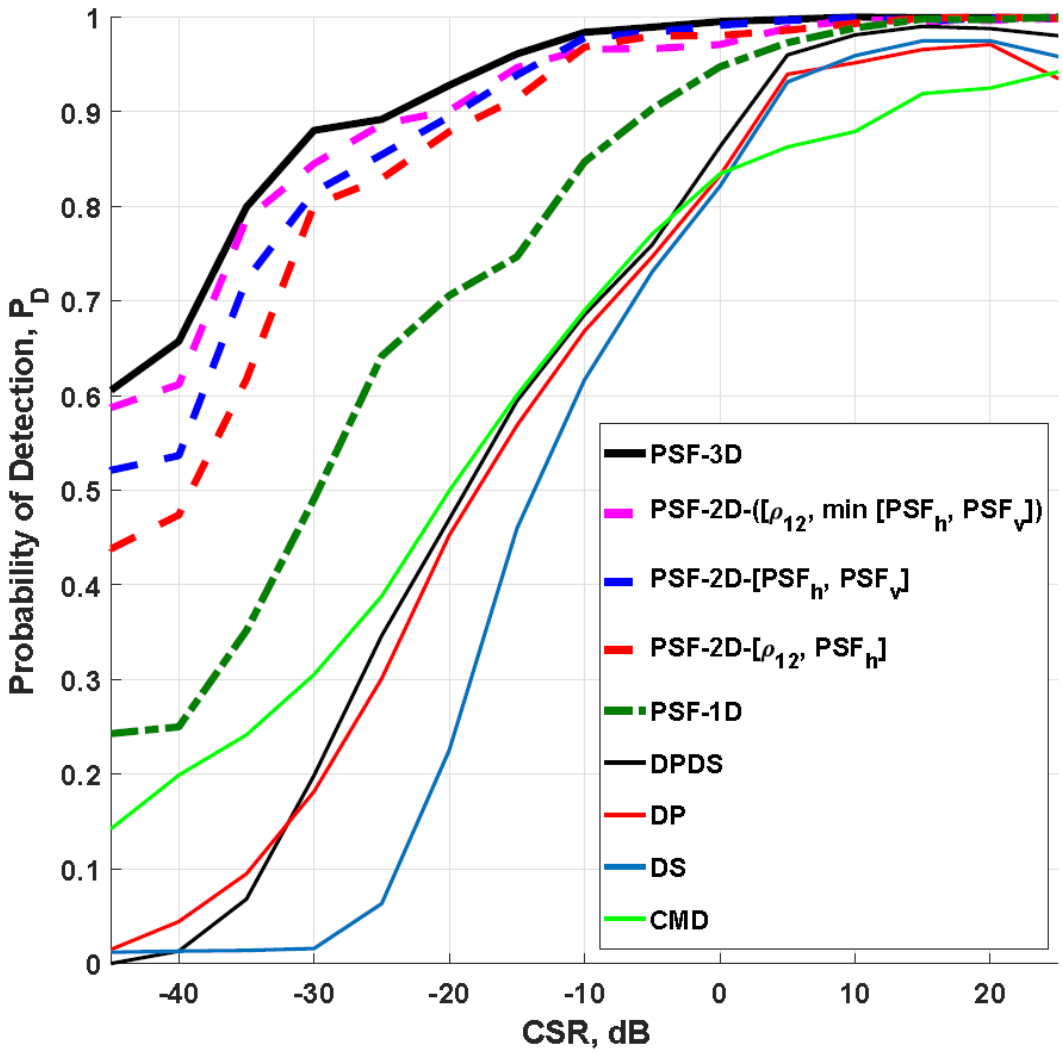

Figure 5-11: Probability of Detection (P_D) using PSF-3D vs. Clutter to Signal Ratio, compared to other detection methods.

Figure 5-11 shows the probability of detection for different clutter detection algorithms. As can be seen from this figure, there is a significant improvement in P_D, using the proposed 3D-PSF clutter detection algorithm compared to other detection algorithms. The performance improvements for the proposed algorithm are due to the good separation of class conditional densities in the 3D space (see Figure 5-2-Figure 5-6).

Figure 5-12 shows the proposed PSF clutter detection algorithm compared to the PSF based on the 2D PDFs, and 3-1D PDF (dash-lines). The 2D-PDFs have over-lapped areas between clutter and weather PDFs and therefore, the probability of detection for the PSF algorithms based on the joint 2D-PDFs are less than that of the 3D-PDF. The PSF algorithm based on the joint 2D PDF of [min (PSF_h, PSF_v), ρ_{12}] has the best performance in compared to other PSF-2D algorithms, and the PSF algorithm based on the joint 2D-PDF of [(PSF_h, PSF_v)] can be used for the case that dual-scan data or ρ_{12} is not available for the radar system. Also, the results are compared to the case of 3-1D (non-joint) discriminant functions, in which the PDFs are separately calculated and considered to make a decision based on the Bayesian classifier.

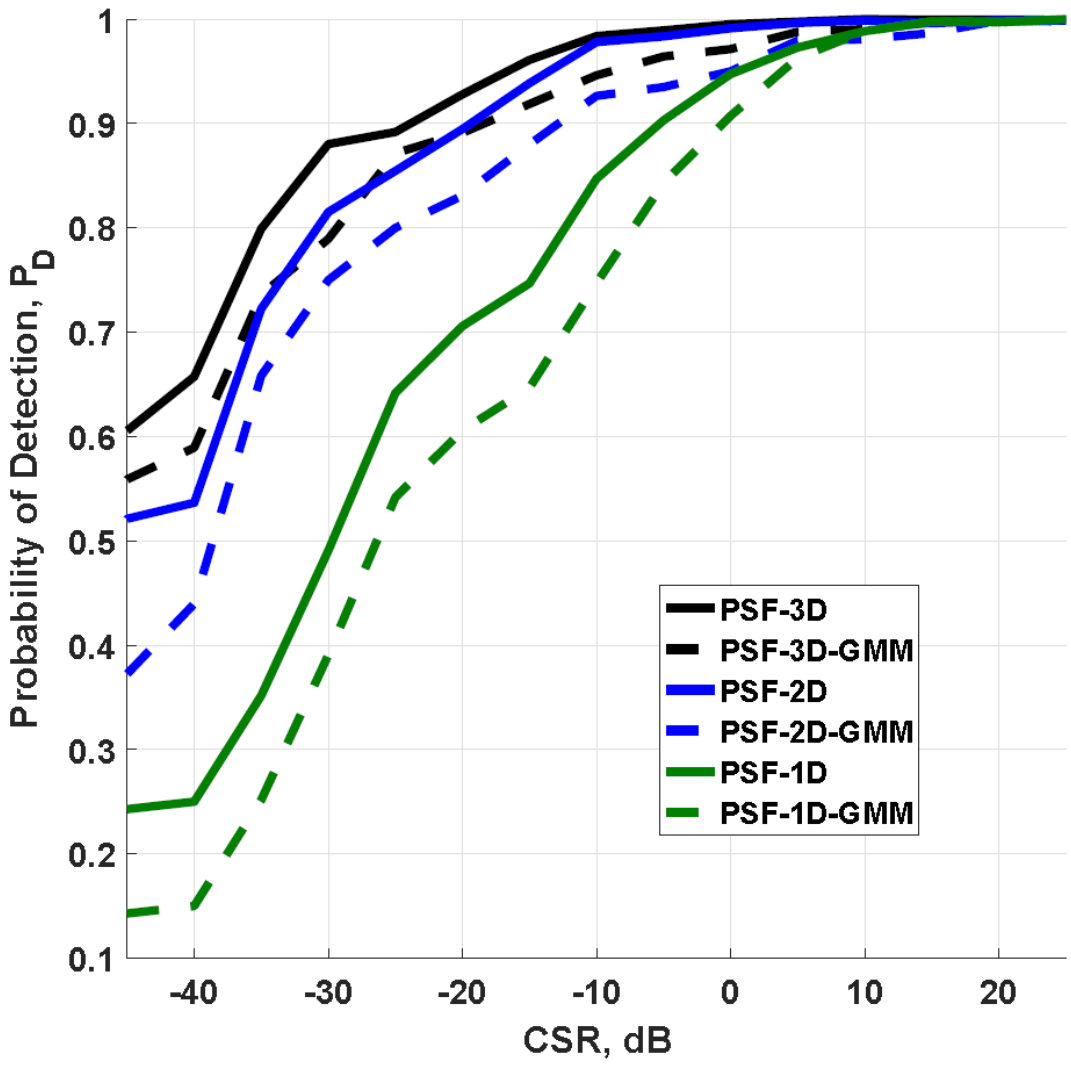

Figure 5-12: Probability of Detection using PSF-3D vs. CSR, compared to GMM methods.

Table 5.3: P_{FA} for the testing data set by using the proposed PSF algorithm compared to DPDS, DP, DS, and CMD algorithms.

	3D-PSF	3D-PSF GMM	2D-PSF GMM	1D-PSF GMM	DPDS	DP	DS	CMD
P_{FA}	0.09%	0.14%	0.14%	0.17%	0.21%	0.47%	0.39%	0.53%

Figure 5-13 shows the P_D for the 3D-PSF detection algorithms with 3D discriminant function (i.e. [PSF_h, PSF_v, ρ_{12}]) and compared to 2D discriminant function (i.e. [PSF_h, PSF_v]), and 3-1D discriminant functions (i.e. [PSF_h], [PSF_v], [ρ_{12}]). The 2D-PSF discriminant function has an overlapped area between clutter and weather PDFs, and therefore the probability of detection is less than the PSF based on the 3D discriminant function. Also, the results are compared to the case of 3-1D (non-joint) discriminant functions, in which the PDFs of discriminant functions are separately calculated and considered to make a decision based on the Bayesian classifier. As can be seen from Figure 5-13, the probability of clutter detection based on the 3D discriminant function has an outstanding performance because there is a good separation between the clutter and weather PDFs, as shown in Figure 5-6. In Figure 5-13, the proposed detection algorithm is also compared to the PSF-GMM model ("dash-lines"). It should be noted that the computational complexity of the model is reduced by parametrizing the discriminant functions, and it is shown that the PSF_GMM algorithm has better performance compared to other existing detection algorithms, such as DP-DS, DP, DS, CMD [10, 18-20]. Moreover, the PSF-1D or PSF-2D detection algorithms still have better performance gains compared to DPDS, DP, DS, and CMD algorithms, in the case, the dual polarization and dual-scan datasets are not available for the weather radar.

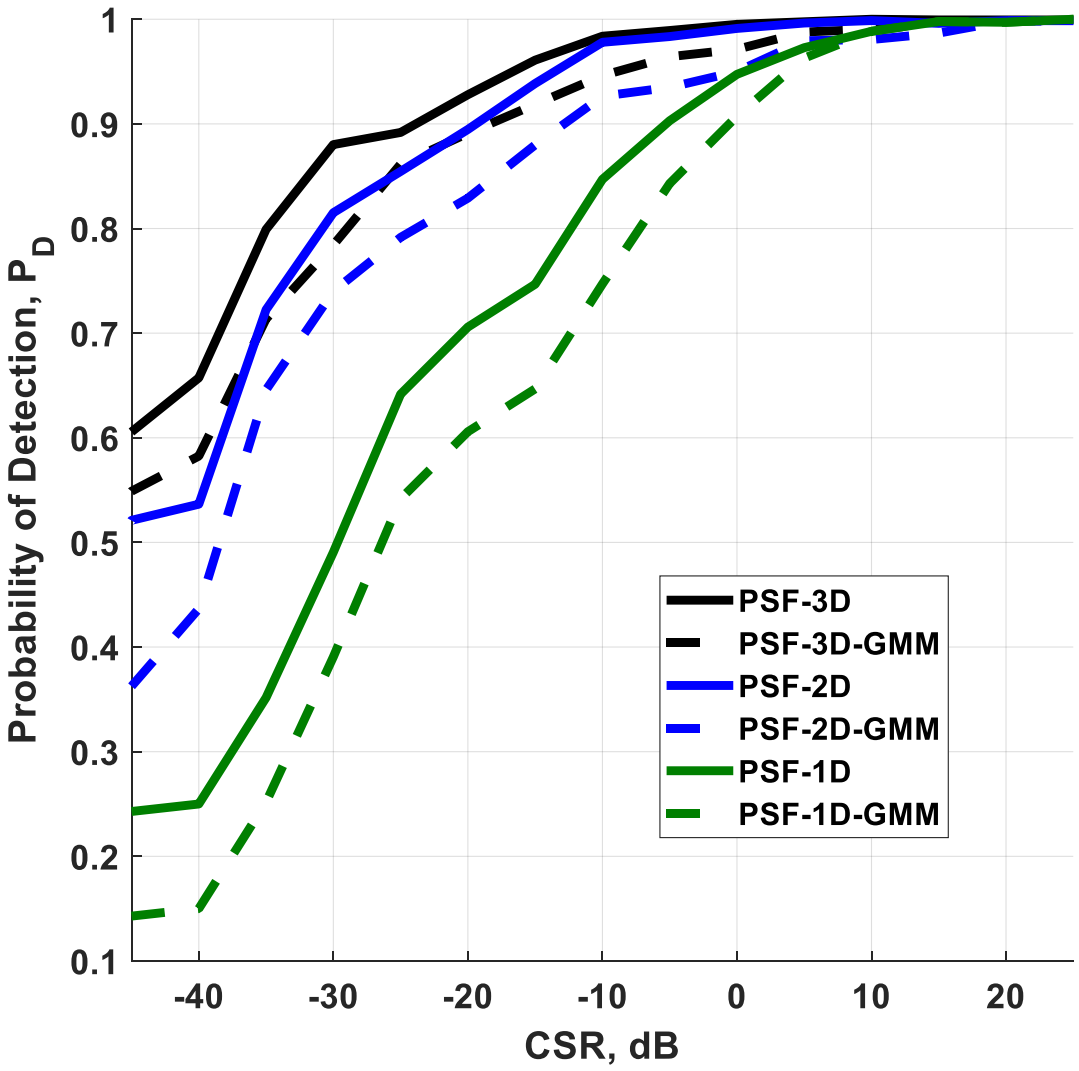

Figure 5-13: Probability of Detection (P_D) for different detection algorithms based on the PSF

Figure 5-14 shows the clutter maps for the proposed PSF algorithm and compared it to other clutter detection algorithms. The results of the PSF-3D algorithm are most similar to the ground truth in comparison to other detection algorithms. In this figure, blue points show True Positive samples and represent the number of clutter samples (as shown in the ground truth), which are correctly detected by

the algorithm. Yellow points (False Negative) are the samples that are falsely detected as weather instead of clutter by the detection algorithm, and green points (False Positive) are the samples that are falsely detected as clutter instead of weather, by the algorithm.

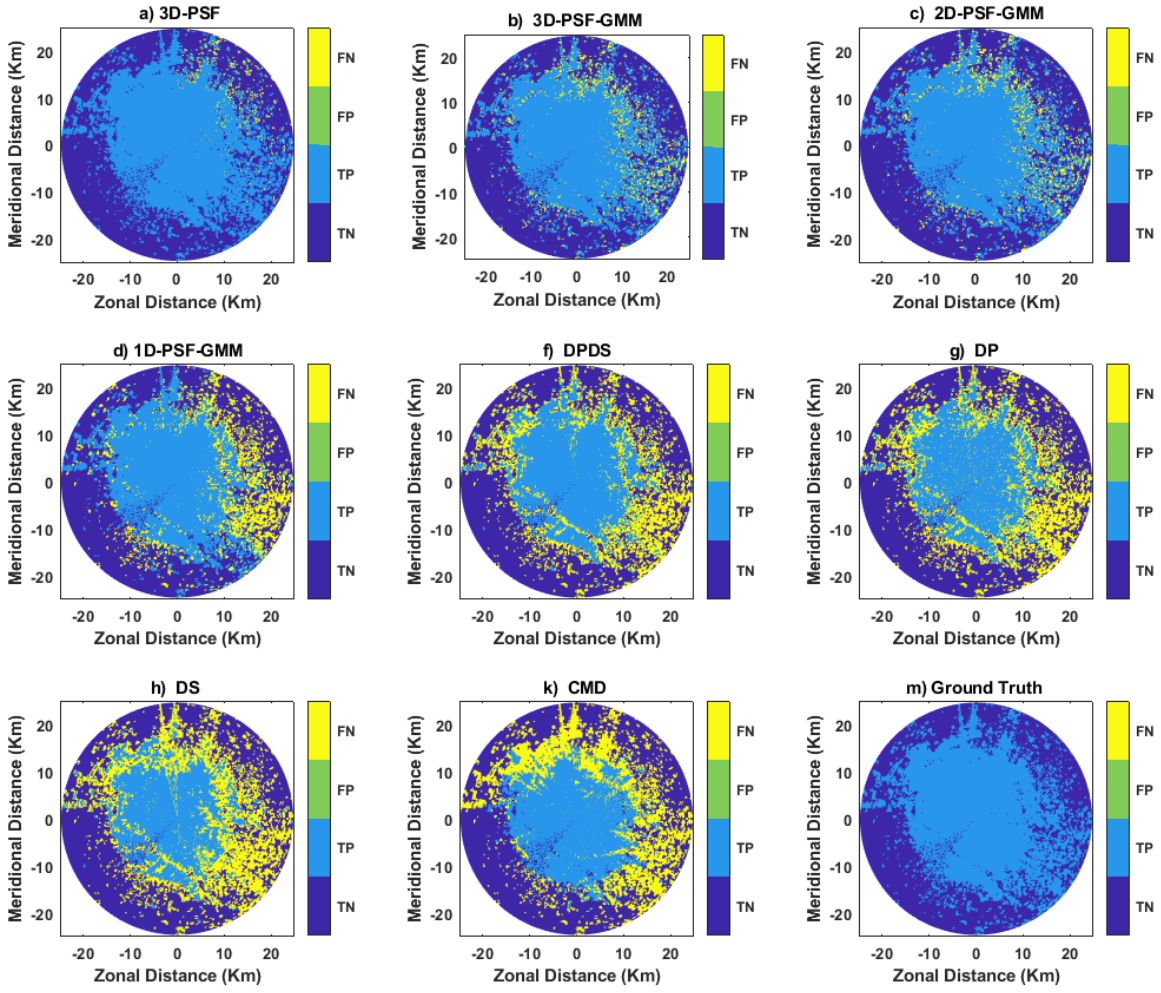

Figure 5-14: Clutter maps using: a) 3D-PSD algorithm, b) 3D-PSF-GMM algorithm, c) 2D-PSF-GMM algorithm, d)1D-PSF algorithm, f) DPDS algorithm, g) DP algorithm, h) DS algorithm, k) CMD algorithm, m) Ground Truth

Chapter 6

Dual Polarization Clutter Filtering

6.1 Introduction

A dual polarization clutter filtering algorithm is presented to mitigate ground clutter effects on weather radar measurements. The statistical properties of the dual polarization radar data are utilized in time and spectral domains to reconstruct the weather signals/data from clutter contaminated resolution volumes. A multivariate Gaussian mixture model is introduced to parametrize clutter and weather power spectrums, and the Maximum A Posterior (MAP) method is used to estimate model parameters. Instead of using the random phase, the phase of the retrieved weather spectrum is estimated based on the weather properties to be more accurate. The performance of the filtering algorithm is examined by applying it to the polarimetric data collected the KOUN radar, and the result is compared with that of several existing filtering algorithms. It is shown that the proposed algorithm can effectively mitigate clutter effects and substantially improve polarimetric weather radar data quality.

Because clutter can bias weather radar data, detecting ground clutter mixed with echoes from precipitation is one of the main challenges in weather radar research. Ground clutter is radar echoes received from objects on the ground when parts of the main lobe or sidelobes of the radar antenna illuminate objects on the ground. Therefore, clutter contamination is more severe for the measurements of near ground precipitation, in which the accurate rainfall rate estimation is required.

Generally, clutter is supposed to be stationary in the time domain and is located around zero Doppler velocity in the spectral domain, because ground targets are stationary or only have slow motions. Therefore, a band-stop filter as a simple traditional method can be applied to the radar data to mitigate the clutter effects on weather signals [1, 2]. Although this filtering method is frequently used to remove clutter from

weather signals, some power components of weather signals may fall into the stop-band of the filter. This can suppress the power components of weather signals and causes bias estimates of spectral moments, especially for narrow-band zero-velocity weather signals [3-6]. Thus, the ground clutter locations need to be accurately identified before applying clutter filters to avoid biases from unnecessarily filtering weather signals.

Over the past few years, researchers in the weather radar community focused on the design of effective clutter detection algorithms to achieve better data quality and reduce error rates [5, 13, 18, 19, 41, 57]. The quality of radar data is important to accurately estimate polarimetric parameters that can provide important information such as rainfall rate, tornado signatures and types of precipitation.

Recently, clutter filtering in the frequency domain has become more popular. The authors in [28] proposed the Gaussian model adaptive processing (GMAP) method. GMAP could recover the weather spectrum after notching the spectrum around zero velocity. However, the filtering still biases the weather signal, and its performance needs to be improved. Hence, after detecting ground clutter, a high-performance clutter filtering system needs to be applied to retrieve weather signals with the least bias effect on weather signals. In [12], the clutter environment analysis using adaptive processing (CLEAN-AP) algorithm is introduced based on the Autocorrelation Spectral Density (ASD) to suppress the effect of ground clutter to achieve better performance. This technique is extended in [13] to apply ASD to the staggered-PRT (pulse repetition time) sequences. The authors in [2] have introduced the Spectrum-Time Estimation and Processing (STEP) algorithm to mitigate the clutter effects on weather

signals. A bi-Gaussian model is considered in this algorithm to estimate the clutter and weather power components in the spectral domain.

The existing clutter filtering algorithms [2, 28, 58-62] are mostly focused on retrieving the spectrum amplitude from the power spectrum. These algorithms are using a random based method to obtain the spectrum phase of weather signals. It is shown in [57] that the wave scattering from the randomly distributed hydrometers yields rapidly fluctuating phase due to turbulence and mean radial velocity. Therefore, the phase of weather signals is typically a rapidly varying function (with a random component due to turbulence), whereas the phase of the ground clutter is a typically slowly varying function. Although using a random phase for the spectrum phase can be acceptable for single polarization weather data, it can bias the estimates of dual polarization weather parameters (such as co-polar cross-correlation coefficient). Therefore, the dual-polarization statistical properties are considered in this chapter to achieve a better performance compared with the existing clutter filtering algorithms.

A dual-polarization ground clutter filtering is introduced in this chapter to suppress the ground clutter effects on dual-polarization weather radar observations. It is generally expected that clutter signals have a Gaussian shape power spectrum and a multivariate Gaussian mixture model distribution is introduced to represent the power spectrum for both clutter and weather components. The model parameters are estimated based on the Maximum-Likelihood, using the Expectation-Maximization (ML-EM) method.

6.2 Ground Clutter Filtering

In this section, a dual-polarization clutter filtering algorithm (DPCF) is introduced to remove ground clutter from weather radar signals. From the previous chapter, if ground clutter is not detected or the SNR value is less than 20dB, the original I/Q data is used to calculate weather moments. However, if weather echoes are contaminated by clutter signals, the DPCF is applied to remove the ground clutter from weather radar signals, in the spectral domain.

It is generally expected that clutter signals have a Gaussian shape power spectrum and generally in clutter filtering algorithms (e.g., Gaussian model adaptive processing (GMAP) [28], and BGMAP [2]), a Gaussian distribution is fitted to estimate the clutter component of the power spectrum. The bi-Gaussian distribution is defined as:

$$\begin{aligned}\widehat{S}_{\mathrm{h}}(v) &= \frac{P_{w1}}{\sqrt{2\pi\sigma_{vw1}^2}}\exp\left[-\frac{(v-v_{rw1})^2}{2\sigma_{vw1}^2}\right]+\frac{P_{c1}}{\sqrt{2\pi\sigma_{vc1}^2}}\exp\left[-\frac{(v-v_{rc1})^2}{2\sigma_{vc1}^2}\right]+\frac{P_{n1}}{2v_{n1}}= \\ &= \underbrace{\widehat{S}_{W_{\mathrm{h}}}(v)}_{Weather}+\underbrace{\widehat{S}_{C_{\mathrm{h}}}(v)}_{Clutter}+\underbrace{\widehat{N}_{\mathrm{h}}(v)}_{Noise} \\ \widehat{S}_{\mathrm{v}}(v) &= \underbrace{\frac{P_{w2}}{\sqrt{2\pi\sigma_{vw2}^2}}\exp\left[-\frac{(v-v_{rw2})^2}{2\sigma_{vw2}^2}\right]}_{Weather}+\underbrace{\frac{P_{c2}}{\sqrt{2\pi\sigma_{vc2}^2}}\exp\left[-\frac{(v-v_{rc2})^2}{2\sigma_{vc2}^2}\right]}_{Clutter}+\underbrace{\frac{P_{n2}}{2v_{n2}}}_{Noise} \\ &= \underbrace{\widehat{S}_{W_{\mathrm{v}}}(v)}_{Weather}+\underbrace{\widehat{S}_{C_{\mathrm{v}}}(v)}_{Clutter}+\underbrace{\widehat{N}_{\mathrm{v}}(v)}_{Noise}\end{aligned} \tag{6.1}$$

where $P_{w1}, P_{w2}, P_{c1}, P_{c2}, P_{n1}$ and P_{n2} are the weather power, clutter power, and noise power for horizontal and vertical polarizations, respectively. v_{rw1}, v_{rw2} and v_{rc1}, v_{rc2} are the mean Doppler velocity of weather and clutter for H and V polarizations, and v_{n1}, v_{n2} are the Nyquist velocities. $\sigma_{vw1}, \sigma_{vw2}$ and $\sigma_{vc1}, \sigma_{vc2}$ are the spectrum

width of weather and clutter, for H and V polarizations. It is typically expected that the spectrum width for weather is larger than that for clutter (i.e., $\sigma_{vc1} < \sigma_{vw1}, \sigma_{vc2} < \sigma_{vw2}$).

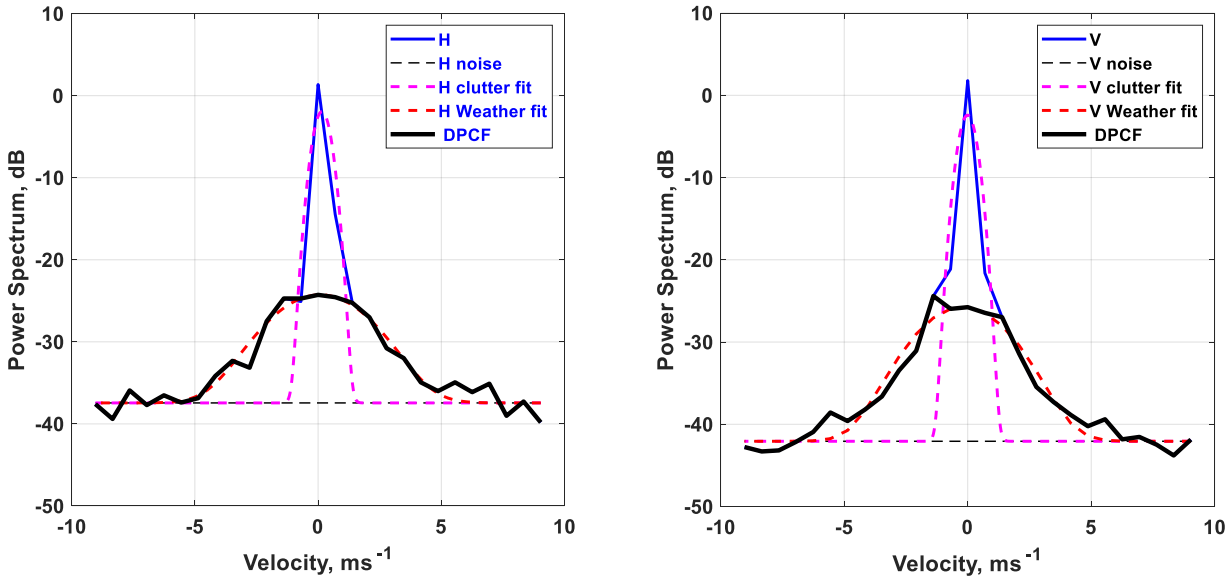

Figure 6-1: Dual-polarization clutter filtering for H-polarization and V-polarization

Weather spectrum and clutter spectrum centered at the mean Doppler velocity of weather signal, and the mean Doppler velocity of ground clutter, respectively. The noise level ($P_{n1} / 2v_{N1}, P_{n2} / 2v_{N2}$) can be predetermined by using the method described in [63]. Thus, the following parameters need to be estimated:

- Powers: P_{w1}, P_{w2}, P_{c1}, P_{c2}
- Mean Doppler Velocities: v_{rw1}, v_{rw2}, v_{rc1}, v_{rc2}
- Spectrum Width $\sigma_{vw1}, \sigma_{vw2}, \sigma_{vc1}, \sigma_{vc2}$.

The mean Doppler velocities of ground clutter (v_{rc1}, v_{rc2}) have near-zero values and can only be within the range of [-Δv, Δv]; where Δv is the spectral line spacing. An example of a dual polarization clutter filtering algorithm is shown in Figure 6-1. A

Maximum Likelihood (ML) method is used to estimate the model parameters. In this figure, the blue lines indicate the power spectrum of horizontal and vertical polarizations, obtained from the I/Q data. Dashed lines denote the fitted power spectrum for clutter and weather components (i.e., $S_{W_H}(v), S_{C_H}(v)$, $S_{W_V}(v), S_{C_V}(v)$), and black dashed lines denote noise components. The solid black lines indicate the power spectrum of clutter filtered data. During the estimation of the power spectrum, the limited number of pulses may cause power leakage from one frequency to other frequencies. The power leakage might overwhelm the weather signal, biasing the estimation of the weather spectrum. Therefore, a window function is used based on the method described in [3], in order to minimize the bias of weather spectra moments. The application of a window function can significantly reduce power leakage when the power spectrum is estimated.

6.3 Window Function

Considering the spectral leakage due to a limited number of samples, the selection of window function is essential for the reconstruction process [64] in order to minimize the bias of weather spectra moments. Generally, a time-domain window is applied to the IQ data prior to performing the FFT. If the clutter is very weak, a rectangular window is used for removing clutter. The more aggressive window such as the Hamming or Blackman, is required when the clutter is strong. In this dissertation, the window is selected based on the CSR values. Window selection methods [64] for the BGMAP algorithm are shown below:

- *First, a Hamming window weighting function is applied to the IQ data, and then the BGMAP algorithm is implemented.*

- *If the estimated CSR > 40 dB, repeat BGMAP using a Blackman-Harris window.*
- *If the estimated CSR > 20 dB, repeat BGMAP using a Blackman window; Then if CSR > 25 dB, Blackman results are used.*
- *If CSR < 2.5 dB, repeat BGMAP using rectangular window; then, if CSR < 1 dB, rectangular results are used.*
- *ELSE, accept the Hamming window results.*

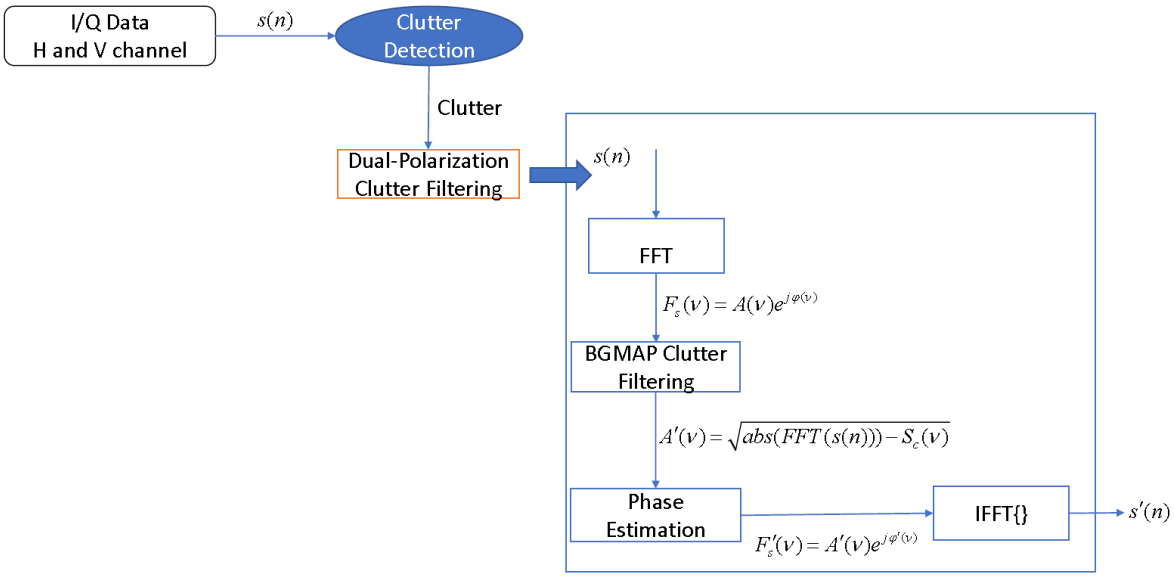

Figure 6-2: Flowchart of Dual-Polarization Clutter Filtering

The amplitude and the phase are considered to be clutter contaminated and have a clutter component. The power spectrum is calculated from the amplitude part:

$$S_{\mathrm{h}}(v) = 20\log_{10}\left|s_{\mathrm{h}}(v)\right| = \underbrace{S_{W_{\mathrm{h}}}(v)}_{Weather} + \underbrace{S_{C_{\mathrm{h}}}(v)}_{Clutter} + \underbrace{N_{\mathrm{h}}(v)}_{Noise}$$
$$S_{\mathrm{v}}(v) = 20\log_{10}\left|s_{\mathrm{v}}(v)\right| = \underbrace{S_{W_{\mathrm{v}}}(v)}_{Weather} + \underbrace{S_{C_{\mathrm{v}}}(v)}_{Clutter} + \underbrace{N_{\mathrm{v}}(v)}_{Noise} \qquad (6.3)$$

It is clear that for the clutter contaminated signals, the total power spectrum consists of three components: ground clutter, weather signal, and noise. The ground clutter is estimated from the bi-Gaussian model, and thus, the weather component can be estimated by removing the estimated clutter component from the total power spectrum.

$$\begin{aligned} \hat{S}_{W_h}(v) &= S_h(v) - \hat{S}_{C_h}(v) - N_h(v) \\ \hat{S}_{W_v}(v) &= S_v(v) - \hat{S}_{C_v}(v) - N_v(v) \end{aligned} \tag{6.4}$$

Therefore, the amplitude part ($\left|\hat{s}_h(v)\right|$) is obtained from the estimated power spectrum ($\hat{S}_h(v)$), and the phase part needs to be estimated. In recent clutter filtering algorithms such as BGMAP and GMAP, the phase of retrieved weather part is considered to be random in the clutter contaminated region. However, a random phase can bias the weather data. The inverse fast Fourier transform (*IFFT*) can be obtained as:

$$\begin{aligned} \hat{s}_{W_h}(v) &= \left|\hat{s}_{W_h}(v)\right| \exp\left(j \measuredangle \hat{s}_{W_h}(v)\right) \quad \Rightarrow \begin{cases} \left|\hat{s}_{W_h}(v)\right| \\ \measuredangle \hat{s}_{W_h}(v) \end{cases} \\ \hat{s}_{W_v}(v) &= \left|\hat{s}_{W_v}(v)\right| \exp\left(j \measuredangle \hat{s}_{W_v}(v)\right) \quad \Rightarrow \begin{cases} \left|\hat{s}_{W_v}(v)\right| \\ \measuredangle \hat{s}_{W_v}(v) \end{cases} \end{aligned} \tag{6.5}$$

$$\begin{aligned} \hat{V}_{W_h}(n) &= IFFT\left\{\hat{s}_{W_h}(v)\right\} \\ \hat{V}_{W_v}(n) &= IFFT\left\{\hat{s}_{W_v}(v)\right\} \end{aligned}$$

The amplitude part of the spectrum is estimated from removing the estimated clutter component of the power spectrum from the total power. However, the phase part ($\measuredangle \hat{s}_h(v), \measuredangle \hat{s}_v(v)$) needs to be retrieved for the weather spectral coefficients, after

removing ground clutter by the filter. For dual-polarization radars, the complex data on the frequency domain is required to estimate dual polarization moments, especially for phase-related radar parameters, such as cross-correlation coefficient (ρ_{hv}) and differential reflectivity (Z_{DR}). Most recent clutter filtering algorithms such as *GMAP* and *BGMAP* are using a random phase for both *h* and *v* polarizations with zero differential phase ($\phi_h - \phi_v$) to retrieve the phase in the clutter range (near zero velocity in the spectral domain $|v| \le |v_c|$), and the same phases are used for other ranges ($|v| > |v_c|$). Here, we discuss the contribution of the phase component on the dual polarization cross-correlation coefficient (ρ_{hv}). From the Parseval's identity, we have:

$$\left\langle V_{\mathrm{h}}(n), V_{\mathrm{v}}^{*}(n) \right\rangle = \frac{1}{M} \left\langle s_{\mathrm{h}}(v), s_{\mathrm{v}}^{*}(v) \right\rangle \tag{6.6}$$

where $s_{\mathrm{h}}(v) = FFT\left[V_{\mathrm{h}}(n)\right]$, $s_{\mathrm{v}}(v) = FFT\left[V_{\mathrm{v}}(n)\right]$. Therefore, the cross-correlation between H-pol and V-pol can be calculated in spectra domain or time domain and can be written as:

$$|\rho_{\mathrm{hv}}| = \frac{\left|\left\langle V_{\mathrm{h}}(n), V_{\mathrm{v}}^{*}(n) \right\rangle\right|}{\sqrt{\left\langle V_{\mathrm{h}}(n), V_{\mathrm{h}}^{*}(n) \right\rangle}\sqrt{\left\langle V_{\mathrm{v}}(n), V_{\mathrm{v}}^{*}(n) \right\rangle}} = \frac{\left|\left\langle s_{\mathrm{h}}(n), s_{\mathrm{v}}^{*}(n) \right\rangle\right|}{\sqrt{\left\langle s_{\mathrm{h}}(n), s_{\mathrm{h}}^{*}(n) \right\rangle}\sqrt{\left\langle s_{\mathrm{v}}(n), s_{\mathrm{v}}^{*}(n) \right\rangle}}$$

As can be seen from Figure 2-4, the PDF of ρ_{hv} for weather signals has a narrow near one value (e.g. $|\rho_{hv}| = 1$), whereas the clutter PDF has a wider range of values. Therefore, it is generally expected that the weather PDF of ρ_{hv} should have larger values compared to clutter, and the peak value for the PDF is near one. Therefore, to have a near one value for the ρ_{hv}, the complex value of horizontal and vertical polarizations should be proportionally related, in both time and spectral domains:

$$|\rho_{hv}| \approx 1$$

$$|\rho_{hv}| = \frac{\left|\left\langle V_{\mathrm{h}}(n), V_{\mathrm{v}}^{*}(n)\right\rangle\right|}{\sqrt{\left\langle V_{\mathrm{h}}(n), V_{\mathrm{h}}^{*}(n)\right\rangle}\sqrt{\left\langle V_{\mathrm{v}}(n), V_{\mathrm{v}}^{*}(n)\right\rangle}} = \frac{\left|\left\langle s_{\mathrm{h}}(v), s_{\mathrm{v}}^{*}(v)\right\rangle\right|}{\sqrt{\left\langle s_{\mathrm{h}}(v), s_{\mathrm{h}}^{*}(v)\right\rangle}\sqrt{\left\langle s_{\mathrm{v}}(v), s_{\mathrm{v}}^{*}(v)\right\rangle}} \approx 1$$

$$\Rightarrow \begin{cases} \left|\left\langle V_{\mathrm{h}}(n), V_{\mathrm{v}}^{*}(n)\right\rangle\right| \approx \sqrt{\left\langle V_{\mathrm{h}}(n), V_{\mathrm{h}}^{*}(n)\right\rangle}\sqrt{\left\langle V_{\mathrm{v}}(n), V_{\mathrm{v}}^{*}(n)\right\rangle} \\ \left|\left\langle s_{\mathrm{h}}(v), s_{\mathrm{v}}^{*}(v)\right\rangle\right| \approx \sqrt{\left\langle s_{\mathrm{h}}(v), s_{\mathrm{h}}^{*}(v)\right\rangle}\sqrt{\left\langle s_{\mathrm{v}}(v), s_{\mathrm{v}}^{*}(v)\right\rangle} \end{cases}$$

$$|\rho_{hv}| = 1 \quad \xrightarrow{\textit{Ideal case}} \quad \begin{cases} V_{\mathrm{h}}(n) = c_1 V_{\mathrm{v}}(n) \\ s_{\mathrm{h}}(v) = c_2 s_{\mathrm{v}}(v) \end{cases} \quad \textit{for } n = [1, \mathrm{M}]$$

$$s_{\mathrm{h}}(v) = c_2 s_{\mathrm{v}}(v) \Rightarrow |s_{\mathrm{h}}(v)| \exp\left(j \measuredangle s_{\mathrm{h}}(v)\right) = c_2 |s_{\mathrm{v}}(v)| \exp\left(j \measuredangle s_{\mathrm{v}}(v)\right)$$

where c_1 and c_2 are constant. It is expected that the power spectrum for H-pol and V-pol should be proportionally related after filtering clutters. Figure 6-1 shows the DPCF filtering algorithm for the H-polarization and V-polarization.

Figure 6-3 shows the cross correlation coeficient of the filtered data using DPCF clutter filtering algorithm compared to BGMAP, and GMAP algorithms for the testing data.

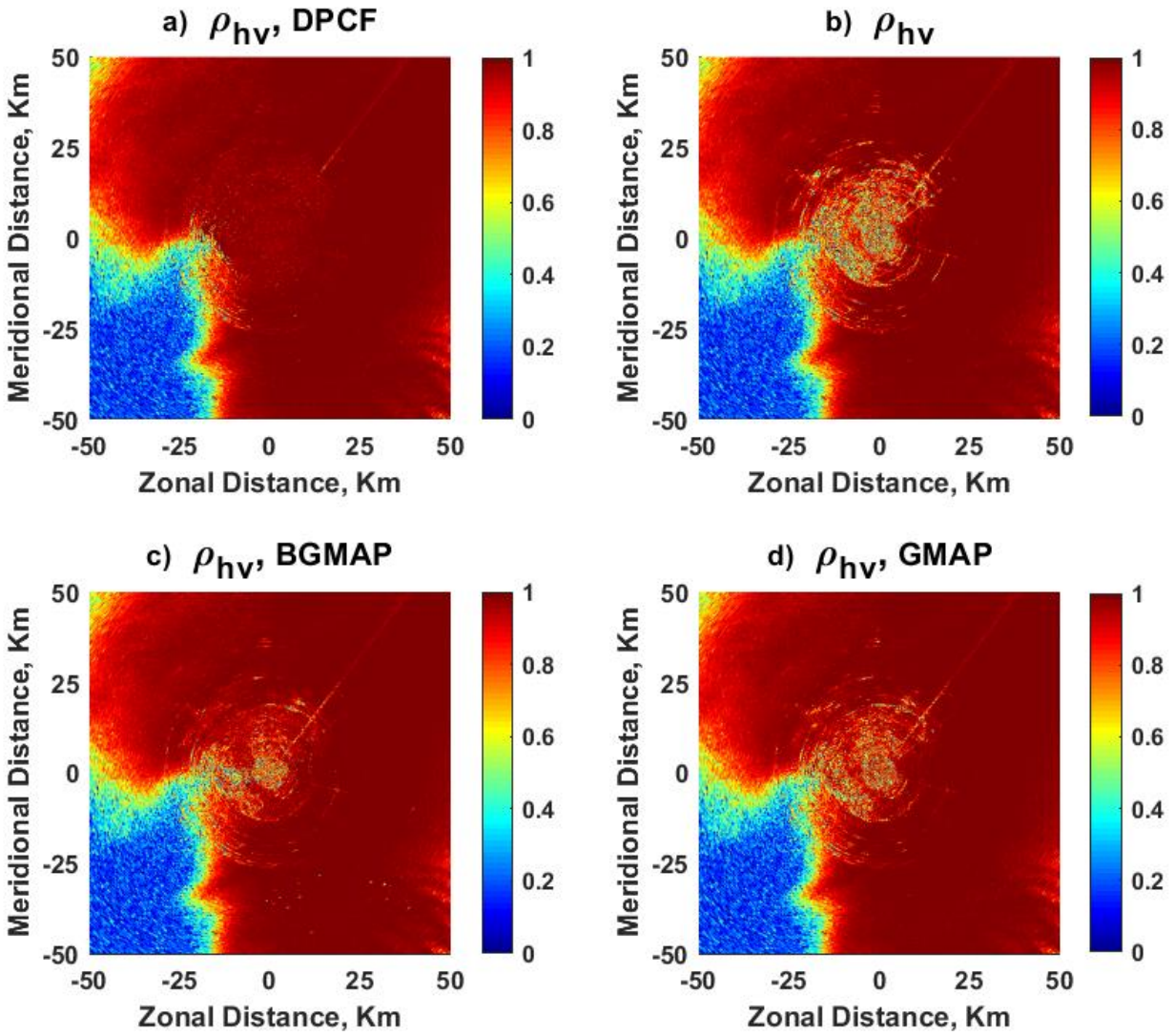

Figure 6-3: Cross-Correlation Coefficient ρ_{hv} for a) DPCF algorithm, b) clutter contaminated data, c) BGMAP algorithm, d) GMAP algorithm

Chapter 7

Conclusions and Future Works

We have introduced PFI as a new discriminant function to improve clutter detection algorithms for weather radars. It is demonstrated that the probability density functions of the PFI for weather and clutter has a very good separation between clutter and weather signals. The PFI property has been analyzed for the proposed detection algorithm, and it is shown that the PFI detects clutter mixed with weather echoes with a P_D better than 90% even for CSR as low as -20 dB. Furthermore, the proposed clutter detection based on PFI can achieve a good performance gain even if dual-polarization data is not available. The PDFs of PFI for H and V polarizations have been jointly combined with the dual scan cross-correlation coefficient to form a unique 3D discriminant function with outstanding performance improvements. The PDFs of discriminant functions need to be parametrized because the class conditional densities for clutter and weather data may change and may need to be updated based on the weather, clutter, radar parameters, and antenna rotation. Additionally, the complete knowledge about the probabilistic structure of the class conditional densities may not be available for real-time implementations. Therefore, a multivariate Gaussian mixture model is introduced to parameterize the PDF of discriminant functions, and the parameters are estimated based on the maximum likelihood method, using the Expectation-Maximization algorithm. A simple Bayesian classifier has been defined to make an optimal decision for the clutter detection. Practical datasets collected and edited by the WSR-88D (KOUN) polarimetric radar have verified the performance of our proposed detection algorithm compared to other existing detection algorithms. The statistical and physical characteristics obtained from PFI have been used to

develop clutter filtering algorithms and also the detection algorithm can be generalized for target detect, for future works.

The preliminary results for clutter detection and filtering algorithms are promising. However, algorithms should be evaluated using other types of weather conditions. Furthermore, the terrain surrounding KOUN represents clutter from urban, wooded, and prairie regions; the performance of detection algorithms to detect clutter from heavily foliage woods under different wind conditions needs to be addressed entirely.

Of great interest for future expansion of advanced radar systems would be multi-band, multi-function, and concurrent transmit-receive systems. However, these systems require reconfigurable hardware for flexible and dynamic operation in a shared spectrum environment. Reconfigurable RF filters are among the most crucial components for such advanced radar systems. [65-69] The works presented in this dissertation can be expanded in the area of the interference cancelation and clutter mitigation based on adaptive null steering techniques. An evolutionary optimization algorithm can be used for the pattern synthesis to mitigate the interference effects on the received signals, by steering nulls on the interference direction. [70-72].

References:

[1] H. L. Groginsky and K. M. Glover, "Weather radar canceller design," presented at the Conference on Radar Meteorology, Miami Beach, FL, 1980.

[2] Q. Cao, G. Zhang, R. D. Palmer, M. Knight, R. May, and R. J. Stafford, "Spectrum-Time Estimation and Processing (STEP) for Improving Weather Radar Data Quality," *IEEE Transactions on Geoscience and Remote Sensing,* vol. 50, Nov. 2012.

[3] A. D. Siggia and R. E. Passarelli, "Gaussian model adaptive processing (GMAP) for improved ground clutter cancellation and moment calculation," in *Third European Conf. on Radar in Meteorology and Hydrology*, Visby, Sweden, 2004, pp. 67-73.

[4] R. J. Doviak and D. S. Zrnic, *Doppler Radar & Weather Observations (2nd Edition)*, New York: Dover, 2006.

[5] G. Zhang, *Weather Radar Polarimetry*: CRC Press, 2016.

[6] L. Lei, G. F. Zhang, R. J. Doviak, R. Palmer, B. L. Cheong, M. Xue*, et al.*, "Multilag Correlation Estimators for Polarimetric Radar Measurements in the Presence of Noise," *Journal of Atmospheric and Oceanic Technology,* vol. 29, pp. 772-795, Jun 2012.

[7] Y. G. Li, G. F. Zhang, R. J. Doviak, L. Lei, and Q. Cao, "A New Approach to Detect Ground Clutter Mixed With Weather Signals," *IEEE Transactions on Geoscience and Remote Sensing,* vol. 51, pp. 2373-2387, Apr 2013.

[8] P. Meischner, *Weather Radar Principles and Advanced Applications*. Berlin, Germany:: Springer-Verlag, 2002.

[9] J. C. Hubbert, M. Dixon, S. M. Ellis, and G. Meymaris, "Weather Radar Ground Clutter. Part I: Identification, Modeling, and Simulation," *Journal of Atmospheric and Oceanic Technology,* vol. 26, pp. 1165-1180, Jul 2009.

[10] J. C. Hubbert, M. Dixon, S. M. Ellis, and G. Meymaris, "Weather Radar Ground Clutter. Part II: Real-Time Identification and Filtering," *Journal of Atmospheric and Oceanic Technology,* vol. 26, pp. 1181-1197, Jul 2009.

[11] L. Yinguang, Z. Guifu, and R. J. Doviak., "A new approach to detect the ground clutter mixed with weather echoes," presented at the IEEE Radar Conference (RADAR), 2011.

[12] D. A. Warde and S. M. Torres, "The Autocorrelation Spectral Density for Doppler-Weather-Radar Signal Analysis," *IEEE Transactions on Geoscience and Remote Sensing,* vol. 52, pp. 508-518, Jan 2014.

[13] S. M. Torres and D. A. Warde, "Ground Clutter Mitigation for Weather Radars Using the Autocorrelation Spectral Density," *Journal of Atmospheric and Oceanic Technology,* vol. 31, pp. 2049-2066, 2014.

[14] S. M. Bachmann, "Phase-based clutter identification in spectra of weather radar signals," *IEEE Geoscience and Remote Sensing Letters,* vol. 5, pp. 487-491, Jul 2008.

[15] J. J. Gourley, P. Tabary, and J. P. D. Chatelet, "A fuzzy logic algorithm for the separation of precipitating from nonprecipitating echoes using polarimetric

radar observations," *Journal of Atmospheric and Oceanic Technology,* vol. 24, pp. 1439-1451, Aug 2007.

[16] H. Park, A. V. Ryzhkov, D. S. Zrnic, and K. E. Kim, "The Hydrometeor Classification Algorithm for the Polarimetric WSR-88D: Description and Application to an MCS," *Weather and Forecasting,* vol. 24, pp. 730-748, Jun 2009.

[17] M. A. Rico-Ramirez and I. D. Cluckie, "Classification of ground clutter and anomalous propagation using dual-polarization weather radar," *IEEE Transactions on Geoscience and Remote Sensing,* vol. 46, pp. 1892-1904, Jul 2008.

[18] M.-H. Golbon-Haghighi, G. Zhang, Y. Li, and R. Doviak, "Detection of Ground Clutter from Weather Radar Using a Dual-Polarization and Dual-Scan Method," *Atmosphere Journal,* vol. 7, 2016.

[19] Y. Li, G. Zhang, and R. J. Doviak, "Ground Clutter Detection Using the Statistical Properties of Signals Received With a Polarimetric Radar," *IEEE Transactions on Signal Processing,* vol. 62, pp. 597-606, 2014.

[20] Y. Li, G. Zhang, R. J. Doviak, and D. S. Saxion, "Scan-to-Scan Correlation of Weather Radar Signals to Identify Ground Clutter," *IEEE Transactions on Geoscience and Remote Sensing,* vol. 10, JULY 2013.

[21] G. Wen, A. Protat, and H. Xiao, "An Objective Prototype-Based Method for Dual-Polarization Radar Clutter Identification," *Atmosphere,* vol. 8, p. 72, 2017.

[22] D. N. Moisseev and V. Chandrasekar, "Polarimetric spectral filter for adaptive clutter and noise suppression," *Journal of Atmospheric and Oceanic Technology,* vol. 26, pp. 215-228, Feb. 2009.

[23] M. T. Falconi, M. Montopoli, and F. S. Marzano, "Bayesian statistical analysis of ground-clutter for the relative calibration of dual polarization weather radars," *European Journal of Remote Sensing,* vol. 49, pp. 933-953, 2016.

[24] M. T. Falconi, "Remote Sensing and Electromagnetic Modeling Applied to Weather and Forward Scatter Radar," Doctoral Sapienza University of Rome). 2018.

[25] P. Bukovcic, A. Ryzhkov, D. Zrnic, and G. F. Zhang, "Polarimetric Radar Relations for Quantification of Snow Based on Disdrometer Data," *Journal of Applied Meteorology and Climatology,* vol. 57, pp. 103-120, Jan 2018.

[26] P. Bukovcic, D. Zrnic, and G. F. Zhang, "Convective-stratiform separation using video disdrometer observations in central Oklahoma - the Bayesian approach," *Atmospheric Research,* vol. 155, pp. 176-191, Mar 15 2015.

[27] P. Bukovcic, D. Zrnic, and G. F. Zhang, "Winter Precipitation Liquid-Ice Phase Transitions Revealed with Polarimetric Radar and 2DVD Observations in Central Oklahoma," *Journal of Applied Meteorology and Climatology,* vol. 56, pp. 1345-1363, May 2017.

[28] A. D. Siggia and R. E. Passarelli, "Gaussian model adaptive processing (GMAP) for improved ground clutter cancellation and moment calculation," *Proc.*

Third European Conf. on Radar in Meteorology and Hydrology, Visby, Sweden, ERAD, 67-73, 2004.

[29] M. H. Golbon-Haghighi, G. F. Zhang, and R. J. Doviak, "Ground Clutter Detection for Weather Radar Using Phase Fluctuation Index," *IEEE Transactions on Geoscience and Remote Sensing,* vol. 57, pp. 2889-2895, May 2019.

[30] L. Yinguang, Z. Guifu, and R. J. Doviak, "Ground Clutter Detection Using the Statistical Properties of Signals Received With a Polarimetric Radar," *IEEE Transactions on Signal Processing,* vol. 62, pp. 597-606, Feb. 2014.

[31] M. H. Golbon-Haghighi, H. Saeidi-Manesh, G. F. Zhang, and Y. Zhang, "Pattern Synthesis for the Cylindrical Polarimetric Phased Array Radar (CPPAR)," *Progress in Electromagnetics Research M,* vol. 66, pp. 87-98, 2018.

[32] H. Saeidi-Manesh, S. Karimkashi, G. F. Zhang, and R. J. Doviak, "High-Isolation Low Cross-Polarization Phased-Array Antenna for MPAR Application," *Radio Science,* vol. 52, pp. 1544-1557, Dec 2017.

[33] H. Saeidi-Manesh, M. Mirmozafari, and G. Zhang, "Low cross-polarisation high-isolation frequency scanning aperture coupled microstrip patch antenna array with matched dual-polarisation radiation patterns," *Electronics Letters,* vol. 53, pp. 901-902, Jul 6 2017.

[34] H. Saeidi-Manesh and G. Zhang, "Cross-polarisation suppression in cylindrical array antenna," *Electronics Letters,* vol. 53, pp. 577-578, Apr 27 2017.

[35] H. Saeidi-Manesh and G. Zhang, "Dual-polarised hybrid feed microstrip patch antenna for multifunction application (vol 55, 2018)," *Electronics Letters,* vol. 55, pp. 358-358, Mar 21 2019.

[36] H. Saeidi-Manesh and G. Zhang, "Dual-polarised hybrid feed microstrip patch antenna for multifunction application," *Electronics Letters,* vol. 55, pp. 679-680, Jun 13 2019.

[37] H. Saeidi-Manesh and G. F. Zhang, "Characterization and Optimization of Cylindrical Polarimetric Array Antenna Patterns for Multi-Mission Applications," *Progress in Electromagnetics Research-Pier,* vol. 158, pp. 49-61, 2017.

[38] H. Saeidi-Manesh and G. F. Zhang, "High-Isolation, Low Cross-Polarization, Dual-Polarization, Hybrid Feed Microstrip Patch Array Antenna for MPAR Application," *Ieee Transactions on Antennas and Propagation,* vol. 66, pp. 2326-2332, May 2018.

[39] H. Saeidi-Manesh and G. F. Zhang, "Low Cross-Polarization, High-Isolation Microstrip Patch Antenna Array for Multi-Mission Applications," *Ieee Access,* vol. 7, pp. 5026-5033, 2019.

[40] M.-H. Golbon-Haghighi and G. Zhang, "Detection of Ground Clutter for Dual-Polarization Weather Radar Using a Novel 3D Discriminant Function," *Journal of Atmospheric and Oceanic Technology,* vol. 36, pp. 1285-1296, 2019.

[41] M.-H. Golbon-Haghighi, G. Zhang, R. J. Doviak, and R. L. Ice, "GROUND CLUTTER DETECTION USING A GAUSSIAN MIXTURE MODEL," in *AMS, 35th*

Conference on Environmental Information Processing Technologies, Phoenix, AZ, 2019.

[42] L. Lei, G. Zhang, R. J. Doviak, R. Palmer, B. L. Cheong, and e. a. M. Xue, "Multilag Correlation Estimators for Polarimetric Radar Measurements in the Presence of Noise," *Journal of Atmospheric and Oceanic Technology,* vol. 29, pp. 772-795, 2012.

[43] V. M. Melnikov and D. S. Zrnic, "Autocorrelation and cross-correlation estimators of polarimetric variables," *Journal of Atmospheric and Oceanic Technology,* vol. 24, pp. 1337-1350, Aug 2007.

[44] M.-H. Golbon-Haghighi, B. Mahboobi, and M. Ardebilipour, "Linear Pre-coding in MIMO–CDMA Relay Networks," *Wireless Personal Communications,* vol. 79, pp. 1321-1341, 2014.

[45] M.-H. Golbon-Haghighi, B. Mahboobi, and M. Ardebilipour, "Multiple Antenna Relay Beamforming for Wireless Peer to Peer Communications," *Journal of Information Systems and Telecommunication (JIST),* vol. 1, pp. 209-215, 2013.

[46] M.-H. Golbon-Haghighi, M. Shirazi, B. Mahboobi, and M. Ardebilipour, "Optimal Beamforming in Wireless Multiuser MIMO-relay Networks," presented at the 21st Iranian Conference on Electrical Engineering (ICEE), 2013.

[47] C. Qing, M. B. Yeary, and Z. Guifu, "Efficient Ways to Learn Weather Radar Polarimetry," *IEEE Transactions on Education,* vol. 55, pp. 58-68, 2012.

[48] Federal Coordinator for Meteorological Services and Supporting Research. [Online].

[49] W. I. S. Richard L. Ice, Norman, OK; and R. D. Rhoton, J. C. Krause, D. S. Saxion, O. E. Boydstun, A. K. Heck, J. N. Chrisman, D. S. Berkowitz, W. D. Zittel, and D. A. Warde, "Automatic clutter mitigation in the WSR-88D, design, evaluation, and implementation," presented at the 34th Conference on Radar Meteorology, Williamsburg, Va, USA, 2009, Paper 5.3.

[50] J. Han, M. Kamber, and J. Pei, *Data Mining: Concepts and Techniques: Concepts and Techniques*: Elsevier Science, 2011.

[51] A. Papoulis, *Probability, Random Variables, and Stochastic Processes*: Mcgraw-Hill, Incorporated, 1991.

[52] L. Yinguang, Z. Guifu, R. J. Doviak, and D. S. Saxion, "Scan-to-Scan Correlation of Weather Radar Signals to Identify Ground Clutter," *IEEE Geoscience and Remote Sensing Letters,* vol. 10, pp. 855-859, 2013.

[53] R. O. Duda, P. E. Hart, and D. G. Stork, *Pattern Classification (2nd Edition)*: Wiley-Interscience, 2000.

[54] S. Theodoridis and K. Koutroumbas, *Pattern Recognition, Fourth Edition*: Academic Press, Inc., 2008.

[55] G. McLachlan and D. Peel, "Finite Mixture Models," I. John Wiley & Sons, Ed., ed, 2000.

[56] M.-H. Golbon-Haghighi and G. Zhang, "Dual Polarization Ground Clutter Filtering," in *AMS 35th Conference on Environmental Information Processing Technologies*, Phoenix, AZ, 2019.

[57] M.-H. Golbon-Haghighi, G. Zhang, and R. J. Doviak, "Ground Clutter Detection for Weather Radar Using Phase Fluctuation Index," *IEEE Transactions on Geoscience and Remote Sensing,* 2018.

[58] M. Sachidananda and D. S. Zrnic, "An improved clutter filtering and spectral moment estimation algorithm for staggered PRT sequences," *Journal of Atmospheric and Oceanic Technology,* vol. 19, pp. 2009-2019, Dec 2002.

[59] M. Sachidananda and D. S. Zrnic, "Ground clutter filtering dual-polarized, staggered PRT sequences," *Journal of Atmospheric and Oceanic Technology,* vol. 23, pp. 1114-1130, Aug 2006.

[60] C. M. Nguyen and V. Chandrasekar, "Polarimetric Variables Retrieval with Clutter Suppression for Staggered PRT Sequences," *Journal of Atmospheric and Oceanic Technology,* vol. 32, pp. 767-782, Apr 2015.

[61] S. M. Torres and D. A. Warde, "Staggered-PRT Sequences for Doppler Weather Radars. Part I: Spectral Analysis Using the Autocorrelation Spectral Density," *Journal of Atmospheric and Oceanic Technology,* vol. 34, pp. 51-63, Jan 2017.

[62] D. A. Warde and S. M. Torres, "Staggered-PRT Sequences for Doppler Weather Radars. Part II: Ground Clutter Mitigation on the NEXRAD Network

Using the CLEAN-AP Filter," *Journal of Atmospheric and Oceanic Technology,* vol. 34, pp. 703-716, Mar 2017.

[63] Hildebra.Ph and R. S. Sekhon, "OBJECTIVE DETERMINATION OF NOISE-LEVEL IN DOPPLER SPECTRA," *Journal of Applied Meteorology,* vol. 13, pp. 808-811, 1974.

[64] A. D. Siggia and R. E. Passarelli, "Gaussian model adaptive processing (GMAP) for improved ground clutter cancellation and moment calculation," in *Proc. Third European Conf. on Radar in Meteorology and Hydrology*, Visby, Sweden, 2004, pp. 67-73.

[65] S. Saeedi, "Frequency-Agile Microwave Filters For Radars With Simultaneous Transmission and Reception," 2015.

[66] S. Saeedi, S. Atash-Bahar, J. Lee, and H. Sigmarsson, "Control System for Piezoelectric-Actuator-Based Tunable Evanescent-Mode Cavity Microwave Filters," *Ieee Transactions on Components Packaging and Manufacturing Technology,* vol. 8, pp. 1979-1989, Nov 2018.

[67] S. Saeedi, J. Lee, and H. Sigmarsson, "Prediction of power handling in tunable, high-Q, substrate-integrated, evanescent-mode cavity bandpass filters," *Electronics Letters,* vol. 52, May 12 2016.

[68] S. Saeedi, J. Lee, and H. H. Sigmarsson, "Novel Coupling Matrix Synthesis for Single-Layer Substrate-Integrated Evanescent-Mode Cavity Tunable Bandstop Filter Design," *Ieee Transactions on Microwave Theory and Techniques,* vol. 63, pp. 3929-3938, Dec 2015.

[69] S. Saeedi, J. Lee, and H. H. Sigmarsson, "Tunable, High-Q, Substrate-Integrated, Evanescent-Mode Cavity Bandpass-Bandstop Filter Cascade," *Ieee Microwave and Wireless Components Letters,* vol. 26, pp. 240-242, Apr 2016.

[70] M.-H. Golbon-Haghighi and G. Zhang, "Pattern Synthesis for Conformal Phased Array Antenna using A Multi-Objective Optimization," presented at the 39th AMS International Conference on Radar Meteorology, Nara, Japan, 2019.

[71] M.-H. Golbon-Haghighi and G. Zhang, "Interference mitigation for the phased array radars using a novel null steering technique," presented at the 39th AMS International Conference on Radar Meteorology, Nara, Japan, 2019.

[72] M.-H. Golbon-Haghighi and G. Zhang, "Pattern Synthesis for Conformal Phased Array Antenna using A Multi-Objective Optimization," presented at the 100th American Meteorological Society Annual Meeting, Boston, MA, 2020.